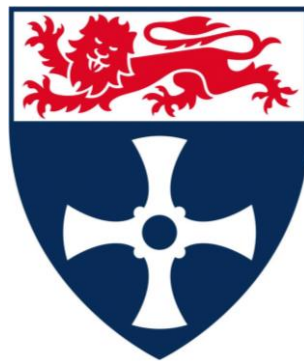


Numerical Modelling of Fluid Flow through a Powered Air-Purifying Respirator Filter



Samuel G. A. Wood

School of Engineering
Newcastle University

This dissertation is submitted for the degree of

Doctor of Philosophy

April, 2020

Declaration

I hereby declare that this thesis is my own original work, except where I have explicitly acknowledged the work of others. No part of this work has been submitted for consideration for any other degree or qualification at this or any other institution. This dissertation contains approximately 40,000 words, 59 figures and 23 tables.

Samuel Wood

April, 2020

Acknowledgements

I would first and foremost like to thank my supervisor, Professor Nilanjan Chakraborty, who has been nothing short of brilliant every step along the way. I'd also like to express my appreciation for all of the wonderful, hyper-caffeinated people I've worked with in the "lab" over the last four years. Non-exhaustively: Bruno Machado, Sahin Yigit, Jiawei Lei, Gulcan Ozel-Erol, Bill Papapostolou, Ilias Konstantinou, Chris Stafford and the many others who have come and gone.

I'm also very grateful to the many people I've collaborated with throughout this project; Jon Thompson, Martin Smith, Mark Summers, Steve McDonald and more. The financial support of DSTL and EPSRC is also greatly appreciated.

I am of course grateful to my family for their support, particularly my brother Joe who has bravely committed to reading this.

Finally, I'd like to thank Alice-Catherine Collins, who I will always owe an enormous debt for the many ways in which she has enabled me.

Abstract

Powered Air-Purifying Respirators (PAPRs), in which air is forced through a filter by means of an integrated motor and blower can provide a significantly higher level of protection than other types of respirator. There is considerable scope for improvement over existing designs, particularly with regards to breath-responsive PAPRs, which provide air only in response to the wearer's inhalation. Understanding the flow of air through such respirators presents a challenging fluid dynamics problem.

In this thesis, the state-of-the-art of respiratory protection is reviewed in order to identify shortcomings and potential areas of improvement. A system-level model has also been developed, which considers each of the key components of a PAPR and presents a simplified depiction of various PAPR parameters under a range of operating conditions. This tool has been designed to integrate more in-depth models of the various PAPR components as they are developed.

The area with the greatest scope for development was found to be the filter. A series of computational fluid dynamics (CFD) simulations using the finite volume method to solve the discretised Reynolds-averaged Navier-Stokes (RANS) equations were conducted based on a typical Chemical Biological Radiological and Nuclear (CBRN) filter canister.

An initial analysis has been conducted to measure the impact of canister geometry on performance metrics such as the pressure drop and the residence time distribution throughout the adsorbent bed by performing a parametric analysis of steady-state axisymmetric simulations. A selection of these geometries were then investigated under transient flow conditions.

A full 3D model of an existing canister geometry has then been developed and simulations are conducted to investigate the extent to which canister performance under steady flow conditions can be used to predict flow behaviour when under a range of real human breathing patterns.

A model to predict adsorption performance of volatile organic compounds on activated carbon has been developed in conjunction with experimental adsorption data, with the intention of relating adsorption behaviour to flow.

The distribution of porosity throughout the adsorbent bed has been shown to have a considerable impact on the distribution of flow. A new method has been developed to better represent the porosity profile by subdividing the bed into discrete sections and assigning a local porosity based on a longitudinally-averaged porosity profile which has been pseudo-randomly perturbed. This porosity model has then been implemented within a 3D CBRN canister model to investigate how different parameters of the porosity model will affect flow.

Axisymmetric simulations have been carried out on a simplified carbon bed geometry using both of these novel adsorption and porosity models in order to gain a better understanding of how the residence time distribution can be related to adsorption.

List of Publications

The following publications have originated from the work presented in this thesis.

Journal articles

Wood, S. G., Chakraborty, N., Smith, M. W., & Summers, M. J. (2019). A computational fluid dynamics analysis of transient flow through a generic Chemical Biological Radiological and Nuclear respirator canister. *Chemical Engineering Research and Design*, 142, 13-24.

Wood, S. G. A., Chakraborty, N., Smith, M. W., & Summers, M. J. (2019). Combined Experimental and Numerical Investigation of Linear Driving Force Kinetics in Small Activated Carbon Beds. *Industrial & Engineering Chemistry Research*, 58(36), 16978-16988.

Wood, S. G. A., Chakraborty, N., Smith, M. W., Summers, M. J., & Brewer, S. A. (2018). The impact of canister geometry on chemical biological radiological and nuclear filter performance: A computational fluid dynamics analysis. *Journal of Occupational and Environmental Hygiene*, 16(1), 41-53.

Conference Proceedings

Wood, S. G. A., & Chakraborty, N. (2018). Transient performance of chemical, biological, radiological and nuclear filter canisters. *ASTFE Digital Library*. Begel House Inc..

Wood, S. G. A., Chakraborty, N., Smith, M. W., & Summers, M. J. (2019) A numerical model for predicting adsorption behaviour in small activated carbon beds. *Proceedings of the 6th International Conference of Fluid Flow, Heat and Mass Transfer (FFHMT'19)*

Wood, S. G. A., & Chakraborty, N. (2019). A numerical model for predicting the impact of porosity distribution within a Chemical Biological Radiological and Nuclear respirator canister. *International Conference on Computational Heat, Mass and Momentum Transfer*

Contents

List of Figures	xi
List of Tables	xv
Nomenclature	xvii
Chapter 1 - Introduction	1
1.1 Background	1
1.2 PAPR Design	2
1.3 Filters	3
1.4 Packed Beds	6
1.5 Mean Air age	7
1.6 Adsorption	8
1.7 Motivations	9
1.8 Scope and Objectives	10
1.9 Thesis Outline	11
Chapter 2 - Numerical Background and Modelling	12
2.1 Governing equations	12
2.2 Turbulence modelling	13
2.3 Near-Wall Treatment	16
2.4 Numerical Method	19
Chapter 3 - Literature Review	24
3.1 Introduction	24
3.2 Respiratory protection devices and their use	24
3.3 Filter types and selection	26
3.4 CFD for CBRN canisters	28
3.5 Adsorption in activated carbon beds	30
3.6 Porosity in packed beds	35
3.7 Conclusions	37
Chapter 4 - System-Level Modelling	39
4.1 System Model Components	39

4.2 Uses and limitations of the existing physical model	46
4.3 Summary of the System-level model	48
Chapter 5 - Effects of Geometry on Performance of a CBRN Canister	50
5.1 Background	50
5.2 Mathematical Background	52
5.3 Configurations	52
5.4 Mesh Independence	54
5.5 Filter Modelling	55
5.6 Numerical Implementation and Boundary Conditions	57
5.7 Data Analysis	58
5.8 Validation	59
5.9 Results of the Steady State Analysis	61
5.10 Key Findings of the Steady State Analysis	72
5.11 Geometries for Transient Analysis	73
5.12 Transient Boundary Conditions	74
5.13 Time-step Selection	74
5.14 Transient Results	74
5.15 Key Findings of the Transient Analysis	77
Chapter 6 - Transient Flow through a Generic CBRN Canister	79
6.1 Background	79
6.2 Mathematical background and Numerical implementation	80
6.3 Turbulence Modelling	81
6.4 Geometry and Boundary Conditions	81
6.5 Grid independence	83
6.6 Turbulence model and Porosity Sensitivity	83
6.7 Model Validation	85
6.8 Transient Breathing Profiles	86
6.9 Results & Discussion	87
6.10 Key Findings	98

Chapter 7 - Experimental and Numerical Investigation of Linear Driving Force Kinetics in Adsorbent Beds	101
7.1 Background	101
7.2 Experimental Method and Results	102
7.3 Numerical Implementation	104
7.4 Mesh independence	106
7.5 Operating and Boundary Conditions	106
7.6 Validation	107
7.7 CFD Results	108
7.8 Key Findings	116
Chapter 8 - Modelling the Stochastic Nature of Porosity in a Respirator Canister	119
8.1 Background	119
8.2 Numerical Modelling	120
8.3 Geometry and Boundary Conditions	121
8.4 Porosity model	121
8.5 Grid independence	123
8.6 Validation	123
8.7 Results and Discussion	124
Chapter 9 - Modelling Adsorption and Residence Time in Porous Beds	138
9.1 Background	138
9.2 Domain and Boundary Conditions	140
9.3 Validation	142
9.4 Results	142
9.5 Key Findings	149
Chapter 10 - Conclusions and Future Work	151
10.1 Impact of Canister Geometry on Filter Performance	151
10.2 The Relationship between Steady-State and Transient Canister Performance	152
10.3 Adsorption Kinetics within an Activated Carbon Bed	153
10.4 Developing a Stochastic Model of Porosity within the Carbon Bed	154

Contents

10.5 Relating Mean Air Age to Adsorption Performance	154
10.6 Future Work	155
References	156

List of Figures

1.1	A representative continuous-flow PAPR (a Scott C420) [5] and a breath-responsive PAPR (a STS Shigematsu Sync01VP3) [6]	2
1.2	Layout of a typical PAPR. The dashed line indicates the feedback loop which is only present in breath-responsive PAPRs.	6
1.3	An example packing of spheres for a bed-to-particle diameter of 7.99, and the location of sphere centres [10].	7
2.1	The solution scheme used for the numerical method.	22
4.1	The individual modules of the system-level model and simplified indications of the flow of data between them.	40
4.2	Example pressure response seen from the system-level model to a single changing parameter (the reference pressure drop across the filter).	47
5.1	Cross section of a typical CBRN filter design.	52
5.2	Schematic diagram of the computational domain for the baseline geometry.	53
5.3	Summary of the variations of the canister geometry considered here: the base case (5.3a), two sizes of bracketing before the carbon filter (5.3b and 5.3c), spacing between the carbon filter and the canister wall (5.3d), curvature of the canister outer wall (5.3e and 5.3f) and two different sizes of bracketing after the carbon filter (5.3g and 5.3h).	54
5.4	Geometric configuration of canister modelled for 3D simulation.	60
5.5	Distribution of pressure difference from the outlet in the case with curvature towards the outlet and extended spacing between the carbon bed and the canister rear wall (the case with the lowest pressure drop).	62
5.6	Distribution of pressure difference from the outlet in the case with the bracketing between the carbon and particulate filters and curvature of the outer wall (the case with the greatest pressure drop)	63
5.7	Alternating regions of high and low velocity close to the canister wall in the base geometry.	63
5.8	Mean age distribution throughout the canister in the case with a curved outer canister wall and bracketing between the carbon and particulate filter and bracketing between the carbon and the rear wall (the case with the smallest mean air age at the carbon outlet).	64

5.9	Mean air age distribution throughout the canister in the case with bracketing between the particulate filter and carbon bed (the case with the greatest mean air age at the carbon outlet).	64
5.10	Pressure drop throughout the canister for all canister geometries.	66
5.11	Mean residence time at the rear of the carbon bed for all canister geometries.	67
5.12	Minimum mean residence at the rear of the carbon bed for all canister geometries.	68
5.13	Distribution of mean air age throughout the canister in the case with the largest minimum residence time at the rear of the carbon bed.	71
5.14	Distribution of mean air age throughout the canister in the case with the smallest minimum residence time at the rear of the carbon bed.	71
5.15	Canister geometries chosen for the transient simulations.	74
5.16	Normalised mean air age at the rear of the carbon bed with respect to distance from the canister outer wall for case I	75
5.17	Normalised mean air age at the rear of the carbon bed with respect to distance from the canister outer wall for case II.	75
5.18	Normalised mean air age at the rear of the carbon bed with respect to distance from the canister outer wall for case III.	75
6.1	Geometry of the configuration considered for all simulations.	82
6.2	Mean air age distributions under steady flow at a cross-section 1mm from the outlet of the carbon bed for the two different turbulence models and descriptions of carbon porosity	85
6.3	Pressure drop across the canister from CFD simulation for steady-state flow using both a constant porosity profile and the Mueller porosity profile compared with the predictions of viscous and inertial losses fit to experimental data	86
6.4	Representative breathing profiles used for each of the cases (showing 2 breaths).	87
6.5	Pressure drop across the canister from CFD simulations at a range of flow rates covering all three complete breathing cycles.	88
6.6	The residence time distribution at the carbon outlet at the same flow rate for each case and the equivalent steady-state flow at two different flow rates.	90
6.7	Distribution of average residence time with canister radius for (a) light breathing, (b) moderate breathing and (c) heavy breathing in the (i) first half of the inhalation (i.e while flow rate is increasing) and (ii) the second half of the inhalation (i.e. while flow rate is decreasing).	92

6.8	The advancing front of a mean air age of 0.15 s throughout the moderate workload breathing cycle and for the equivalent continuous steady flow.	94
6.9	a) Distributions of mean air ages of 0.15 s and 0.3 s for each transient breathing cycle at the moment of first breakthrough and b) Profile for the steady-state equivalent of light breathing for a mean air age of 0.434 s, the lowest residence time at which breakthrough will occur.	95
6.10	The volume fraction of the carbon bed below (a) 0.15 s residence time and (b) 0.3 s residence time throughout each of the breathing profiles	97
7.1	The adsorption isotherm for cyclohexane on activated carbon at 295 K and the mass uptake predicted using the Dubinin-Radushkevich equation fitted to this experimental data.	103
7.2	Outlet stream concentration of cyclohexane for a 15 mm activated carbon bed exposed to three different inlet flow rates with a concentration of 2000 ppm.	104
7.3	The distance into the bed a threshold vapor concentration of $Y_{C_6H_{12}6} = 0.0001$ can be seen for (a) $K_M = 0.004 \text{ s}^{-1}$, (b) $K_M = 0.01 \text{ s}^{-1}$.	109
7.4	Distance contaminant penetrates into the bed in the initial rapid stage, seen against V_I/K_M .	110
7.5	Ratio of front speed to front speed predicted from the Wheeler-Jonas equation for different inlet velocities and values of K_M .	111
7.6	Distribution of uptake of contaminant throughout the bed after 60 s exposure at (a) 200 L/min (inlet velocity 0.567 m/s) and (b) 500 L/min (inlet velocity 1.418 m/s).	112
7.7	Axial velocity distribution close to the inlet of the bed for an inlet flowrate of 200 l min^{-1} (corresponding to an inlet velocity of 0.567 m/s) seen 60 s after first exposure.	113
7.8	The distribution of contaminant in the inlet stream at 200 L/min (inlet velocity 0.567 m/s) immediately before it first contacts the carbon bed.	114
7.9	Distribution of contaminant in the carbon bed 0.1 s after initial exposure at (a) 200 L/min (inlet velocity 0.567 m/s) and (b) 500 L/min (inlet velocity 1.418 m/s) for $K_M = 0.004 \text{ s}^{-1}$ and $K_M = 0.01 \text{ s}^{-1}$	115
7.10	Distribution of contaminant close to the center line 60 s after initial exposure at (a) 200 L/min (0.567 m/s inlet velocity) and (b) 500 L/min (1.418 m/s inlet velocity) for $K_M = 0.004 \text{ s}^{-1}$ and $K_M = 0.01 \text{ s}^{-1}$	116
8.1	Geometry of the CBRN canister simulated in the current study.	122

8.2	Voidage distribution of a cross section taken halfway through the length of the canister for two separate section sizes and b) the radial voidage profiles of these sections.	125
8.3	Profiles of pressure drop across the canister, average mean air age at a cross section at the carbon bed outlet, and the minimum value of the mean air age seen there.	129
8.4	Velocity magnitude distribution 10 mm from the outlet of the carbon bed for $\sigma_E = 2\%$ and $\sigma_E = 25\%$ for a range of section sizes	130
8.5	Representative velocity magnitude distributions of a vertical bed cross section.	131
8.6	Iso-surfaces of a mean air age of 0.7 s coloured by the local turbulent kinetic energy.	132
8.7	Profiles of pressure drop across the canister, average mean air age at a cross section at the carbon bed outlet, and the minimum value of the mean air age seen there, against ratio of section size to standard deviation.	134
8.8	Profiles of pressure drop across the canister, average mean air age at a cross section at the carbon bed outlet, and the minimum value of the mean air age seen there, against ratio of section size to standard deviation for select cases at high flow rates	135
9.1	Configuration of the geometry studied for this investigation.	140
9.2	The axial distance penetrated into the bed over time for each case investigated here.	143
9.3	Axial velocity profiles for each of the cases considered here.	144
9.4	Contours of mean air age for each case investigated here.	145
9.5	The distribution of contaminant close to the inlet after 30 s, overlaid with contours of mean air age for the two different porosity models and two different inlet flow rates investigated here.	145
9.6	the distribution of contaminant close to the inlet after 200 s, overlaid with contours of mean air age, for the two different porosity models and two different inlet flow rates investigated here.	146
9.7	Time at which each area within the bed is first contaminated seen against local mean air age for each case.	148

List of Tables

1.1	Summary of major threats protected against by a CBRN filter.	5
5.1	Key characteristics for each of the meshes used to establish grid independence.	55
5.2	Geometric parameters varied and their respective levels used in the analysis of variance study.	58
5.3	Permeabilities of the materials used for the 3D simulations	59
5.4	Experimental and computational pressure drops across the 3D simulation for a flow rate of 50 L/min.	60
5.5	Hardware used for CFD simulations.	61
5.6	Results of the ANOVA analysis with respect to pressure drop.	69
5.7	Results of the ANOVA analysis with respect to the mean residence time in the carbon at the rear of the carbon bed.	70
5.8	Results of the ANOVA analysis with respect to the minimum residence time in the carbon at the rear of the carbon bed.	72
6.1	Information related to the meshes used for grid independence study.	84
6.2	Mean pressure drops across the canister for the different porosity treatments and turbulence models.	84
6.3	The pressure drops seen across the canister under equivalent steady-state flows and the peak pressure drop for each transient case.	88
6.4	A comparison of the lowest residence time seen at the carbon filter outlet for all three breathing patterns and the equivalent steady-state flows	98
7.1	Results of the mesh independence and validation studies study for the selected cases.	106
7.2	Physical properties used for this study	107
7.3	Comparisons between experimental and numerical breakthrough times at each flow rate.	108
8.1	Results of the mesh independence study	123
8.2	Mean results of key performance parameters and their standard deviations over five measurements for a range of section sizes and porosity variations.	126
9.1	Material properties of cyclohexane and activated carbon used in this study	141
9.2	The range of cases investigated in the study	141
9.3	Results of the validation study	142

-
- 9.4 Breakthrough time, minimum and average mean air ages at the outlet and the ratio of these. **146**
- 9.5 Correlation coefficients and linear regression coefficients between local mean air age and the average time until contamination for each case. **148**

Nomenclature

Roman

A_j	Local air age, (s)
C_e	Equilibrium concentration, (kg/m ³)
C_j	Concentration of j , (kg/m ³)
C_{in}	Inlet contaminant concentration, (kg/m ³)
C_{out}	Outlet contaminant concentration, (kg/m ³)
d_p	Particle diameter, (m)
d_b	Bed diameter, (m)
E	Porosity, (-)
f	Frequency, (s ⁻¹)
f_D	Darcy friction factor, (-)
f_μ	Turbulence damping function, (-)
I	Turbulence intensity, (-)
$J_{\alpha,i}$	Species flux, (kg m ⁻² s ⁻¹)
k	Turbulent kinetic energy, (J/kg)
K_f	Freundlich isotherm constant, (-)
K_L	Langmuir isotherm constant, (m ³ /kg)
K_M	Kinetic rate constant, (s ⁻¹)
k_T	Thermal conductivity, (W m ⁻¹ K ⁻¹)
k_{WJ}	Wheeler Jonas kinetic constant, (s ⁻¹)
L_B	Adsorbent bed length, (m)
l_t	Integral length scale, (m)
\dot{m}	Mass flow rate, (kg/s)
N	Angular velocity, (-)

n_f	Adsorption intensity, (-)
p	Pressure, (Pa)
p_e	Equilibrium partial pressure, (Pa)
p_{sat}	Saturation partial pressure, (Pa)
Q	Volumetric flow rate, (m ³ /s)
R	Ideal gas constant, (J/mol K)
Re	Reynolds number, (-)
Re_t	Turbulent Reynolds number, (-)
\bar{S}_{mi}	Mass source term, (kg m ⁻³ s ⁻¹)
\bar{S}_{ui}	Momentum source term, (kg m ⁻² s ⁻²)
$\bar{S}_{\alpha,i}$	Species source term, (kg m ⁻³ s ⁻¹)
T	Temperature, (K)
t_b	Breakthrough time, (s)
u	Velocity, (m/s)
u_s	Superficial velocity, (m/s)
u_τ	Friction velocity, (m/s)
V_L	Inlet velocity, (m/s)
W	Uptake, (-)
W_e	Equilibrium uptake, (-)
W_0	Maximum adsorption capacity, (-)
y^+	Dimensionless wall distance, (-)

Greek

α	Species fraction, (-)
ϵ	Turbulent kinetic energy dissipation rate, (J kg ⁻¹ s ⁻¹)
η	Efficiency, (-)

κ	Heat capacity ratio, (-)
μ_l	Molecular viscosity, (Pa s)
μ_t	Eddy viscosity, (Pa s)
ρ	Density, (kg/m ³)
τ	Mean air age, (s)
τ_w	Wall shear stress, (Pa)

Chapter 1

Introduction

1.1 Background

Air-purifying respirators (APRs) are respiratory protection devices designed for use in a range of hazardous environments which contain dangerous particulates, gases and vapours. In an APR contaminated air is drawn through some form of filter into a facemask to provide clean air to the wearer.

The need for respiratory protection in industrial settings dates back at least to the Roman era, when loose-fitting animal bladders were used in lead mining to prevent the inhalation of harmful lead oxides. Rapid development took place with the onset of the First World War; the extensive use of chemical weapons such as phosgene and sulphur mustard created an urgent need for a higher standard of protection, leading to the creation of the first devices resembling modern gas masks. In recent years, there has been a perceived increased threat of terrorist attacks – chemical and biological weapons and the use of radioactive materials in “dirty” bombs are now all regarded as credible terror threats. This has therefore created an increased demand for respiratory devices which provide a high level of protection for long periods in a range of hazardous atmospheres [1].

In the most widespread design of these devices, air is driven through the filter by the force of the wearers breathing. A more recent innovation of the APR design is the Powered Air-Purifying Respirator (PAPR), in which air is forced through the filter by means of an electrically powered blower [2, 3].

There are a number of benefits to the use of PAPRs over unpowered (negative-pressure) APRs. A greater degree of protection is offered, due to a positive pressure ideally being maintained within the facepiece, preventing leaks due to an imperfect seal. A greater potential driving force for air through the filter can allow more resistive filters. The constant supply of air within the facepiece provides cooling and can increase wearer comfort. For these reasons and others, the use of PAPRs has become widespread in military, emergency services and industrial applications [4].

1.2 PAPR Design

Despite this there has been relatively limited academic research on the subject of their design and improvement. For APRs generally many models common today originated a considerable time ago, and there is therefore significant scope for innovation.

1.2 PAPR Design

PAPRs typically consist of a motor and blower unit with a battery. These are connected in some way to a filter and face-piece. Many older designs have the blower and battery incorporated into a single module which is worn at the waist, and then attached to the mask via a hose. Some more modern models have all parts of the PAPR incorporated into a single mask or helmet. Within the facepiece there is also a valve which allows air to leave when the pressure within becomes high.



Figure 1.1: A representative continuous-flow PAPR (a Scott C420) [5] and a breath-responsive PAPR (a STS Shigematsu Sync01VP3) [6]

PAPRs can generally be subdivided into three major types: continuous, multi-flow, and breath-responsive. Continuous flow PAPRs simply provide a continuous supply of air at a fixed rate. This is obviously significantly draining on battery life, and the excessive air being driven through the filter at times the user is not inhaling will leave the mask via a valve without being inhaled, wasting filter life. Additionally, the users breathing rate and required air supply will depend on a wide range of factors which are in no way accounted for in a continuous flow PAPR; this can be hazardous and uncomfortable for the wearer if the provided air supply is inadequate to their needs. Multi-flow PAPRs are materially similar to continuous flow models, but include controls to adjust the air supply over a range of flow rates in order to match the wearer's breathing requirements.

Breath-responsive PAPRs adjust the air supply to match the wearers breathing rate. This allows them to not only respond to increased air-demand from the user, but also to provide air only as required throughout the inhalation stage of the breathing cycle, rather than providing unnecessary air as the wearer is exhaling. This can result in drastic increases in filter life. Breath-responsive PAPRs require a sensor for detecting when air flow is required, which usually comes via a pressure sensor which feeds back to the motor and blower. The ability to respond very rapidly to required changes in flow rate puts an extra constraint on the choice of motor and blower used, and as a result breath-responsive PAPRs are not used with more resistive filters [7].

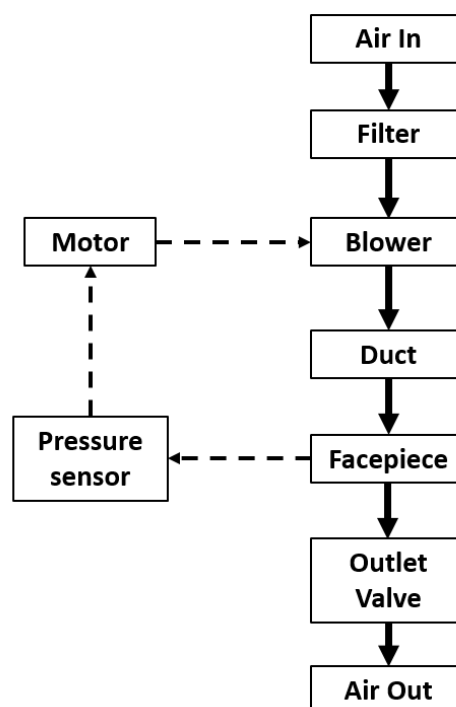


Figure 1.2: Layout of a typical PAPR. The dashed line indicates the feedback loop which is only present in breath-responsive PAPRs.

1.3 Filters

PAPRs may be used with a wide variety of filter types. Filters are selected on the basis of the target contaminant; they may protect against dusts and other particulates, airborne viruses, bacteria and other pathogens, acid gases, ammonia, chlorine, volatile organics and nerve agents, amongst others. Appropriate filter selection will ensure adequate protection while not incurring additional costs, breathing resistances and other issues [8].

Most filters can be subdivided into those which protect against particulates by physically obstructing them such as with pleated paper type filters, and those which contain an adsorbent bed. The adsorbent material used is almost always granular activated carbon; pure or near-pure carbon which has been treated in order to produce a high degree of microporosity and a subsequently extremely large surface area-to-mass ratio. It is favoured in a large variety of adsorption applications due to its low cost of manufacture and excellent adsorbent properties. Depending on the expected contaminant atmosphere, impregnants may be added; chemicals which are finely distributed on the carbon's internal surface, which will react with and immobilise the target contaminant molecule [9].

Both types of filter will degrade with sustained use. For particulate filters, the filtering material will become clogged over time with the filtered material, increasing the resulting breathing resistance. Eventually the filter will be rendered unusable and must be replaced. In adsorbent beds, there is a finite number of available adsorbent sites, depending on a number of factors including properties of the bed and the environment in which it is being used. With sustained usage, there will eventually be few too few adsorbent sites for sufficient adsorption to take place and contaminant will pass through the filter, at which point it is considered to have failed.

A special case of respirator filter canister is the Chemical Biological Radiological and Nuclear (CBRN) respirator canister. CBRN canisters have become increasingly commonplace in a wide range of defence and emergency services applications in view of an increased global terrorist threat. CBRN canisters are typically cylindrical canisters with two separate filtering chambers; a layer of High Efficiency Particulate Air filter (HEPA) at the inlet, and an impregnated activated carbon bed. In total a CBRN filter is designed to protect against 139 agents which have been identified as terrorist threats, which are summarised in Table 1.1.

Table 1.1: Summary of major threats protected against by a CBRN filter.

<p><u>Chemical Agents</u> 110 chemical gases, vapours and solid or liquid aerosols, including both chemical warfare agents and toxic industrial chemicals. These can be further subdivided as follows:</p> <ul style="list-style-type: none"> • Choking agents such as phosgene and chlorine, which impede the ability to breathe • Blood agents such as hydrogen cyanide and cyanogen chloride, which prevent O₂ and CO₂ being exchanged from the blood • Nerve agents including sarin, VX and Novichok agents, which disrupt the mechanisms of nervous signalling. • Blister agents (vesicants) such as sulfur mustard and lewisite, which cause severe chemical burns and blistering on the body and within the lungs.
<p><u>Biological Agents:</u> 13 agents. These may be disease-bearing pathogens or biological toxins in the form of solid or liquid aerosols. These include anthrax, pneumonic plague and botulism amongst others.</p>
<p><u>Radiological Agents:</u> Products of a conventional explosive used to disperse radioactive material (a “dirty bomb”) to create a long-term hazardous area</p> <p><u>Nuclear Agents:</u> Airborne radioactive particulates spread as a result of a nuclear explosion.</p> <p>There are 16 radiological and nuclear agents protected against, including Carbon 14, Cobalt 60 and Cesium 137.</p>

Due to the extremely toxic nature of the substances involved, a CBRN canister must obviously provide a high level of protection. Generally, the canister must be frequently replaced in accordance with a highly pessimistic change schedule as any breakthrough at all is unacceptable. Additionally, an APR with a CBRN canister is not suitable for use in environments where the concentration of a hazardous substance exceeds the maximum acceptable concentration, which will depend on the chemical and the protection factor of the specific model of respirator [3].

In general, the following properties are desirable in a PAPR:

- A single unit wearable on the head without a pipe to connect the blower module to the facepiece.
- Breath-responsive as opposed to continuous flow. Breath-responsive is the current state of the art in industry and gives improved battery and filter life.
- Suitable for use with a CBRN rated filter.

- Not excessively noisy.
- Capable of providing flow to match the user's maximum inhalation rate without being overbreathed. Many breath responsive PAPRs used in industry at the moment are not designed for use with physical exertion and the ensuing high breathing rates.
- Tolerant to faults.
- Lightweight.

1.4 Packed Beds

The activated carbon bed within a CBRN canister is generally composed of tightly packed spheres, typically with diameters of a millimetre or less. The packing is generally intended to provide a uniform porosity throughout the bed; however, in reality the proximity of the wall will have an effect on the packing within the near-wall region. This results in a partially ordered region extending several particle diameters from the cylinder wall. The effect of this will be greater as the ratio of the particle diameter to bed diameter is increased.

This will not necessarily be immediately apparent in a single cross-section, but when the longitudinal average of porosity is taken, a clear pattern of alternating regions of high and low porosity near the canister wall can be seen. An example of this can be seen in Fig. 1.3.

This partially structured region can produce a significant "flow-channelling" effect, in which fast flow is seen through more porous regions, potentially significantly reducing residence time.

There are a number of methods for calculating the longitudinally averaged porosity profile based on the particle and bed diameters, and the nature of the packing method. The longitudinally averaged porosity profile is insufficient to give a complete description of bed porosity, however, as random variations of porosity within the longitudinal direction will have a significant impact on the resulting flow.

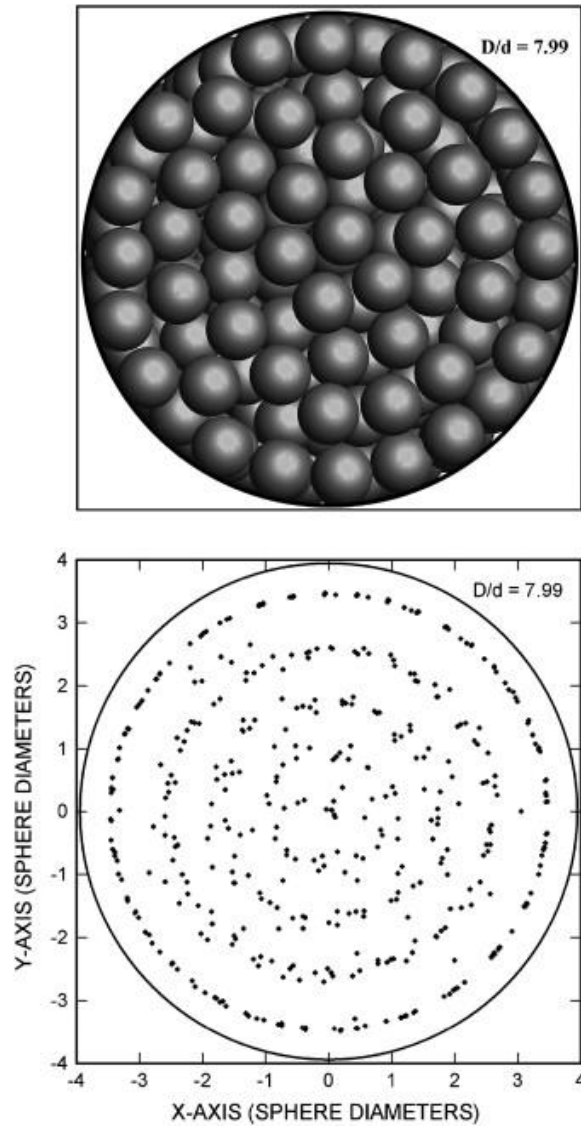


Figure 1.3: An example packing of spheres for a bed-to-particle diameter of 7.99, and the location of sphere centres [10].

1.5 Mean Air age

A key concept in understanding the distribution of flow within a respirator canister is that of mean air age, which is commonly used in applications relating to air flow and ventilation. The mean air age at a point in space (ie. the local mean air age) is the amount of time air has been resident within the system, assuming air at the inlet is entirely fresh [11]. In an experimental method, the mean air age at any point within a domain can be assessed by injecting a tracer into the inlet stream and

recording the concentration $C_j(\tau)$ within the target control volume over time. The age distribution within the control volume is therefore given by:

$$A_j(t) = \frac{C_j(t)}{\int_0^\infty C_j(t) dt} \quad (1.1)$$

The mean air age within an arbitrary control volume as a function of spatial position is found as:

$$\tau = \frac{\int_0^\infty t C_j(x, t) dt}{\int_0^\infty C_j(x, t) dt} \quad (1.2)$$

If the flow field within a domain is known, the local mean air age can be found by the solution of a transport equation.

1.6 Adsorption

Adsorption is the adhesion of molecules at a surface by physical or chemical processes. Good adsorbents typically have an extremely large surface-area to volume ratio and are often characterised by tortuous microporous structures.

There are a large number of methods used to describe adsorption processes, the selection of which will depend on the adsorbent and adsorbate used, as well as temperature, pressure and species concentrations within the system.

In general, two models are required to describe adsorption within a specific case; an isotherm, which describes the equilibrium adsorbent uptake, and a kinetic model which describes the rate at which adsorption will occur for a given vapour phase concentration and uptake.

Isotherms include a wide range of models, such as the Langmuir, BET, Freundlich and Dubinin models. These range considerably in terms of complexity and the assumptions made. For example, one of the earliest (and still most commonly used) isotherms is the Langmuir isotherm; this assumes the adsorbent material consists of a fixed number of equivalent adsorbing sites, which immobilise adsorbate a monolayer thick on its surface, without any interactions between the adsorbed material and its vapour phase. Although this is a simplification of the true physical

situation, it gives good results over a range of conditions. In contrast to this, the Dubinin-Radushkevich models consider adsorbate as a liquid filling the micropore volume, and incorporates the liquid density, pore shape and the change in Gibbs free energy associated with the phase change [12].

The kinetics of adsorption are governed by a number of mass transfer resistances, including external film resistances and resistances for transfer through macro- and micro- pores. Models may account for each of these resistances separately or group them into a lumped parameter. The most commonly used kinetic model for gas adsorption is the Linear Driving Force (LDF), which takes the mass transfer from the particle surface into pores as the rate limiting step [13].

1.7 Motivations

PAPRs offer considerable scope for improvements in terms of acceptable exposure time, degree of protection over negative-pressure respirators. In spite of this, there is very little existing literature concerning their design and optimisation. Much of the existing research on air-purifying respirators is for unpowered, negative-pressure APRs. PAPRs, particularly more modern, breath-responsive models, present their own challenges and opportunities.

Much of the potential for improvement with PAPRs lies in the filter itself. For example, it should be possible to develop a PAPR with a larger, more resistive filter than in an equivalent unpowered APR as an inexpensive blower can easily exceed the pressure differential provided by human lungs; however this is offset by the challenges associated with control and responsiveness for a breath-responsive PAPR. A better understanding of the pressure response to transient blower outputs is necessary for advanced breath-responsive PAPRs capable of using larger, longer lasting filter canisters.

Similarly, the adsorption capacity of a carbon bed is a finite resource. In order to maximise the longevity of a carbon bed, it is necessary for as many adsorption sites as possible to be occupied at the moment of breakthrough. This can only come through better understanding of flow through the bed and the resultant adsorption behaviour. While carbon bed usage may be comparatively

straightforward to predict under continuous flow, under the transient conditions of a breath-responsive PAPR, it will not be so predictable. This, in turn, presents an opportunity; a good knowledge of bed usage in response to changing flow rates may allow for control systems which take this into account in order to maximise bed usage.

While there is a reasonably large body of work concerning adsorbent beds, very little of it is directly applicable to the context of a CBRN canister. Much of the focus is on large industrial, adsorbent beds, where wall and near-wall flow channelling effects will be less prevalent. Many existing models to describe adsorption rely on the assumption of plug-flow, which is not likely to occur under the conditions of a filter canister, even without the additional flow complexities that will be introduced due to the transient nature of a breath-responsive PAPR.

1.8 Scope and Objectives

Although there is considerable scope for improvement across all components of a PAPR, this work will focus in particular on filters. Flow and adsorption performance relevant to filters will be examined in detail in order to develop a number of modelling methods and resources. This should provide a knowledge base of the fluid dynamics within a filter, which can be adapted to future filter design, with the overarching aim of developing filters capable of providing CBRN-level protection in an intelligently-controlled breath-responsive PAPR.

A number of key research objectives have therefore been identified:

- Develop better understanding of the impact filter geometry has on both pressure drop and residence time distribution, under both steady state and transient conditions.
- Relate canister performance under steady-state (easily modelled) conditions to more complex, transient flow, reducing the need for computationally expensive transient simulations in the future design process.
- Improve current understanding of porosity and its distribution within the adsorbent bed, and relate this to flow and adsorption behaviour.

- Relate the residence time distribution within the bed to adsorption and breakthrough performance.

The analysis will primarily be conducted using computational fluid dynamics simulations, with supporting validation in the form of experimental results.

1.9 Thesis Outline

The thesis is organised in the following way:

- Chapter 2 gives the full mathematical background and details of the implementation of the numerical method.
- Chapter 3 gives an in-depth review of the literature relating to flow in PAPRs.
- Chapter 4 gives a further breakdown of the individual components within a PAPR and how they can be represented within a system level model.
- Chapter 5 gives the results of a numerical study on the effects of canister geometry on performance of a CBRN canister.
- Chapter 6 gives the results of a numerical study assessing the extent to which transient CBRN canister performance may be predicted from steady state calculations.
- Chapter 7 gives the results of a combined experimental and numerical study on adsorption in small activated carbon beds.
- Chapter 8 gives the results of a numerical study on a new section-based model to more realistically describe porosity.
- Chapter 9 gives results of a numerical study investigating the relationship between mean air age and adsorption performance.
- Chapter 10 summarises the conclusions and proposes avenues for future research.

Chapter 2

Numerical Background and Modelling

Flow phenomena may be described by a series of partial differential equations describing the transport of various properties. As these transport equations are highly non-linear, they can not be solved analytically. Instead a method of discretisation and numerical solution is used. In this chapter the governing equations and numerical method used are discussed.

2.1 Governing equations

In general, the motion of any fluid is governed by conservation of mass and conservation of momentum. For flows involving heat transfer the conservation of energy must also be considered. If more than one species is present then each individual species must also be conserved.

In a turbulent flow, eddies will occur on extremely small length scales that will in turn require an extremely fine computational mesh to fully resolve. This approach is not practical for most common turbulent flows, as the computational time required would be prohibitively large. It is therefore useful to consider only the average flow, and to consider turbulent fluctuations only for their effect on the mean flow; this is done by means of the Reynolds-Averaged Navier-Stokes equations.

A variable q may be split into a mean and fluctuating component in the following manner:

$$q = \bar{q} + q' \quad (2.1)$$

where \bar{q} represents the time averaged mean value of q and q' the instantaneous fluctuation. In this way the Reynolds-Averaged equation for mass conservation is expressed as [14]:

$$\frac{\partial \rho}{\partial t} + \frac{\partial \rho \bar{u}_i}{\partial x_i} = \bar{S}_m \quad (2.2)$$

where \bar{u}_i is the velocity in the i th direction, and \bar{S}_m is the mass source term, which will depend upon the nature of the physical problem.

In the case of incompressible flow and in the absence of any source term the mass conservation equation is reduced to:

$$\frac{\partial \bar{u}_i}{\partial x_i} = 0 \quad (2.3)$$

The Reynolds averaged momentum equation in the i th direction is given by:

$$\frac{\partial}{\partial t}(\rho \bar{u}_i) + \frac{\partial}{\partial x_j}(\rho \bar{u}_i \bar{u}_j) = \frac{\partial}{\partial x_j} \left[\mu_l \frac{\partial \bar{u}_i}{\partial x_j} \right] - \frac{\partial \bar{p}}{\partial x_i} - \frac{\partial}{\partial x_j}(\rho \overline{u'_i u'_j}) + \bar{S}_{ui} \quad (2.4)$$

where μ_l is the molecular viscosity and \bar{S}_{ui} is the momentum source term. The use of Reynolds-averaging leaves the equation unclosed; the Reynold's stress term $(-\overline{\rho u'_i u'_j})$ must be modelled by an appropriate turbulence model, which will be discussed in the following section.

For a species a with mass fraction α the Reynolds averaged species conservation equation is:

$$\frac{\partial}{\partial t}(\rho \bar{\alpha}) + \frac{\partial}{\partial x_i}(\rho \bar{u}_i \bar{\alpha}) = -\frac{\partial}{\partial x_i} \bar{J}_{\alpha,i} - \frac{\partial}{\partial x_i}(\rho \overline{u'_i \alpha'}) - \frac{\partial}{\partial x_j}(\rho \overline{u'_i u'_j}) + \bar{S}_{\alpha,i} \quad (2.5)$$

where $\bar{S}_{\alpha,i}$ is the source term of species a . As with the momentum equation, this equation is left unclosed due to the $(\rho \overline{u'_i \alpha'})$ term, which requires an appropriate turbulence model. Note that for a mixture with n species it is necessary to solve species conservation for $n - 1$ species.

The transport of energy in an incompressible turbulent flow can be expressed as:

$$\frac{\partial(\rho \bar{E})}{\partial t} + \frac{\partial}{\partial x_i}(\rho \bar{u}_i \bar{E}) = \frac{\partial}{\partial x_i} \left(\underbrace{k_T \frac{\partial \bar{T}}{\partial x_i}}_{\text{conduction}} - \underbrace{\sum_a \bar{h}_a \bar{J}_{a,i}}_{\text{species diffusion}} \right) - \frac{\partial}{\partial x_i}(\rho \overline{u'_i E'}) + \bar{S}_E \quad (2.6)$$

where \bar{E} is the specific internal energy and k_T is the thermal conductivity. The Reynolds flux of energy $(\rho \overline{u'_i E'})$ also requires an appropriate closure.

2. 2 Turbulence modelling

The Reynolds stresses in the momentum equation represent additional unknowns that must be calculated if the system of equations is to be closed. A turbulence model is therefore required which sufficiently depicts the physical nature of the flow while not excessively impacting computational time. A range of turbulence models exist, which range from simple algebraic depictions of the Reynolds-stress to those which require the solution of multiple additional transport equations for individual Reynolds stresses.

The most-widely used and validated turbulence model is the $k - \epsilon$ turbulence model [15], which requires the solution of two additional transport equations, the turbulent kinetic energy k and its dissipation rate ϵ .

The turbulent kinetic energy – the kinetic energy within the flow that is due to turbulent fluctuations from the mean velocity – is defined as:

$$k = \frac{\overline{u'_i u'_i}}{2} \quad (2.7)$$

Dissipation of turbulent kinetic energy is caused by viscous stresses on the smallest eddies and its rate is defined as:

$$\epsilon = \nu \overline{\frac{\partial u'_i}{\partial x_j} \frac{\partial u'_i}{\partial x_j}} \quad (2.8)$$

The exact equation for the transport of turbulent kinetic energy is as follows:

$$\frac{\partial}{\partial t}(\rho k) + \frac{\partial}{\partial x_j}(\rho \bar{u}_j k) = \frac{\partial}{\partial x_j} \left[\mu_t \frac{\partial k}{\partial x_j} - \frac{\rho}{2} \overline{u'_i u'_i u'_j} - \overline{p' u'_j} \right] - \underbrace{\overline{\rho u'_i u'_j} \frac{\partial \bar{u}_i}{\partial x_j}}_{\text{turbulent kinetic energy generation}} - \underbrace{\rho \epsilon}_{\text{turbulent dissipation}} \quad (2.9)$$

The $k - \epsilon$ turbulence model is predicated on the assumption that losses due to the Reynolds stress are analogous to losses from viscous stresses, and therefore an eddy viscosity μ_t may be introduced. By dimensional analysis the eddy viscosity may be represented by a length scale ℓ and a velocity scale σ :

$$\nu = k^{\frac{1}{2}} \quad (2.10)$$

$$\ell = \frac{k^{\frac{3}{2}}}{\epsilon} \quad (2.11)$$

$$\mu_t = C_\mu \rho \ell \nu = C_\mu \rho \frac{k^2}{\epsilon} \quad (2.12)$$

where C_μ is a constant of proportionality which is taken to be $C_\mu = 0.09$ within the standard $k - \epsilon$ model.

The modelled transport equations for k and ϵ are as follows:

$$\frac{\partial}{\partial t}(\rho k) + \frac{\partial}{\partial x_j}(\rho \bar{u}_j k) = \frac{\partial}{\partial x_j} \left[\left(\mu_l + \frac{\mu_t}{\sigma_k} \right) \frac{\partial k}{\partial x_j} \right] + \underbrace{\mu_t \left(\frac{\partial \bar{u}_i}{\partial x_j} + \frac{\partial \bar{u}_j}{\partial x_i} \right) \frac{\partial \bar{u}_i}{\partial x_j}}_{\text{Turbulent kinetic energy generation}} - \underbrace{\rho \epsilon}_{\text{turbulent dissipation}} \quad (2.13)$$

$$\frac{\partial}{\partial t}(\rho \epsilon) + \frac{\partial}{\partial x_j}(\rho \bar{u}_j \epsilon) = \frac{\partial}{\partial x_j} \left[\left(\mu_l + \frac{\mu_t}{\sigma_\epsilon} \right) \frac{\partial \epsilon}{\partial x_j} \right] + \frac{\epsilon}{k} \left[C_{\epsilon 1} \mu_t \left(\frac{\partial \bar{u}_i}{\partial x_j} + \frac{\partial \bar{u}_j}{\partial x_i} \right) \frac{\partial \bar{u}_i}{\partial x_j} \right] - \frac{\rho \epsilon^2}{k} C_{\epsilon 2} \quad (2.14)$$

$\sigma_k = 1.1$; $\sigma_\epsilon = 1.3$; $C_{\epsilon 1} = 1.44$ and $C_{\epsilon 2} = 1.92$ are constants of the model

The Reynolds stress can then be modelled in the following manner using k and ϵ for incompressible flow:

$$-(\overline{\rho u'_i u'_j}) = \mu_t \left(\frac{\partial \bar{u}_i}{\partial x_j} + \frac{\partial \bar{u}_j}{\partial x_i} \right) - \delta_{ij} \frac{2\rho k}{3} \quad (2.15)$$

2.3 Near-Wall Treatment

The near-wall region within a turbulent flow may prove challenging to adequately depict with a RANS model, due to the presence of steep velocity gradients and the relatively large impact of viscosity damping turbulence. A number of approaches exist to represent near wall behaviour.

Over the course of this study, three approaches to near-wall treatment are considered; a standard approach in which the near-wall region is modelled algebraically, a low-Reynolds-number

approach, in which all transport equations are solved up to the wall, and a blended-wall function approach which takes aspects of each.

For steady flows, in the absence of a pressure gradient or wall curvature, there is some generality to near-wall behaviour, which makes wall-modelling possible [16]. Flow near the wall may be subdivided into regions on the basis of dimensionless wall distance y^+ :

$$y^+ = \frac{u_\tau y}{\nu} \quad (2.16)$$

where u_τ is the friction velocity:

$$u_\tau = \sqrt{\frac{\tau_w}{\rho}} \quad (2.17)$$

τ_w is the wall shear stress.

For y^+ values below 5 the flow is dominated primarily by viscous effects, and the velocity will scale linearly with wall distance. For regions in the boundary layer with a y^+ value of greater than 30 the dimensionless velocity will increase logarithmically with y^+ . Between the two regions is a buffer region which is not fully represented by either.

2.3.1 Low Reynolds-Number $k - \epsilon$ Model

The Low-Reynolds number $k - \epsilon$ fully solves all transport equations all the way to the wall. This requires the closest grid point to the wall to lie within the viscous sublayer ($y^+ < 5$), which can cause a considerable increase in the number of cells in the near-wall region. This stringent requirement can also prove difficult to guarantee with transient flows.

The low Reynolds-Number model must additionally account for viscous damping of turbulence as viscous forces dominate in the near-wall region – an effect not accounted for in the standard $k - \epsilon$ equations. This is accomplished by altering the expression of μ_t to incorporate the damping function f_μ in the following manner [17]:

$$\mu_t = f_\mu C_\mu \rho \frac{k^2}{\epsilon} \quad (2.18)$$

$$f_\mu = \exp\left(-3.4/\left(1 + \frac{Re_t}{50}\right)^2\right) \quad (2.19)$$

$$Re_t = \frac{\rho k^2}{\mu_t \epsilon} \quad (2.20)$$

2.3.2 Blended Wall Treatment

The blended-wall treatment method is designed to be applicable throughout the entire near-wall region. It combines a two-layer model which accurately depicts the near-wall flow down to the viscous sublayer for meshes that are sufficiently fine, while still giving accurate results when the first near-wall node is placed outside of the viscous sublayer [18]. It is therefore relatively insensitive to y^+ values, a desirable trait with transient flows and complex geometries.

A law-of-the-wall that is applicable throughout the entire near-wall region is necessary to achieve this. This is achieved by using a blending function Γ to blend dimensionless velocities in the laminar region (u_{lam}^+) and turbulent region (u_{turb}^+) in the following manner:

$$\Gamma = \frac{-0.01(y^+)^4}{1 + 5y^+} \quad (2.21)$$

$$u^+ = e^\Gamma u_{lam}^+ + e^{\frac{1}{\Gamma}} u_{turb}^+ \quad (2.22)$$

The near-wall region is subdivided on the basis of wall distance-dependent turbulent Reynolds number Re_y :

$$Re_y = \frac{\rho y \sqrt{k}}{\mu_t} \quad (2.23)$$

Where y is the distance to the nearest wall. For $Re_y > 200$ the flow is considered to be fully turbulent and at $Re_y < 200$ it is considered to be viscosity affected. In the fully turbulent region the

2.3 Near-Wall Treatment

transport equations for both k and ϵ are solved. In the viscosity-affected region a one equation model is instead employed, where ϵ is modelled as:

$$\epsilon = k^{\frac{3}{2}}/l_{\epsilon} \quad (2.24)$$

$$l_{\epsilon} = y C_l^* \left(1 - e^{-\frac{Re_y}{A_{\epsilon}}} \right) \quad (2.25)$$

$$l_{\epsilon} = 2C_l^* \quad (2.26)$$

$$C_l^* = \kappa C_{\mu}^{-\frac{3}{4}} \quad (2.27)$$

$$\kappa = 0.4 \quad (2.28)$$

Turbulent viscosity in the viscosity affected region no longer contains turbulence dissipation rate and is calculated from:

$$\mu_{t, nearwall} = \rho C_{\mu} l_{\mu} \sqrt{k} \quad (2.29)$$

$$l_{\mu} = y C_l^* \left(1 - e^{-\frac{Re_y}{A_{\mu}}} \right) \quad (2.30)$$

$$A_{\mu} = 70 \quad (2.31)$$

Turbulent viscosity is blended between the two-layer region and the outer region according to the following manner:

$$\mu_{t, blend} = \lambda_{\epsilon} \mu_t + (1 - \lambda_{\epsilon}) \mu_{t, nearwall} \quad (2.32)$$

The blending function λ_{ϵ} is defined to range from zero at the wall to one far from the walls:

$$\lambda_{\epsilon} = \frac{1}{2} \left[1 + \tanh \left(\frac{Re_y - 200}{A} \right) \right] \quad (2.33)$$

2.4 Numerical Method

The transport equations above were solved in Ansys Fluent [19]. This requires the pre-generation of a computational mesh with an appropriate grid spacing. The generation and selection of the mesh is conducted on a case-by-case basis as discussed in each following chapters, based around the requirements that the grid spacing does not affect the results of the calculation and that the near-wall grid spacing is appropriate for the near-wall modelling method chosen. Following this, appropriate boundary conditions are chosen.

2.4.1 Discretisation

The governing equations must then be appropriately discretised and solved. The transport equations for each variable over each cell are solved by the finite-volume method, wherein the transport equation is integrated over each cell to give a discrete of conservation for that cell. The conservation equation for a quantity ϕ with a per-volume source of S_ϕ over a control volume V with surface area A can be expressed in integral form as:

$$\rho \frac{\partial \phi}{\partial t} dV + \rho \int_A \vec{n} \cdot \vec{u} \phi dA = \int_A \vec{n} \cdot (D\nabla\phi) dA + \int_V S_\phi dV \quad (2.34)$$

By using the midpoint rule for the approximation of surface integrals, this can be converted into discrete form as:

$$\rho \frac{\partial \phi}{\partial t} V + \rho \sum_f^{N_f} \vec{n}_f \cdot (\vec{u}_f \phi_f A_f) = \sum_f^{N_f} \vec{n}_f \cdot (D\nabla\phi_f A_f) + S_\phi V \quad (2.35)$$

where N_f is the number of cell faces, ϕ_f is the value of ϕ at face f and A_f is the area of face f .

Solving this requires an assessment of face values ϕ_f via spatial discretisation and of the term $\frac{\partial \phi}{\partial t}$ via a temporal discretisation scheme.

For discretisation of the convective terms, a second-order upwind scheme is used. In this scheme, the value ϕ_f is evaluated based on the cell-centre value ϕ of the upwind-cell and its gradient $\nabla\phi$:

$$\phi_f = \phi + \nabla\phi \cdot \bar{r} \quad (2.36)$$

where \bar{r} is the displacement vector between the cell centroid and the upstream cell centroid. The gradient term $\nabla\phi$ is assessed using the least-squares cell-based method. The diffusive terms are discretised using the central differencing scheme.

For transient cases the temporal partial derivative $\frac{\partial\phi}{\partial t}$ must be evaluated for each timestep.

The second order discretisation of this for a time-step of size Δt is given by:

$$\frac{\partial\phi}{\partial t} = \frac{3\phi^{n+1} - 4\phi^n + \phi^{n-1}}{2\Delta t} \quad (2.37)$$

where the superscripts ϕ^{n-1} , ϕ^n and ϕ^{n+1} represent the value of ϕ at the previous, current and next time step respectively. As the ϕ^{n+1} term is unknown, this must be solved iteratively using an implicit method.

2.4.2 Solution method

The discretised equations can be solved using a pressure-based solver via the pressure-velocity coupling enabled by the Semi-Implicit Method for Pressure Linked Equations (SIMPLE) algorithm [20].

The velocity field is solved by the solution to the momentum conservation equations. However, the face fluxes calculated from this do not satisfy the continuity equation. The SIMPLE algorithm therefore introduces a pressure correction term to correct the velocity field. Under this method, the pressure-correction equation is solved to ensure continuity is enforced, rather than direct solution of the continuity equation [20].

In this method the coupled equations are solved sequentially so the method must be iterated until appropriate convergence criteria are met, as shown in Fig. 2.1. The method steps are as follow:

1. Update flow-field dependent properties
2. Solve momentum equations sequentially
3. Solve the pressure-correction equation for continuity

4. Update fluxes, pressure and velocity field based on pressure-correction equation
5. Solve energy, species, turbulence and other scalar equations as appropriate
6. Check convergence

2.4.3 Convergence criteria

Convergence is assessed based on the scaled residuals of each of the conservation equations used.

For a general variable ϕ the conservation equation at cell P can be expressed:

$$a_p \phi_P = \sum_{nb} a_{nb} \phi_{nb} + b \quad (2.38)$$

where a_p is the centre cell coefficient and a_{nb} the neighbouring cell coefficients and b is the cell source term. The residual, summed across the domain, is the imbalance of this equation.

The unscaled residual may be expressed as:

$$R^\phi = \sum_{cells P} \left| \sum_{nb} a_{nb} \phi_{nb} + b - a_p \phi_P \right| \quad (2.39)$$

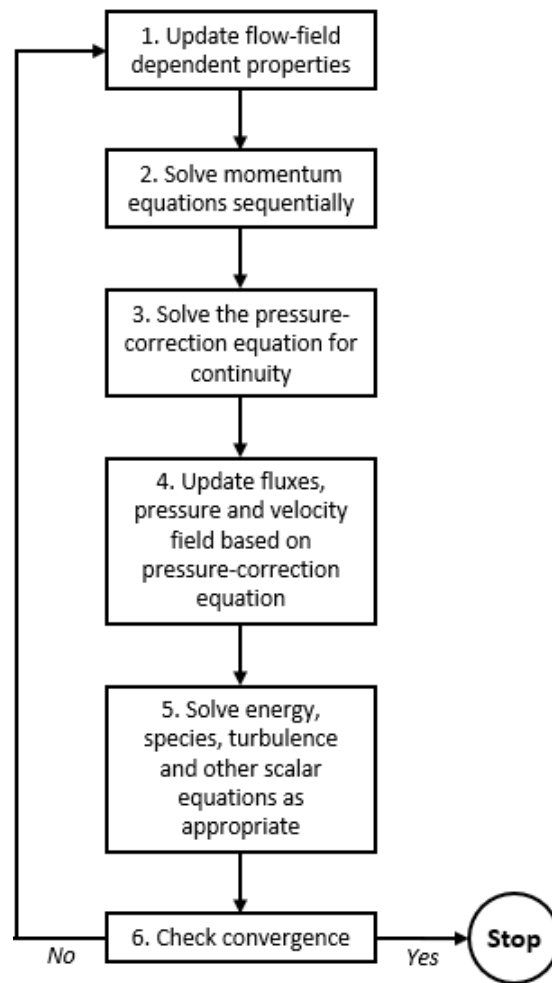


Figure 2.1: The solution scheme used for the numerical method.

This does not provide a strong indicator of convergence, however, as it will tend to increase with an increasing number of cells. The residual is instead scaled in the following manner:

$$R^\phi = \frac{\sum_{cells P} |\sum_{nb} a_{nb} \phi_{nb} + b - a_p \phi_p|}{\sum_{cells P} |a_p \phi_p|} \quad (2.40)$$

The exact residual threshold chosen varied according to the case and the variable as discussed in the following chapters.

A well-conditioned problem is required for the residual to be a useful assessment of convergence. If the coefficient matrix is well-conditioned, a small residual will be indicative of a small relative error.

2.4.4 Grid Independence

It is necessary to verify that the spacing of the computational mesh does not significantly affect the results; the mesh must be suitably refined to accurately depict the physical problem, while remaining efficient in terms of computational time.

Grid independence can be assessed systematically by defining a representative global cell size, and conducting simulations using meshes over a range of representative cell sizes. In general three mesh sizes should be used, separated by a constant refinement ratio. A parameter is then selected as indicative of overall performance and assessed for each cell size.

For representative cell sizes h_1 , h_2 and h_3 in order of increasing size, with results ϕ_1, ϕ_2 and ϕ_3 measured for each respectively, an apparent order of convergence p can be calculated as follows:

$$p = \frac{\ln\left(\frac{\phi_3 - \phi_2}{\phi_2 - \phi_1}\right)}{\ln(r)} \quad (2.41)$$

where r is the refinement ratio. A Richardson Extrapolation can be performed to estimate the true value of parameter ϕ for meshes i and j in the following way:

$$\phi_{ext}^{ij} = (r_{ij}^p \phi_j - \phi_i) / (r_{ij}^p - 1) \quad (2.42)$$

Approximate and extrapolated relative errors, e_a^{ij} and e_{ext}^{ij} , respectively for each mesh can be estimated based on this as follows:

$$e_a^{ij} = \left| \frac{\phi_j - \phi_i}{\phi_j} \right| \quad (2.43)$$

$$e_{ext}^{ij} = \left| \frac{\phi_{ext}^{ji} - \phi_j}{\phi_{ext}^{ji}} \right| \quad (2.44)$$

A fine-grid convergence index can be used to standardise reporting of grid convergence results as follows:

$$GCI_{fine}^{ij} = \frac{1.25e_a^{ij}}{r_{ij}^p - 1} \quad (2.45)$$

Grid independence is assessed on an individual basis for each of the cases investigated, as discussed in the following chapters.

Chapter 3

Literature Review

3.1 Introduction

At present there is a comparatively small body of published work concerning PAPRs. However, across the broader field of air-purifying respirators and respirator technology in general there is a considerable amount of relevant overlapping literature. In addition to this, specific PAPR components may relate to other fields in a number of ways which provides some relevant learning. In this section, the existing scientific literature is reviewed, with the intention of identifying the shortcomings of current PAPR technology and understanding how future devices might be improved.

3.2 Respiratory protection devices and their use

In this section, the main types of respirators will be compared, with a particular focus on identifying the advantages and limitations of PAPRs as compared to other respirators.

Respirators can be divided into two major categories; air-purifying (PAPRs and APRs) and air supplying such as Self-Contained Breathing Apparatuses (SCBAs) [21]. Each of these types of respirator is expected to provide user protection in a different working context, ranging from full protection in the immediate aftermath of a chemical or biological terror attack, to working in dusty environments [22].

Supplied-air respirators provide the highest degree of protection, including crucially in situations with low oxygen. However, they are heavy and bulky, and have a short service life before the pressurised air canister requires replacement. In contrast to this, air purifying respirators are generally small, light-weight and easily maintained. Though they do not provide the same type of general multi-environment protection as supplied-air respirators there are many different combinations of components available which allow the respirator to be matched to a specific situation [23].

3.2 Respiratory protection devices and their use

Air-purifying respirators should only be used over supplied-air respirators when the hazardous substance has been identified and verified not to exceed the protection factor for the specific respirator used [22]. This can be a significant challenge, as many agents, particularly chemical warfare agents, may not necessarily be detectable at a level that poses a threat. There are also concerns that detection devices are not always accessible, and that their operation in protective clothing may be difficult [24]. In the military, the use of air-purifying respirators in poorly characterised hazardous environments is widespread for a range of operational and logistical reasons [25].

Air-purifying respirators are easier to use than supplied-air respirators. In a study on the impact of a Department of Health initiative to improve preparedness for chemical incidents it was noted that there was considerable difficulty ensuring staff were adequately trained in the appropriate use of their protective equipment. It was suggested that future protective equipment should be designed with the goal of reducing the amount of preparation, testing and training required on the part of users [26].

The degree of protection provided is highly dependent on the quality of the fit. For tight-fitting respirators, good fit quality is considered to be the single most important aspect of respiratory protection, as a poor fit allows contaminants to enter via leaks in the seal. Fit-checking is therefore vitally important, and this adds to the amount of training a preparation required for APRs [27]. The requirement for a good fit with negative-pressure respirators introduces additional concerns; there is a large range of variation in human facial shapes that ensures no single facepiece will fit all users. In particular, it has been observed that some existing models of respirator are designed only for male faces, and that certain brands of respirator did not generally provide adequate fits for women [28]. For PAPRs, fit checking is still important, as a better seal will still provide a higher degree of protection. However, unlike unpowered APRs, PAPRs may still provide some level of protection with an imperfect seal [29]. PAPRs with loose-fitting hoods or helmets also provide protection to wearers who cannot get an adequate seal for reasons like facial hair and scars [23].

The type of respirator worn has an impact on the wearer safety, comfort and ability to perform tasks. For many applications, particularly military and emergency services, it is a key requirement that the choice of respirator does not excessively hinder worker performance. A study of emergency medical care providers performing simulated resuscitations either unprotected, wearing conventional APRs and wearing PAPRs found that neither form of respiratory protection significantly affected their ability to perform the task [4], although they did both equally negatively affect the degree of mobility and ease of communication. However, the users reported that the PAPR was superior in terms of breathing resistance. Health care workers who used PAPRs in a clinical context during the 2003 Severe Acute Respiratory Syndrome (SARS) outbreak were also questioned [30], with the majority favouring a PAPR to a disposable negative pressure APR.

A number of workers from the emergency services and the military were asked to perform tasks relating to trauma care in a range of different protective equipment, including chemical protective suits and gas masks. For all levels of protective equipment worn an increase in the time taken to perform tasks of 30% or greater was observed, despite the users being fully trained in its use. Generally the slowing was worsened in workers wearing gasmasks in addition to the chemical protective suits [31].

A study of subjects wearing PAPRs while performing aerobic tasks indicated that performance would be considerably reduced if airflow was inadequate [32]. Inadequate airflow also reduced comfort and caused users to overheat.

A higher degree of comfort also increases compliance with correct use. For example, there is a requirement for firefighters to also be protected by SCBA respirators during all stages of firefighting [33]. However, it has been observed that during the latter stages of firefighting (investigation and extinguishing any potential re-ignition sources) many firefighters will instead forego their respiratory protection, although there is still a considerable respiratory threat in this period.

3.3 Filter types and selection

Filters for PAPRs can take a large variety of forms and fill a wide range of different roles. In general, they take the form of a disposable cylindrical canister containing some kind of filtering media. The filtering media may be of a particulate filter type such as a HEPA filter, which is generally made of pleated paper or cloth, or it may be an adsorbent type which usually contains a packed bed of activated carbon. Some filters may contain layers of both types of media. Each filter is rated only for specific contaminants or classes of contaminants, and only rated up to a specific exposure concentration [34].

A special case of respirator canister is the chemical, biological, radiological and nuclear filter. These contain both a particulate filter towards the inlet followed by a packed carbon adsorbent bed (which contains a number of chemical impregnants targeted at specific contaminant chemicals). A CBRN filter must follow a unique and specific set of standards to protect against a far wider range of contaminants than other filtering canisters. They are widely used in industry, emergency services and defence applications [8].

A CBRN canister must pass a rigorous series of laboratory tests to verify that it provides an acceptable standard of protection. In these tests the filter is exposed to series of contaminants which represent 139 identified CBRN agents the filter must protect against. The agents can be grouped into eleven categories, based on similar adsorption characteristics and each of these groups can be represented using a single Test Representative Agent (TRA). The TRAs are all selected to be indicative of the least favourable contaminant of the group in order to ensure that results are pessimistic. The TRAs and the chemical groups they represent are as follows [35]:

- 32 Acid gases. These are typically not well physisorbed on to activated carbon due to their high vapour pressure, and must therefore be protected against means of chemical impregnants to the carbon which react with the gases. The TRAs for acid gases are cyanogen chloride, hydrogen cyanide, hydrogen sulphide, phosgene, and sulphur dioxide.
- Five nitrogen oxides, which are tested against using nitrogen dioxide.

- Four base gases, which are tested against using ammonia.
- Four hydrides, which are tested against using phosphine.
- 61 organic vapours, which includes most chemical warfare agents. The TRA for these is cyclohexane.
- 32 Particulate agents, which are tested against using dioctyl phthalate.
- Formaldehyde, which is tested using formaldehyde.

Each TRA is tested independently against an unused canister, with a fixed concentration of TRA introduced to a stream at a fixed flow rate; separate tests are carried out for each TRA at 64 l min^{-1} and 100 l min^{-1} , which broadly correspond to human average breathing rates at medium and high workloads respectively [36]. It is not representative of peak inhalation rates, which can be far higher [37]. The time taken for a threshold concentration to be crossed in the outlet stream is then measured, and the filter is then certified based on this. The breathing resistance (pressure drop) at these flow rates must also be deemed to be sufficiently low for certification.

This testing method is pessimistic, and not necessarily indicative of the true working conditions in which the filter will be used. It also provides no indication of filter efficiency. In general, when designing a filter it is desirable to maximise the total working life of the filter by ensuring that the entire adsorption capacity of the bed is used (ie. that all adsorption sites within the bed are occupied at the moment the filter fails). It is also desirable to ensure that the pressure drop across the filter is not prohibitively high under real flow conditions [38]. The pressure drop consideration is particularly significant for breath-responsive PAPRs, for which high pressure drops will challenge the blower response time [39, 40].

3.4 CFD for CBRN canisters

Improvement and optimisation of respirator canisters requires an improved knowledge of the flow throughout under real working conditions. Even within a simple cylindrical adsorbent bed domain there is considerable scope for optimisation; characteristics such as inlet and outlet placement, the distribution of porosity and the relationship between flow distribution and adsorption performance

will all have a considerable impact on adsorption performance. For a single canister geometry, performance may vary if introduced to a variable flow rate, or it may vary greatly from one choice of contaminant to the next.

Increased understanding of flow through a canister should allow optimisation of existing CBRN canister designs and may produce tools that can be used to better design novel filter designs, such as those that better conform to the face or may be worn within a helmet.

The use of computational fluid dynamics (CFD) may provide valuable insights to flow performance in a respirator canister. Insights into the relationship between flow and canister performance can be gained from a number of observations. Simple inspection of flow structures and streamlines gives some suggestion as to the location of dead zones or routes of preferential flow [41]. Numerical methods can also give accurate predictions for pressure drop across a filter [42].

The residence time distribution can also be used to give an indication of adsorption performance. Within a CFD simulation this can be identified by solution of the transport of mean air age τ by the following equation:

$$\frac{\partial}{\partial t}(\rho\tau) + \frac{\partial}{\partial x_j}(\rho\bar{u}_i\tau) = \frac{\partial}{\partial x_j}(\mu_{eff} \frac{\partial \tau}{\partial x_i}) + \rho \quad (3.1)$$

where $\mu_{eff} = \mu_l + \mu_t$, and μ_l and μ_t are the molecular and eddy viscosities respectively. The mean air age represents the average amount of time air will have spent within the domain at each location. While it does not give a perfect indication of adsorbent usage, it is widely used to give some indication of the “freshness” of air [43-45].

One CFD study modelled a CBRN canister that has been widely used since the 1970s [45]. The canister was configured with two layers of filtration separated by brackets perforated with several holes, a common canister design. The study measured experimental pressure drops for each filtration layer at a range of flow rates. It was noted that throughout most of the expected range of flow rates the pressure drop across the domain was dominated by viscous resistances; only at higher flow rates did inertial losses become significant. Viscous and inertial pressure loss parameters for

each of the filtering media were then used as the basis of a CFD study to identify how the placement of holes in the bracketing between the separate layers affected residence time distribution and pressure drop. It was noted that there was considerable scope for filter optimisation by simply modifying the hole distribution.

A similar study used computational fluid dynamics as a design tool for optimising CBRN canister design and compared CFD models to experimental data. The CFD studies showed a good match to experimental data. It was shown that the pressure drop could be reduced by up to 50% designing the airways between filtration layers such that the velocity of air entering the carbon bed was reduced (hence lowering the inertial resistance). It also showed considerable scope for some designs to reduce dead zones and improve carbon utilisation [46]

CFD can not only be used to predict characteristics of the filter itself, but also the physiological response of the wearer. By measuring the heart rates of test subjects wearing respirators, it has been shown to be possible to predict the influence of respirator breathing resistance on the wearer's heart-rate. This can then be used in conjunction with CFD pressure drop analysis to design respirators that minimise the increase in heart rate. This could also be used to predict the workload under which wearer's would transition into anaerobic respiration, which would significantly increase fatigue [47].

Another CFD study demonstrated the influence simple functional modifications to a respirator canister could have on the outcomes, observing the difference to pressure drop and flow distribution that could be seen when an explosion-resistant plate was added to an existing canister design [48].

3.5 Adsorption in activated carbon beds

Activated carbon has been used in a huge range of industrial contexts over many decades as an adsorbent for an extremely wide range of chemicals. Its strength as an adsorbent lies in the processes of its formation. Carbonaceous compounds are at first carbonised by heating at temperatures below 800°C in an inert atmosphere, eliminating volatile species and causing the residual carbon to form,

3.5 Adsorption in activated carbon beds

irregularly arranged, cross-linked sheets which have many free interstices within their structure, which form into pores. The porous nature can then be further enhanced by the activation process, which is carried out by heating a stream of air or CO₂ to selectively oxidise some regions and enhance the porous nature by selectively oxidising and etching throughout the carbon. This results in an extremely large internal surface area which is capable of adsorbing a large number of chemicals by a number of mechanisms [49].

Adsorption onto activated carbon requires understanding of the thermodynamic driving force, and the kinetics. The thermodynamics are generally described by means of an adsorption isotherm, which describes the equilibrium uptake of contaminant at a given temperature and concentration.

Experimentally, for vapours, an adsorption isotherm is often calculated by exposing a known weight of carbon to a chemical at a known concentration, and recording the change in mass of the carbon after sufficient time has taken place for equilibrium to be reached. This is done over a wide range of concentrations to give the full isotherm [50]. Other methods exist, such as a volumetric method in which the pressure reduction in a sealed chamber is measured as adsorption takes place to indicate how much total vapour has been adsorbed [51].

Adsorption data may be fitted to a wide number of isotherm equations. These isotherms vary greatly in terms of their ease of estimation, complexity, number of required parameters, applicable range of concentrations and applicable range of target molecules [52]. Isotherms also exist for the description of multicomponent systems, where there is competition for available adsorption sites [53].

The oldest and one of the most widely used adsorption isotherms is the Langmuir isotherm [54]. This model is predicated on assumptions that molecules striking a vacant adsorption site are immediately completely immobilised. It assumes all surface sites are equivalent and that the surface is entirely homogeneous [55].

On the basis of these assumptions, the Langmuir isotherm can be expressed to give the equilibrium uptake W_e (kg/kg) as follows:

$$W_e = \frac{W_0 K_L C_e}{1 + K_L C_e} \quad (3.2)$$

where C_e is the equilibrium contaminant concentration (kg/m^3), W_0 is the maximum capacity of the carbon (kg/kg) and K_L is the Langmuir isotherm constant (m^3/kg). An advantage of the Langmuir equation is that it can be easily linearised as:

$$\frac{1}{W_e} = \frac{1}{W_0} + \frac{1}{W_0 K_L C_e} \quad (3.3)$$

which facilitates easy retrieval of parameters from experimental results from a plot of $\frac{1}{W_e}$ as a function of $\frac{1}{C_e}$ [56]. The assumptions underpinning the Langmuir isotherm do not generally give an accurate depiction of the physical picture. However, in a limited range of contexts the Langmuir isotherm gives a good enough representation of experimental data to remain useful [57-59]. Simple modifications to account for surface heterogeneity and changing desorption rates with concentration allow its range of applicability to be significantly increased [60].

Another comparatively simple isotherm equation is the Freundlich equation, which accounts for heterogeneity of the adsorbent surface. The Freundlich isotherm can be expressed as:

$$W_e = K_f C_e^{n_f} \quad (3.4)$$

where K_f (kg/kg) is the isotherm constant and n_f is the adsorption intensity. K_f incorporates the adsorption capacity of the adsorbate. n_f gives an indication of the strength of the adsorption process [56]. As with the Langmuir isotherm, the Freundlich equation does not give an entirely accurate depiction of the true physical situation, and is somewhat limited in its applicability; in particular it tends to fail at high partial pressures where the assumption of only a single layer of adsorbate is no longer valid [61]. However, it still gives a good match to experimental data over a number of cases

3.5 Adsorption in activated carbon beds

[62, 63]. Models also exist which combine aspects of both the Langmuir and Freundlich isotherms to better fit experimental data [64].

A more recent development is the Dubinin-Radushkevich isotherm [65]. This model is based upon the theory that pores become filled with the adsorbed material, rather than the layer by layer modelling used in other models [66]:

$$W_e = \rho_L W_0 \exp \left[- \left(\frac{RT}{\beta E_0} \right) \ln \left(\frac{p_{sat}}{p_e} \right)^2 \right] \quad (3.5)$$

where ρ_L is the density of the adsorbed material in the liquid phase, βE_0 is the adsorption energy and p_{sat} and p_e are saturation and equilibrium partial pressures respectively. The Dubinin-Radushkevich equation has shown to be particularly effective for adsorption on activated carbon and other carbonaceous substances [67]. A number of modifications exist to this, such as the Dubinin-Astakhov equation which extends its range of applicability to better cover non-carbonaceous adsorbents, such as zeolites [68]. While the Dubinin-Radushkevich equation is useful in a range of contexts it generally does not perform well for highly volatile substances [69].

A thermodynamic model alone is not sufficient to fully model adsorption; while it indicates the uptake once equilibrium occurs, it does not take account of factors that will limit the rate of adsorption. At extremely low contaminant concentrations, particularly in cross flow problems, adsorption is sometimes considered to occur instantaneously at the point of first exposure, and the contaminant then proceeds through the carbon by Fickian diffusion. This approximation can be used to model the behaviour of CBRN protective garments in low-contaminant concentrations. However, at higher contaminant concentrations and with flow proceeding through a bed this approximation is likely to be inaccurate and the contaminant will travel far faster in the vapour phase [70].

Adsorption kinetics are often governed by a single rate limiting step. For activated carbon, this is usually the mass transfer of adsorbed material on the surface deeper into the particle in order

to free a surface adsorption site. In this case the adsorption kinetics can be considered to be first order, with the adsorption rate given as [71, 72]:

$$\frac{dW}{dt} = K_M(W_e - W) \quad (3.6)$$

where K_M is the rate constant. A number of other adsorption processes are governed by second order kinetics as follows:

$$\frac{dW}{dt} = K_M(W_e - W)^2 \quad (3.7)$$

Activated carbon beds are widely used in industry for the purpose of cleaning contaminated streams. Generally a stream of fluid which contains a contaminant is passed through a packed bed of particles of activated carbon. A study of an industrial gas adsorption column for the extraction of hexafluoropropylene found that for designing an adsorbent column it was far more important to have an accurate adsorption isotherm than kinetic model; in this case the use of the Dubinin-Raduskevich isotherm over the Langmuir isotherm substantially improved the accuracy of results, whereas there was a relatively low sensitivity to kinetic parameters [73]. A separate study investigated the breakthrough behaviour of phenol through an activated carbon bed. Breakthrough is investigated by measuring concentration of a contaminant in the outlet stream of a packed bed [74]. Typically no contaminant will be seen in the outlet stream (or the contaminant will be below a chosen or detectable threshold) for some long period of time. This period of time will depend upon the adsorption isotherm and by kinetics. When breakthrough occurs the outlet concentration will begin rising. The rate at which the outlet concentration will rise is dictated by the extent of dispersal in the axial direction of contaminant within the bed; this in turn is directed by the adsorption kinetics. Slow kinetics will tend to lead to more dispersal of the contaminant (ie. a long region at the front of the contaminated region which is partially contaminated, but below the equilibrium uptake concentration). With slow kinetics and a more dispersed contaminated front, the rate of increase of contaminant concentration at breakthrough will be shallow. If the kinetics are fast, the rate of increase of contaminant in the outlet stream will be steep, and the time to

breakthrough will depend primarily upon the adsorption isotherm with little influence from kinetics. A less dispersed front will make more efficient use of the carbon bed before breakthrough [75, 76].

For large, industrial adsorbent beds it is often assumed that the contaminant moves through the bed via a plug flow. In reality, there will be a small boundary layer near the wall, but for a sufficiently large bed diameter this may be treated as negligible [77]. For a defined breakthrough threshold concentration C_{out} , the time t_b taken for breakthrough of a plug flow can be calculated by performing a mass balance of contaminant over the length of the adsorbent bed to give the Wheeler-Jonas equation:

$$t_b = \frac{\rho_B W_e}{C_{in} V_L} \left[L_B - \frac{V_L}{k_{WJ}} \ln \left(\frac{C_{in}}{C_{out}} \right) \right] \quad (3.8)$$

where ρ_B is the bed bulk density, L_B the bed length, V_L the inlet velocity and k_{WJ} the overall kinetic constant. For some non-plug flow cases, the shape of the front of contaminant passing through the bed will remain relatively unchanged over the length of the bed. In such cases the Wheeler-Jonas equation may still be used to give a good indicator of breakthrough performance by modifying the value of k_{WJ} to account for the shape of the front [78]. In reality, the extent of axial dispersion may vary over the length of the bed, leading to deviation away from the predicted breakthrough time seen in Eq. 3.8 in deeper beds [79]. There is also a limitation in very shallow beds, where the breakthrough time will be under predicted by the Wheeler-Jonas equation [80]. Despite these limitations, with accurate kinetic and dispersion data the Wheeler-Jonas equation is useful over a wide range of applications, and can be relatively reliably extended to broader circumstances, such as adsorption in multi-vapour systems [78].

In respirator canisters the geometry involved is far more complex and aspects such as inlet placement, bracketing and the low length to diameter ratio will prevent the flow from being an ideal plug flow throughout the bed. The Wheeler-Jonas equation will therefore not be strictly applicable [81]. Attempts have been made previously to develop simple models to depict breakthrough behaviour of filters. For a known contaminant and known concentration with sufficient

experimental data for a specific model of filter, models have been developed to predict breakthrough time over a range of flow rates [82], and extended to incorporate additional phenomena such as binary contaminant systems. However, such models require a very large amount of experimental data and are somewhat limited in terms of what can be predicted.

In a respirator canister there may also be a number of impregnants within the activated carbon bed designed for the immobilisation or extraction of contaminants which do not so easily adsorb to the carbon. For example, hopcalite (a mixture of copper and manganese oxides) is commonly used to catalyse the oxidation of carbon monoxide into carbon dioxide [83]. Inorganic metal oxides are frequently used to extract chemical warfare agents. For example, CuO can be used for the adsorption and decomposition of sulphur mustard and nerve agents [84].

3.6 Porosity in packed beds

A widespread issue in packed-bed systems is the influence of the container walls on the distribution of the packing material; some degree of structure will generally be seen close to the walls and particles will no longer be uniformly distributed. This results in areas of high and low porosity in the near wall region which can be seen when the porosity is averaged over the length of the bed [10]. This will have an impact on the distribution of flow through the bed, often resulting in a phenomenon known as “wall-channelling” in which the faster flow will occur in the near wall region [85].

A number of attempts have been made to characterise this near wall behaviour. Experimental studies have been conducted in which a packed bed has been filled with wax or resin and then slices extracted and the porosity over each measured [86, 87]. Alternatively, methods such as radiography may be used to sample beds remotely [88]. For a given bed and particle diameter the exact distribution of porosity between individual packing realisations will vary significantly.

The longitudinally-averaged porosity profiles may be described by either empirically or theoretically derived models. A semi-empirical model can be used to describe the porosity profile simply by an exponential expression [89]:

$$E = E_0 \left(1 + C_E \exp \left(1 - 2 \frac{R-r}{d_p} \right) \right) \quad (3.9)$$

Where E is the average porosity at radius r for a bed of radius R and a particle diameter d_p and C_E is an experimental tuning parameter. This model has the advantage of fairly accurately predicting the high velocities seen close to the wall but does not model oscillations of porosity further from the wall. Other models better represent the oscillating behaviour by use of a cosine function [90, 91], although none of these models remain entirely accurate across the entire radius of the bed.

A good representation of porosity distribution can be seen by use of an analytical method, using a Bessel function to describe the oscillations.

$$E_p = E_b(1 - E_b)e^{-br}J_0(ar^*) \quad (3.10)$$

where J_0 is a zero order Bessel function of the first kind and a, b, r^* and E_b are described as follows:

$$a = 7.45 - \frac{3.15d_p}{d_b} \text{ for } 2.02 \leq \frac{d_b}{d_p} \leq 13.0 \quad (3.11)$$

$$a = 7.45 - \frac{11.25d_p}{d_b} \text{ for } 13 \leq \frac{d_b}{d_p} \quad (3.12)$$

$$b = 0.315 - \frac{0.725d_b}{d_p} \quad (3.13)$$

$$E_b = 0.365 + \frac{0.220d_p}{d_b} \quad (3.14)$$

$$r^* = \frac{r}{d_p} \quad (3.15)$$

This method has been shown to give a good match to experimental measurements over a range of circumstances [92, 93].

Longitudinally averaged models are an important tool in the analysis of packed beds but do not necessarily provide a complete picture. In reality, the random variations in porosity over the length of the bed will have a significant impact on flow throughout which will not be fully described by a longitudinally averaged model [94].

Detailed depictions of packed beds can be created by the use of discrete element method (DEM) simulations, in which the position of each individual particle can be found by calculating individual forces on each particle over time as the bed is packed. This results in a highly detailed model of the packed bed. However, such modelling is highly complex and time consuming, so is not practical for beds with a large number of particles in many applications [95].

An alternative approach has been a section-based model of porosity, which is seeing increasing use in the modelling of trickle-bed reactors, in which a liquid and a gas are passed simultaneously through packed beds [96]. In this method, the bed is divided into discrete sections, and each of these sections is assigned a local porosity according to a longitudinally averaged model such as Eq. 3.10. The local porosity is then modified according to a probability distribution function (PDF). The section size and PDF may be assessed by the use of Magnetic Resonance Imaging of the bed [96], or estimated based on empirical results [85, 97, 98].

3.7 Conclusions

A review of the existing literature suggests that PAPRs can provide significant benefits over other types of respirator, in terms of ease-of-use, safety and comfort. However, there is still significant scope for improvements, such as modifying CBRN filters to be more compatible with breath-responsive PAPRs and increase their functioning life. In particular this might be achieved by gaining a better understanding of which aspects of the filter geometry have the most significant impact on the pressure drop and adsorption performance. It would also be useful to develop tools to make estimates of performance under the transient conditions seen in breath-responsive PAPRs from continuous-flow data.

It has been found that CFD can be a valuable tool for improving filter design. A number of challenges persist in reliably modelling CBRN filters, such as poor understanding of the relationship between the widely used mean air age and adsorption. There are also issues pertaining to the distribution of porosity, where there is scope for learning from the modelling of other packed bed applications, such as trickle bed reactors.

Chapter 4

System-Level Modelling

A breath-responsive PAPR is composed of a number of separate components; the performance of each of these is heavily coupled with the performance of the others. In addition to this, external factors such as temperature, local air pressure, the extent of filter blockage and the users breathing rate can all have impact the performance of this device. For this reason, it is useful to have a system-level depiction of a PAPR that will indicate how varying any of a large number of performance parameters will impact the key outputs.

MATLAB Simulink [99] was used to build a modular framework in which each of the key components of the PAPR can be represented as single module with a number of inputs and outputs. Each of these can then be replaced or improved upon as further models are developed for each component. The existing system model is designed to depict a non-specific generic breath responsive PAPR and uses a number of estimated parameters and simplified calculations.

4.1 System Model Components

The primary input for the system level model is the wearers breathing requirement, which may be specified as a function. On the basis of this a large number of parameters throughout the PAPR are evaluated over time. For the current model the instantaneous breathing flow rate was approximated as a sinusoidal curve in the following manner:

$$Q_{req} = Q_{peak} \sin\left(\frac{2\pi t}{f_{breath}}\right) \quad (4.1)$$

where Q_{peak} is the peak inhalation flow rate and f_{breath} is the breathing frequency and the values of these will depend on the individual and their current workload [37].

The PAPR components which are included in the system-model are the inlet, the filter, the blower (incorporating the motor and battery), the pipe or ducting and the facepiece. Descriptions of the current depictions of these are detailed below[23].

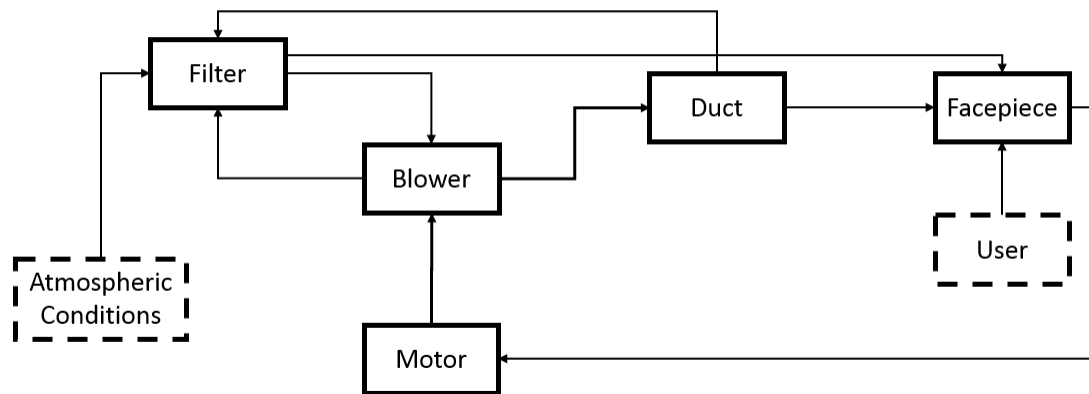


Figure 4.1: The individual modules of the system-level model and simplified indications of the flow of data between them.

4.1.1 Filter

Inputs:

- p_{atm} Pressure from atmosphere
- ρ_{atm} Air density from atmosphere
- p_{face} Pressure within facepiece
- T_{atm} Temperature from atmosphere
- Q_{blow} Volumetric flow rate from blower
- p_{blow} Pressure from blower

Outputs:

- p_{filter} Filter outlet pressure to blower
- T_{filter} Filter outlet temperature to blower
- \dot{m}_{filter} Inlet mass flowrate to mask

Module parameters:

- Q_{ref} Reference flow rate
- Δp_{ref} Reference pressure drop
- A_{filter} Filter cross sectional area

The model assumes that no air is leaked out of the system prior to entering the mask. This means that at any point in time the mass flowrate of air is known throughout the system.

The pressure at the blower outlet is known as described below. According to the ideal gas law the density of air can be expressed as:

$$\rho = \frac{p}{RT} \quad (4.2)$$

4.1 System Model Components

The volumetric flowrate at the inlet can be calculated based on the volumetric flowrate at the blower as

follows:

$$Q_{atm} = \frac{T_{atm} p_{blow}}{T_{blower} p_{face}} Q_{blow} \quad (4.3)$$

For existing filters a reference pressure drop is provided for a reference flow rate. Darcy's law for pressure drop through a porous medium gives an estimate for the pressure drop over a range of flow rates based on this, in which case pressure drop is proportional to the mean velocity (i.e. $\Delta p \propto u_m \propto Q/A$, where u_m , Q and A are the mean velocity, volumetric flow rate and filter area, respectively), which leads to [100]:

$$\Delta p_{filter} = \frac{\Delta p_{ref} Q_{atm}}{Q_{ref}} \quad (4.4)$$

For a given filter a pressure drop is specified at a reference flowrate. This allows the actual pressure drop Δp_{filter} to be evaluated where Q_{filter} is the volumetric flowrate through a single filter. It is assumed that the flow is split equally between the two filters. The temperature change across the filter can be derived from the steady-state energy equation[101]:

$$c_p (T_{filter} - T_{atm}) = \frac{1}{2} \left(\frac{\dot{m}}{\rho_{atm} A} \right)^2 \left[1 - \left(\frac{p_{atm}}{p_{filter}} \right)^2 \left(\frac{T_{filter}}{T_{atm}} \right)^2 \right] \quad (4.5)$$

4.1.2 Blower Motor

Inputs:

- p_{face} Pressure in facepiece

Outputs:

- N_{imp} Filter outlet pressure to blower

Module parameters:

- ΔN_{up} Impeller ramp-up rate
- ΔN_{down} Impeller ramp-down rate
- p_{set} Facepiece set pressure

The motor dictates the impeller speed and is governed according to a set pressure in the mask. If the facepiece pressure is above the set pressure the motor will ramp down linearly; if it is below it will ramp down linearly.

$$N_{imp} = N_{imp}^{ts-1} + \Delta t \Delta N_{up} \quad \text{for } p_{face} \leq p_{set} \quad (4.6)$$

$$N_{imp} = N_{imp}^{ts-1} - \Delta t \Delta N_{down} \quad \text{for } p_{face} > p_{set}$$

4.1.3 Blower

Inputs:

- N_{imp} Impeller speed from motor
- T_{filter} Temperature from filter
- p_{filter} Pressure from filter

Outputs:

- p_{blow} Blower outlet pressure to duct
- T_{blow} Blower outlet temperature to duct
- Q_{blow} Blower volumetric flow rate to filter and duct

Module parameters:

- A_0, A_1, A_2 Blower coefficients
- Δp_{refb} Reference pressure rise
- Q_{refb} Reference flow rate
-
- T_{refb} Reference torque
- N_{refb} Reference impeller speed
- η_{blow} Blower efficiency
- η_{mot} Motor efficiency

The blower is rated for a specific volumetric flowrate, pressure increase, impeller speed and torque (Q_{refb} , N_{refb} , Δp_{refb} and T_{refb}). The value of these parameters at any other speed N can be related to the rated values as follows [102]:

$$\frac{Q_N}{Q_{refb}} = \frac{N}{N_{refb}} \quad \frac{\Delta p_N}{\Delta p_{ref}} = \frac{N^2}{N_{refb}^2} \quad \frac{T_N}{T_{refb}} = \frac{N^2}{N_{refb}^2} \quad (4.7)$$

The flowrate leaving the blower is therefore calculated from:

$$Q_{blow} = \frac{N_{imp} Q_{refb}}{N_{refb}} \quad (4.8)$$

Each blower will have a pressure-discharge relationship described by a characteristic flow curve.

The pressure-discharge relationship for the blower can also be expressed in a quadratic form:

$$\Delta p = a_0 + a_1 Q + a_2 Q^2 \quad (4.9)$$

where a_0 is the pressure at no flow and a_1 and a_2 are constants which can be estimated from the flow curve.

4.1 System Model Components

By applying the homologous relationships to the pressure-discharge equation the pressure increase at any impeller speed is found [102]:

$$\Delta p_N = a_0 \left(\frac{N_{imp}}{N_{refb}} \right)^2 + a_1 \left(\frac{N_{imp}}{N_{refb}} \right) Q_N + a_2 Q_N^2 \quad (4.10)$$

When the pressure in the mask rises above the set point the motor is cut off. Since the impeller still has some momentum it will still provide a flow and pressure increase as given by Eq. 4.10.

The power drawn by the motor is treated as rising linearly with motor speed from 0 up to the rated power at full speed for simulation purposes. In reality, this will depend on specific details of the motor and impeller.

Blower Efficiency:

In general the pressure change can be estimated if the motor and blower efficiency and power are both known as follows. The maximum possible efficiency that can be achieved by a compression process is given by the work required for an isentropic process. It can be shown that this work is [101]:

$$\dot{W}_{isen} = p_1 Q_{in} \frac{\kappa}{\kappa - 1} \left[\left(\frac{p_2}{p_1} \right)^{\frac{\kappa-1}{\kappa}} - 1 \right] \quad (4.11)$$

where \dot{W}_{isen} is the blower power requirement for an isentropic process, Q_{in} is the volume rate of air displaced at the blower inlet, and p_1 and p_2 are the pressures at the inlet and outlet respectively.

In the above equation κ is the ratio of heat capacities of air which is taken to be 1.4.

This can then be compared to the actual power drawn by the motor \dot{W}_{actual} using the overall efficiency of the motor and blower. This is a combined efficiency for both, so losses may be attributable to either the motor or the blower:

$$\eta_M \eta_b = \frac{3.5 Q_{blow} p_{filter}}{\dot{W}_{actual}} \left[\left(\frac{p_{blow}}{p_{filter}} \right)^{0.283} - 1 \right] \quad (4.12)$$

The temperature T_s that would result if the process were isentropic is as follows:

$$T_s = T_{filter} \left(\frac{p_{blow}}{p_{filter}} \right)^{\frac{k-1}{k}} \quad (4.13)$$

This can be used with the efficiency to calculate the actual outlet temperature:

$$T_{blow} = T_{filter} + \frac{T_s - T_{filter}}{\eta_b} \quad (4.14)$$

4.1.5 Duct/Pipe

Inputs:

- p_{blow} Pressure from blower
- T_{blow} Temperature from filter
- Q_{blow} Flow rate from blower

Module parameters:

- L_{pipe} Pipe length
- d_{pipe} Pipe diameter
- Q_{refb} Reference flow rate

Outputs:

- p_{pipe} Pressure to facepiece and filter
- T_{pipe} Temperature to facepiece

Pressure losses due to flow between individual components must be accounted for. Within the present model, a configuration with a pipe connecting a separate filter/blower module worn at the waist to the facepiece.

Flow in PAPRs is invariably low Mach-number and incompressible. The pressure loss due to viscous effects in the pipe can be estimated from the Darcy-Weisbach equation [103]:

$$\frac{\Delta p_{pipe}}{L_{pipe}} = \frac{f_D \rho u_{pipe}^2}{2d_{pipe}} = f_D \frac{\dot{m}^2}{2\rho d_{pipe} (\pi d_{pipe}^2/4)^2} \quad (4.15)$$

where f_d is the Darcy friction factor for a smooth pipe which is dependent on the Reynolds number,

Re :

$$Re = \frac{\rho u_{pipe} d}{\mu} \quad (4.16)$$

$$f_D = \frac{64}{Re} \quad \text{when } Re < 2000 \quad (4.17)$$

4.1 System Model Components

$$\frac{1}{\sqrt{f_D}} = -2 \log \left(\frac{2.51}{Re \sqrt{f_D}} \right) \text{ when } Re > 4000 \quad (4.18)$$

In the transition between laminar and turbulent flow the friction factor is not easily calculated so it is estimated by linear interpolation between the friction factors at Reynolds numbers of 2000 and 4000. This correlation for the friction factor was chosen as it can be easily modified to account for non-smooth pipes.

There is an additional hydrostatic pressure loss due to the height difference between the blower and the mask. Due to the small height involved this is also treated as incompressible and is given by:

$$\Delta p_{hydro} = \rho g L_{pipe} \quad (4.19)$$

4.1.6 Facepiece

Inputs:

- N_{imp} Impeller speed from duct
- T_{pipe} Temperature from filter
- p_{pipe} Pressure from pipe
- \dot{m}_{lung} Breathing rate from lungs
- p_{atm} Pressure from atmosphere

Outputs:

- p_{face} Facepiece internal pressure to motor

Module parameters:

- V_{face} Facepiece internal volume
- Δp_{refb} Reference pressure rise
- k_d Outlet valve discharge coefficient
- f_{breath} Breathing frequency
- A_{out} Outlet valve area

There are four sources of air into and out of the mask:

- The blower, which provides a flow in response to a pressure reading in the mask as described in Section 4.1.3.
- The outlet valve, which will allow no outwards flow below a fixed set pressure. When this set pressure is exceeded the valve will discharge at a rate given by:

$$Q_{out} = k_d A_{out} \sqrt{\frac{(p_{mask} - p_{atm})}{2\rho_{mask}}} \quad (4.20)$$

where k_d is the discharge coefficient which is dependent on the valve and A_{out} is the area of the outlet valve.

- Leakage out of the mask seal. This is not included in the current model, and will depend significant on the quality of the wearers face seal.
- The lungs, which will add or remove air according to the wearers breathing. In general, a good approximation of a human breathing pattern takes the following form:

$$Q_{req} = Q_{peak} \sin\left(\frac{2\pi t}{f_{breath}}\right) \quad (4.21)$$

- where Q_{peak} and f_{breath} are the peak inhalation flow rate and the breathing frequency respectively, which will depend on the wearer and their current workload.

The simulation begins with the model containing a mass of air required to approximately produce atmospheric pressure. The pressure in the mask is evaluated according to the ideal gas law.

The airflow into or out of the mask from each source is evaluated at each time interval. At the start of the next time interval the mass of air in the mask is known and the new pressure is evaluated.

The temperature in the mask is taken as the temperature at the outlet of the blower, which has been calculated upstream. Future updates to the model will take into account the impact of the lungs on the condition of the air.

4.2 Uses and limitations of the existing physical model

Many of the variables that feed into the system-level model will vary greatly on a design-by-design basis and are generally not widely documented. There is a high degree of sensitivity to many of the key parameters.

One major output of the system-level model is the pressure inside the mask under a range of conditions. There is a stringent requirement for PAPRs that a positive pressure must be maintained within the mask at all time in order to prevent inward leakage. A fully developed system-model

4.2 Uses and limitations of the existing physical model

should be able to identify when this condition is breached. An example of this behaviour is seen in Fig. 4.2, where a single parameter, the reference pressure drop across the filter has been increased by just 20%, resulting in an unacceptable negative pressure within the facepiece.

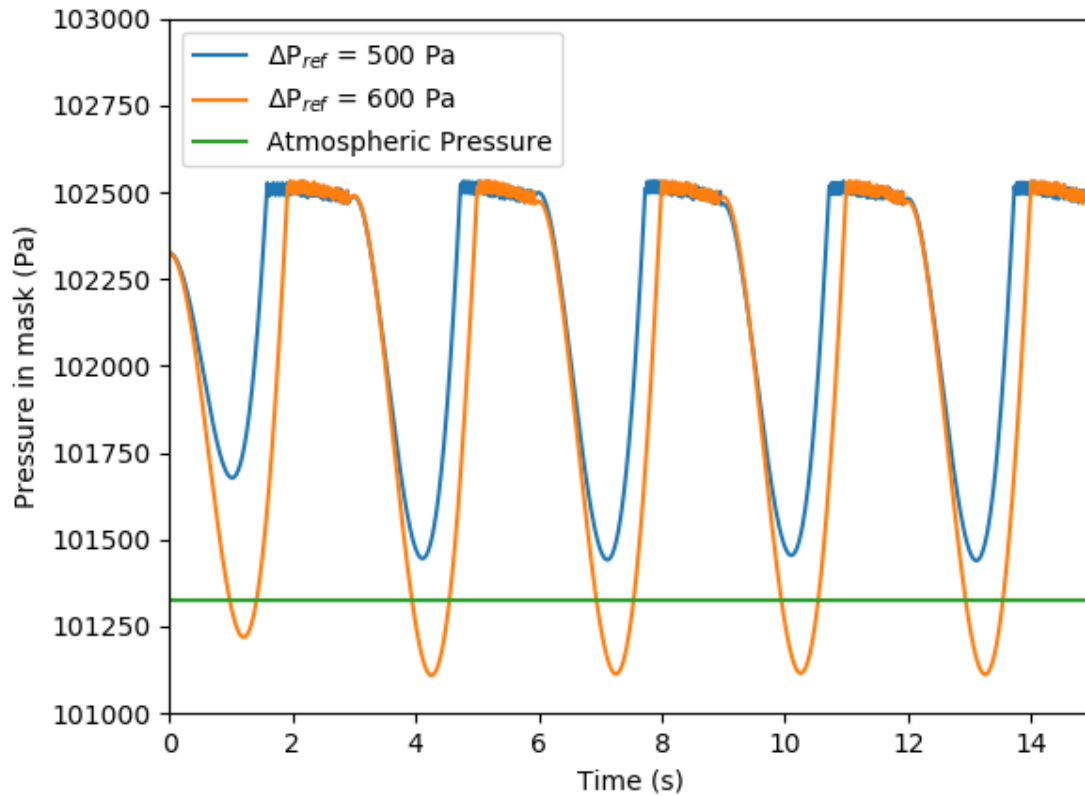


Figure 4.2: Example pressure response seen from the system-level model to a single changing parameter (the reference pressure drop across the filter).

There are a large number of assumptions and simplifications within the current system level model, which can be considered on a component by component basis.

4.2.1 Filter

There are a significant number of limitations within the filter module:

- The assumption that the pressure drop will increase linearly with flow rate is dubious. Eq. 4.4 is only true for a uniform porous bed under steady flow conditions dominated only by viscous losses. In reality, as the flow rate increases inertial losses will become significant and these losses scale quadratically with velocity.

- Losses will also be affected by the nature of the porous medium. Eq. 4.4 is not necessarily valid with non-uniform porosity profiles.
- There is no consideration given for increasing losses due to clogging of the filter will occur in particulate laden atmospheres.
- There is no estimate of filter lifetime or contaminant breakthrough. This is of vital importance for PAPR performance but at present there is no suitable method for clearly predicting breakthrough under a transient flow.

4.2.2 Motor and Blower

As with the filter, the impact of transience on the blower is not well accounted for in the current model. It is assumed that the homologous relationship seen in Eq. 4.10 remains true even as the impeller accelerates or decelerates, which will not necessarily be the case. In the present model the power drawn is also taken to rise linearly with the instantaneous impeller speed, which will not necessarily be accurate and depend upon the specifics of the motor, impeller and battery.

There is no means to disentangle the motor and impeller efficiencies with the current model, and it is therefore assumed that the motor efficiency is 100%, with all losses being within the blower.

4.2.3 Other losses

The current model assumes the blower and filter module are connected to the facepiece by means of a hose, which is barely the case in modern breath-responsive PAPRs. It also assumes a lack of leakage throughout the system. While there is scope to improve the model to incorporate additional losses, these losses are anticipated to be extremely small relative to the filter, blower and breathing rates.

4.2.4 Facepiece

A significant limitation with the existing model is a lack of inclusion of loss of air through an imperfect seal; as a PAPR is expected to maintain a positive pressure within the mask at all times there is likely to always be some air lost in this manner.

4.3 Summary of the System-level model

A partial system-level model has been developed with the intent of identifying the key factors which influence PAPR performance and the areas in which further development is needed. The model is highly modular and individual modules may be updated as better understanding of the relevant components is developed. The filter in particular has been identified as an area in which existing understanding is relatively poor and should be the subject of further investigation.

Chapter 5

Effects of Geometry on Performance of a CBRN Canister

In this chapter, steady-state axisymmetric RANS simulations have been carried out in order to optimise the performance of a CBRN canister filter for its use in a PAPR. Alterations have been made to the shape of the canister, the spacing of the rear wall of the canister with regard to the carbon filter, and the bracketing between (i) the particulate filter and the carbon bed and (ii) the carbon bed and the canister wall. The pressure drop across the canister and the residence time distribution at the rear of the carbon bed have been analysed in detail based on an extensive parametric analysis involving the aforementioned variations.

The steady state simulations were used to inform selection of three transient cases which were analysed in more detail with respect to the mean air age distribution throughout the carbon bed over the duration of a single breath.

5.1 Background

Computational Fluid Dynamics (CFD) has been used in the past as a method of predicting the performance of CBRN protective equipment [70]. It has also been previously used to optimise filters for a number of industrial applications, and has shown good results when used to predict performance in pleated filters similar to those used at the inlet of a PAPR canister [42, 104]. Three-dimensional CFD simulations have been used to analyse the flow features in CBRN filter canisters in a past study [105], in which a large range of flow rates were considered. The results of these simulations were also compared to experimental measurements of pressure drop throughout the canister and a good agreement between experimental and computational results was reported. Additionally, the bracketing used to contain the carbon bed was modified in a number of small ways (closing and opening holes in the bed) to explore the impact this would have on both the residence time of air in the bed and on the pressure drop throughout the canister [105]. It was found that small optimisations on the bracket hole distribution can have significant impact on the performance of

5.1 Background

the canister. However, the variations to the canister geometry made in this work were limited only to the hole placement in the bracket and stopped short of more substantial changes to the canister geometry. The work was also carried out based on an assumption of uniform permeability throughout the carbon bed which does not necessarily give an accurate picture of the internal structure of the canister [105].

Axisymmetric simulations were carried out based on another design of CBRN canister with the intent of developing a model to describe adsorption throughout the canister [106]. In this work a radial porosity profile based on the longitudinally averaged Mueller equation was implemented to better describe the packing distribution of carbon throughout the carbon bed, which is described in the Chapter 3.

The purpose of the analysis in this chapter is to consider different axisymmetric geometries of CBRN filter canisters to analyse the effects of geometrical variations on the performance of the filter in terms of pressure drop across it and the residence time distribution at the rear of the carbon bed within the filter. This is achieved by carrying out steady-state RANS simulations for a flow rate which is often realised in continuous flow PAPRs, and for breath-responsive PAPRs under the normal breathing pattern of a healthy individual [46]. For CBRN filters to be used with transient flows, continuous flow tests are commonly used to provide a good, if not comprehensive, indication of canister performance, and are used for canister performance testing in NIOSH specifications [35]. The flow rate of 50 L/min was chosen based on a past study [107] which indicates that this is the most representative continuous flowrate for canister testing. The typical axisymmetric filter geometry considered here is shown in Fig. 5.1.

The mathematical background and numerical implementation pertaining to this analysis will be presented in the next section. Following this, results will be presented along with the discussion. The main findings are summarised in the final section of this chapter.

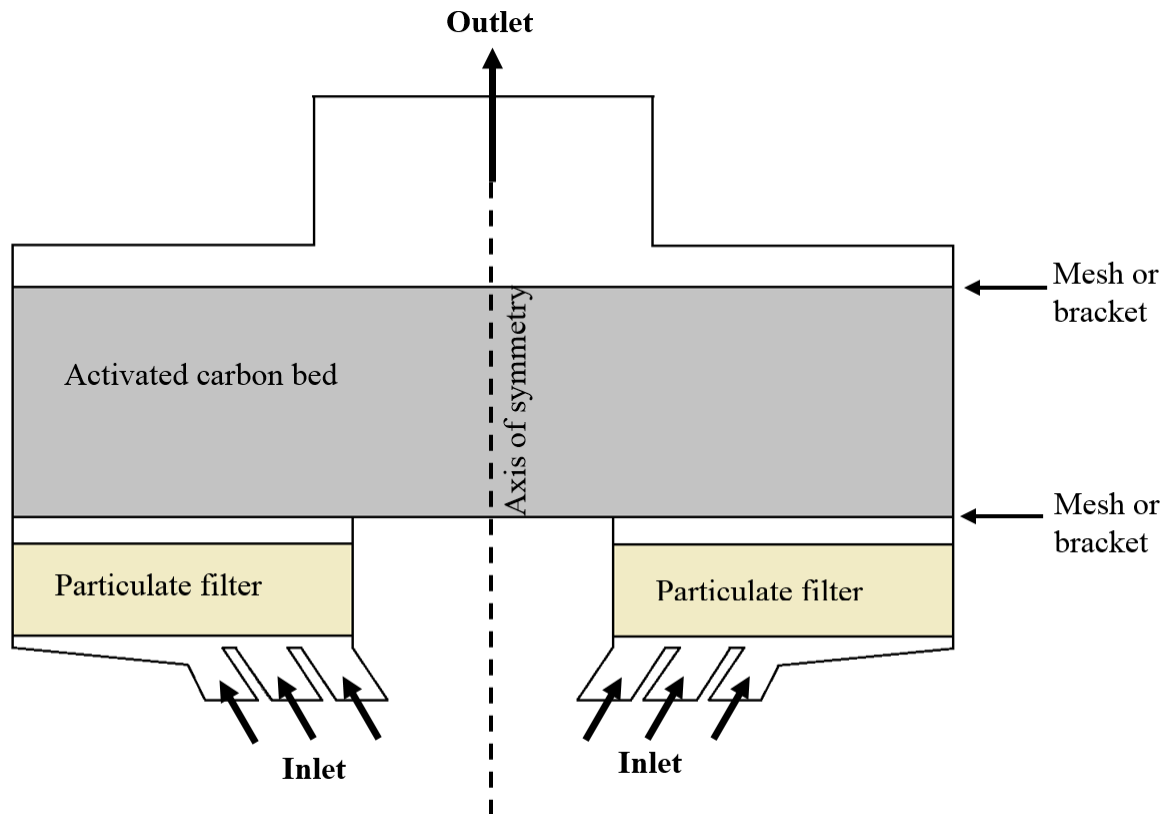


Figure 5.1: Cross section of a typical CBRN filter design.

5.2 Mathematical Background

For the current analysis, steady-state Reynolds-averaged Navier-Stokes (RANS) simulations have been carried out by solving the Reynolds-averaged Navier-Stokes equations for mass and momentum conservation [108]. Turbulence is modelled using the low Reynolds-number $k - \epsilon$ turbulence model, as described in Chapter 3 (Eq. 3.15 and Eq. 3.16).

5.3 Configurations

A number of different variations has been made to the baseline CBRN canister design [106] shown in Fig. 5.2, and these variations are schematically shown in Fig. 5.3. This geometry was selected as it represented a typical CBRN canister without any novel features, and there is an existing body of work available on adsorption throughout the canister which could be applicable to future work using variations of this geometry [106]. A schematic representation of the simulation domain is shown in Fig. 5.2. This domain represents a filter such as that shown in Fig. 5.1 rotated by 90 degrees and considering only one half with respect to the axis of symmetry for the sake of computational

5.3 Configurations

economy. This design features three separate inlets leading into a chamber containing two separate layers of filter with a small gap between them, as shown in Fig. 5.3. These simulations allowed for fluid flow across the entire domain without representing the internal bracketing that holds the filters in place. The following changes are made to the baseline geometry (see Fig. 5.3(a)):

- Brackets between the carbon and particulate filter: Two different sizes of bracketing are used, with 3mm spacing (see Fig. 5.3b) and 6 mm spacing (see Fig. 5.3c).
- Extending the rear of the canister past the back of the carbon filter, leaving a space between the carbon and the narrowing of the outlet. Two different lengths of extension are used: 2 mm (see Fig. 5.3d) and 6 mm.
- Curving the outer wall of the canister towards the outlet (see Fig. 5.3e) with a 10 mm radius of curvature.
- Curving the inner wall of the canister towards the outlet (see Fig. 5.3f) with a 10 mm radius of curvature.
- Brackets to the rear of the carbon filter (at the outlet), in the cases where the rear of the canister has been extended by 6 mm. Two different sizes of bracketing are used, with 3 mm spacing (see Fig. 5.3(g)) and 6 mm spacing (see Fig. 5.3h).

All possible variations of these changes to the geometry have been simulated, leading to a total of 60 cases.

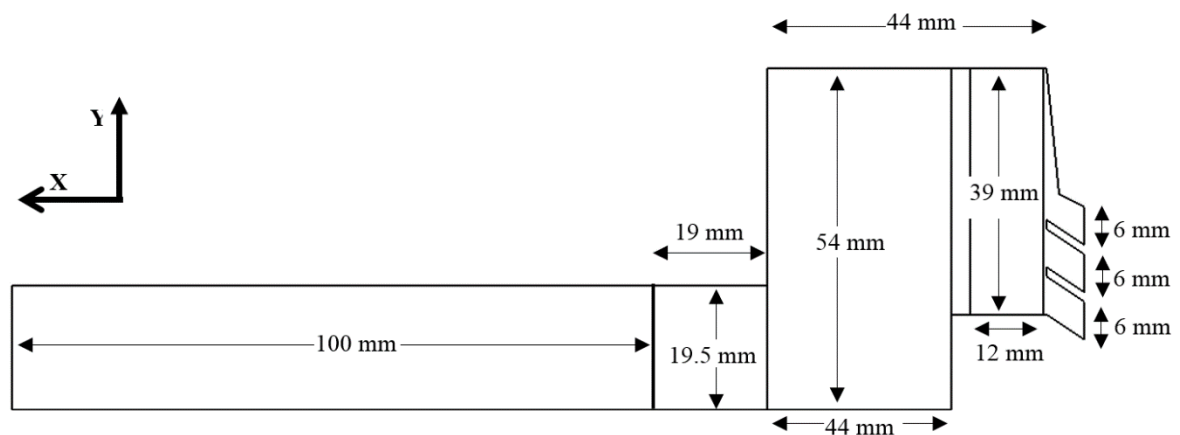


Figure 5.2: Schematic diagram of the computational domain for the baseline geometry.

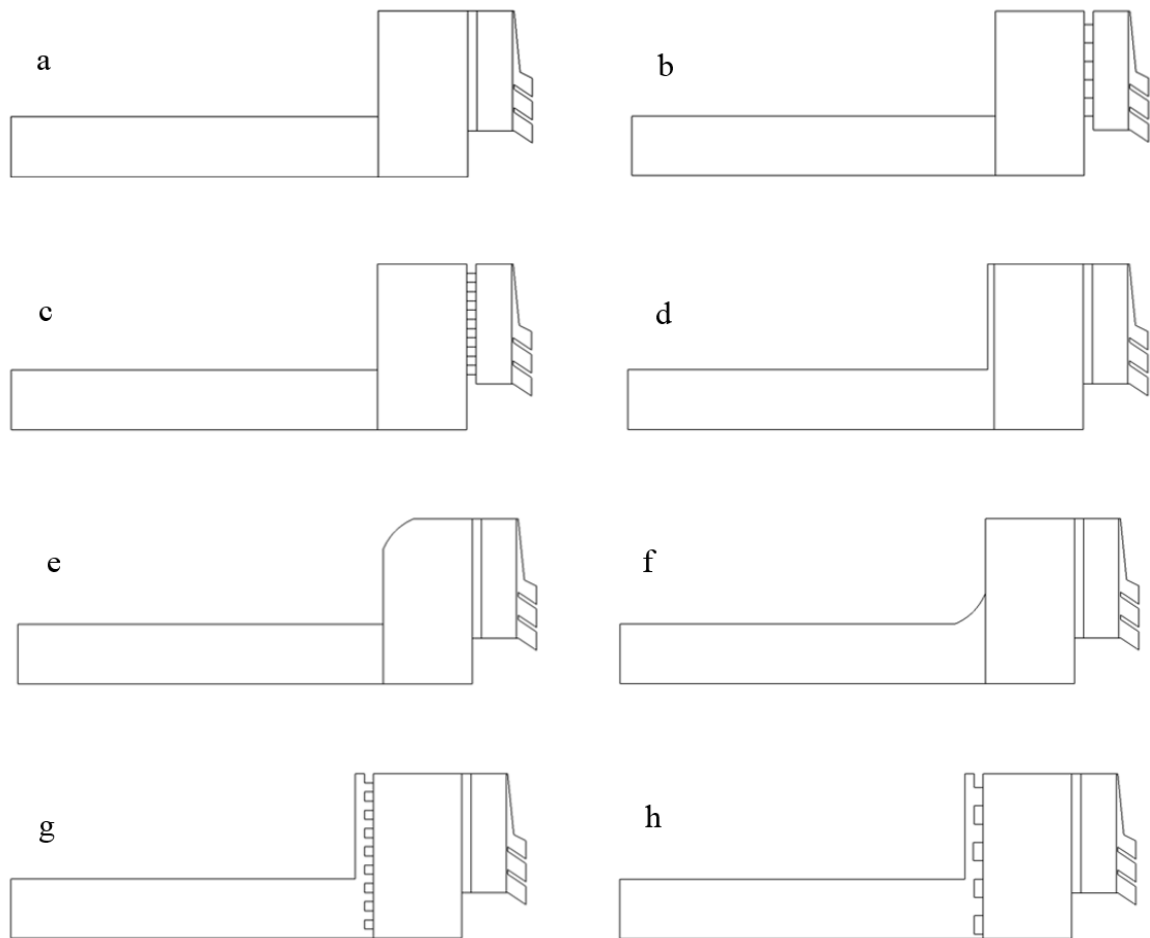


Figure 5.3: Summary of the variations of the canister geometry considered here: the base case (5.3a), two sizes of bracketing before the carbon filter (5.3b and 5.3c), spacing between the carbon filter and the canister wall (5.3d), curvature of the canister outer wall (5.3e and 5.3f) and two different sizes of bracketing after the carbon filter (5.3g and 5.3h).

5.4 Mesh Independence

For the aforementioned 60 variations, the mesh independence of the results has been ensured using both coarse (Mesh A) and refined (Mesh B) Cartesian meshes with non-uniform grid spacing. The grid spacing remains small close to the wall in order to resolve the boundary layer and to ensure that the maximum $y^+ = \rho u_\tau \Delta / \mu$ remains smaller than 5.0 but the grid spacing gradually increases away from the wall. The number of grid points, grid spacing and grid expansion ratio for the meshes used for this analysis are summarised in Table 5.1. For five cases (each separate type of spacing or bracketing at the rear of the canister) an additionally refined mesh (Mesh C) was considered in order to provide an additional level of verification of mesh independence. For each geometry, mesh independence was ensured by checking that both the coarse and refined cases gave equivalent values of pressure drop from the inlet to the outlet, and mean air age at the rear of the carbon filter,

5.5 Filter Modelling

to within 1%. For the other geometries the number of cells in each mesh did not vary substantially from that used in the base case.

Table 5.1: Key characteristics for each of the meshes used to establish grid independence.

Case	Target element length in carbon region (m)	Target element length in rest of canister (m)	Max number of inflation layers	Inflation layer growth ratio	Inflation layer transition ratio	Number of cells in base case
Mesh A	3×10^{-4}	4.5×10^{-4}	10	1.05	0.272	70625
Mesh B	2.7×10^{-4}	4.05×10^{-4}	12	1.05	0.272	85323
Mesh C	2×10^{-4}	3×10^{-4}	15	1.05	0.272	155563

5.5 Filter Modelling

The filter material in a respirator filter canister is usually modelled as a porous medium [106]. The canister contains two layers of filtration media; a pleated particulate filter near the inlet to stop particulates, followed by a layer of carbon, which acts as an adsorbent. The carbon bed is held in place by bracketing or a mesh above and below. A 2D schematic of a typical filter design is shown in Fig. 5.1.

The pressure drop across the porous media of the two filter layers is described by the Forchheimer equation, Eq. 5.1 [106]:

$$(-\Delta\bar{p}/L) = a_1\bar{u}_s + a_2\bar{u}_s^2 \quad (5.1)$$

where a_1 and a_2 are the parameters which depend upon the specific medium, \bar{u}_s is the superficial velocity of the fluid, and the overbar refers to the mean quantities. The superficial velocity for a porous medium may be defined as $u_s = E_p u$ where E_p is the local porosity. The term $a_1\bar{u}_s$ describes the pressure loss associated with viscous effects and $a_2\bar{u}_s^2$ describes the pressure loss due to inertial effects. At lower flow rates, the viscous term dominates and the inertial term may often be neglected [46]. The cases examined here use sufficiently low flow rates that the inertial term may be neglected.

The permeability of the particulate filter may vary over time as the particulate loading increases, although in this study it was treated as clean. The permeability of the particulate filter was chosen as $2.5 \times 10^{-9} \text{ m}^2$ to correspond to a pressure drop of 40 Pa across the particulate filter seen in Smith [106].

The permeability of activated carbon in respirator filters is not well-documented and varies from filter to filter. One estimate for the permeability can be expressed with the help of the Ergun equation, which finds the permeability as a function of the local porosity [100].

The carbon filters are packed using the “snowstorm” filling technique to maximise the packing efficiency [109]. This results in a porosity profile that varies radially throughout the bed, oscillating between high and low porosity near the wall before converging to a uniform porosity near the centre of the bed. This behaviour is described by the empirical Mueller equation [110]. The relevant equations describing the porosity distribution are presented in Chapter 3 (Eq. 3.10). The pressure drop can be related to the porosity by means of the Ergun equation [100]:

$$(-\Delta\bar{p}/L) = \frac{150\mu_L(1 - E_p)^2}{d_p^2 E_p^3} \bar{u}_s + 1.75 \rho \frac{(1 - E_p)}{d_p E_p^3} \bar{u}_s^2 \quad (5.2)$$

A key parameter in assessing canister performance is the pressure drop across the filter, as increased pressure drop can lead to increased power requirement for the blower or diminished flow rate. The pressure drop was measured by taking the difference of the area-weighted average of the mean pressure values at the inlet and the outlet.

The time until breakthrough of the challenge substance is the other key indicator of canister performance. This is related to the residence time distribution of air in the carbon filter. An estimate for the average residence time, τ , can be found using the air age equation within the canister (Eq. 3.1) [44].

For optimum filter usage, all of the adsorption sites present should be occupied at breakthrough and breakthrough would occur simultaneously across the whole outlet of the carbon filter. It is therefore important to know exactly how much the residence time varies radially across

the outlet of the carbon filter. The distribution of residence time in the carbon has therefore been analysed at the outlet of the carbon filter, and the mean air age distribution, minimum mean air age and the standard deviation of mean air age have been analysed in detail.

5.6 Numerical Implementation and Boundary Conditions

The coupled mass, momentum and age equations are solved in the framework of finite-volume technique using Ansys Fluent, with full details of the numerical method used given in Chapter 2. A scaled residual threshold of 10^{-6} is considered to be the convergence criteria for all the variables considered here.

The simulations have been conducted under the assumption of axisymmetry based on a geometry considered in the past for practical applications [106].

In many of the simulations, a large zone of flow recirculation was seen close to the outlet after the final corner, causing some reverse flow at the outlet, so the length of the outlet pipe was increased. Key characteristics such as the mean pressure drop were still evaluated using true outlet location, rather than the extended simulation outlet.

Although human breathing rates vary considerably, the flow rate was selected based on the most typical case. A constant inlet flowrate of 50 l min^{-1} was chosen for all simulations, as it represents a breathing rate under moderate labour [107]. This equates to a mean velocity of 1.80 m/s at the inlet. Steady-state simulations were used due to the drastic reduction in computational time compared to transient flow, and have previously been shown to give a good indication of canister performance [105, 107]. The Neumann boundary condition has been used at the outlet boundary, such that each primitive variable does not change normal to the boundary. All the walls are considered to be no-slip boundaries and thus the velocity components tangential to the wall are considered to zero. The velocity components normal to the walls are also zero due to impenetrability of the solid walls.

Turbulence at the inlet is described by two parameters, turbulence intensity $I = u'/U$ and the integral length scale $l_t = C_\mu k^{3/2}/\epsilon$ where $u' = \sqrt{2k/3}$ is the root mean square of velocity fluctuations, U is the mean inlet velocity, and the integral length scale at the inlet was chosen as: $l = 0.07d$ where d is the canister diameter [106] and verified by a sensitivity analysis. Three different turbulence intensities (i.e. 2%, 10% and 20%) have been considered for the base geometry, which showed there is a very small change in pressure drop (i.e. less than 1.0%) even when the turbulence intensity changed by an order of magnitude. This is a result of the dampening of inlet turbulence close to the inlet. Thus, a turbulence intensity of 10% at the inlet has been chosen for the purpose of parametric analysis.

The turbulent kinetic energy is identically zero (i.e. $k_{wall} = 0$) at the wall and the dissipation at the wall is specified as $\epsilon_{wall} = 2\nu(\partial\sqrt{k}/\partial n)^2$ in the context of low Reynolds number $k - \epsilon$ turbulence model [42]. It is worth noting that wall conditions are not used in the context of the low Reynolds number $k - \epsilon$ model and both k and ϵ are solved all the way up to the wall. This requires adequate resolution of the viscous sub-layer of the turbulent boundary layer. It was ensured that the maximum non-dimensional wall distance $y^+ = \rho\sqrt{\tau_w/\rho}\Delta/\mu_l$ remains smaller than 5 (i.e. $y^+ \leq 5$) for all cases considered here (where Δ is the wall normal distance of the grid point next to the wall and $\sqrt{\tau_w/\rho}$ is the friction velocity with τ_w being the wall shear stress).

5.7 Data Analysis

The impact of changing each parameter was assessed by carrying out a factorial analysis of variance study, which gives an indication of the significance of each parameter with regard to each response variable, [111] as well as any interaction between parameters. The parameters and levels and the labels used for them are shown in Table 5.2.

Table 5.2. Geometric parameters varied and their respective levels used in the analysis of variance study.

Parameter	Levels
Outer canister curve	Curved (CO), Straight (SO)
Inner canister curve	Curved (CI), Straight (SI)

Spacing at rear of carbon	No gap, 2 mm gap, 6 mm gap, 6 mm bracket spacing in 6mm gap, 3 mm bracket spacing in 6 mm gap
Bracketing between paper and carbon	No bracket (N), 6 mm bracket spacing (B), 3 mm bracket spacing (fB)

5.8 Validation

Experimental results for pressure drop over a wide range of flow rates across an existing canister filter (shown in Fig. 5.4) were reported in Li [105]. These results were used to provide validation for the CFD methodology used in this analysis. However, it is worth noting that the geometry shown in Fig. 5.4 is not axisymmetric and thus 3D simulations have been carried out for this configuration. However, the same numerical methodology that has been used for 2D axisymmetric cases shown in Fig. 5.3 were employed for 3D simulations in order to compare the pressure drop with respect to the experimental results reported in Li [105]. Two different mesh sizes were used for 3D simulations and mesh independence was verified.

The boundary conditions used in the 3D simulations were the same as those used for the axisymmetric cases. Two cases were modelled; one in which a fixed permeability was used and one, which used a radial porosity profile, described by the Mueller equation, using a fixed carbon bead size of 0.8 mm. The fixed permeability was found experimentally by measuring the pressure drop throughout both the filter paper and the carbon bed independently and fitting them to the Darcy equation. The parameters used in this study can be seen in Table 5.3.

Table 5.3: Permeabilities of the materials used for the 3D simulations

Material	Permeability (m^{-2})
Filter paper	1.52×10^9
Carbon	2.39×10^9

The pressure drop across the canister was measured at 50 l min^{-1} , and is shown in Table 5.4. Both the fixed permeability and the Mueller porosity profile slightly under-predict the experimental results but come close enough to suggest that this methodology gives a good indicator of the actual performance, with the Mueller equation giving the more accurate prediction. There is a small difference between the results found here and the results seen in Li [105]. This minor difference

may have arisen due to the fact that a small screw in the canister geometry has not been accounted for in the current simulations.

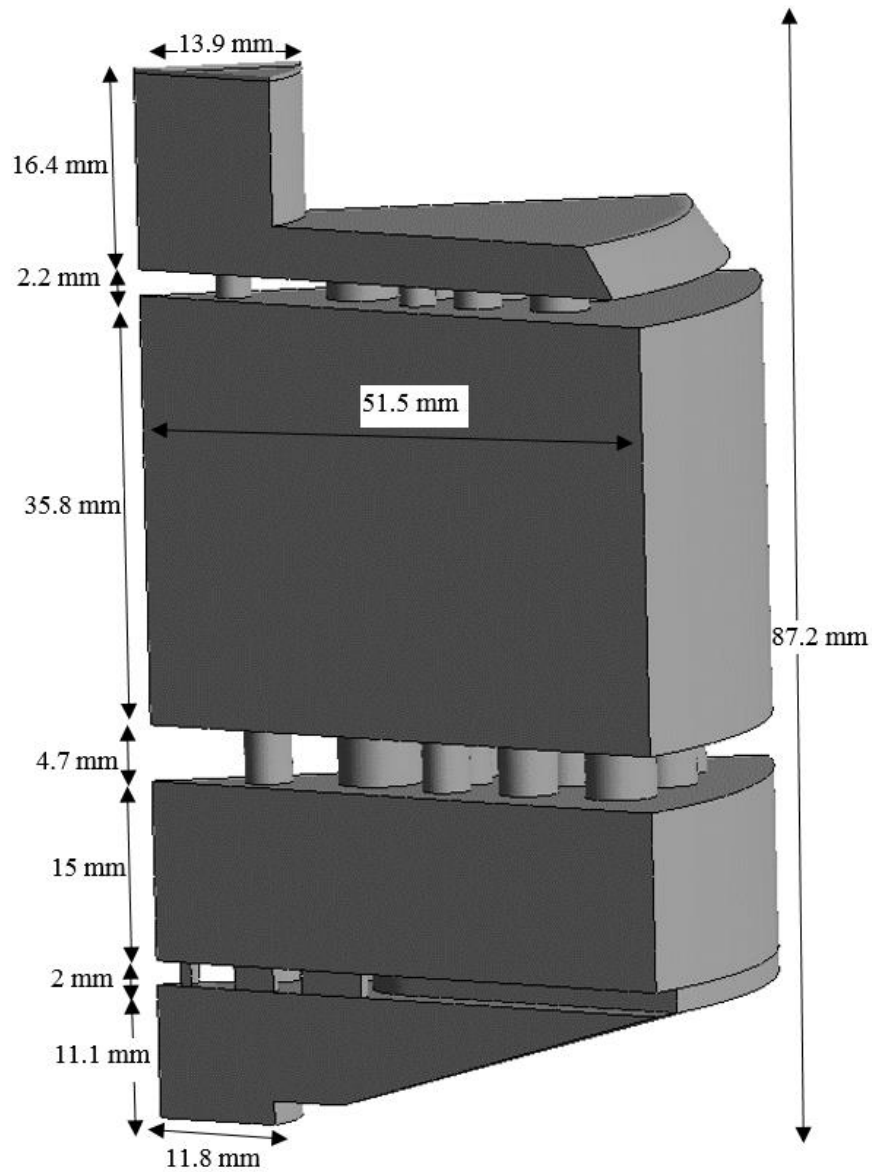


Figure 5.4: Geometric configuration of canister modelled for 3D simulation.

Table 5.4: Experimental and computational pressure drops across the 3D simulation for a flow rate of 50 L/min.

Case	Pressure drop (Pa)
Experimental	250
Fixed carbon permeability	225
Carbon porosity described by Mueller equation	241

Typically, an axisymmetric model takes of the order of one hour to converge on the computational hardware given in Table 5.5, in contrast to approximately seven hours for the 3D simulations. For this reason, axisymmetric simulations were favoured when a large number of variations to the geometry were desired.

Table 5.5: Hardware used for CFD simulations.

CPU	Intel i7-6700K, (8 CPU cores at ~4GHz)
GPU	NVIDIA Quadro K620 4GB
RAM	32 GB DDR3

5.9 Results of the Steady State Analysis

5.9.1 General Flow Features

In general, a large pressure gradient has been observed throughout the porous media in all cases, with a very small pressure gradient throughout the empty canister. The pressure profile seen throughout the carbon bed depends largely on whether or not the carbon backs directly onto the canister back wall, or if a space is left between the carbon and the canister wall.

As shown in Fig. 5.5, in cases where there is a space between the carbon outlet and the canister wall, the pressure gradient is mostly uniform in the axial direction and there is very little variation in radial pressure throughout the carbon bed. In contrast to this, in Fig. 5.6 it is clear that the pressure varies both in the radial and axial directions throughout the carbon bed, as the flow against the back wall is directed inwards towards the outlet. This also results in a significantly increased pressure drop in these cases.

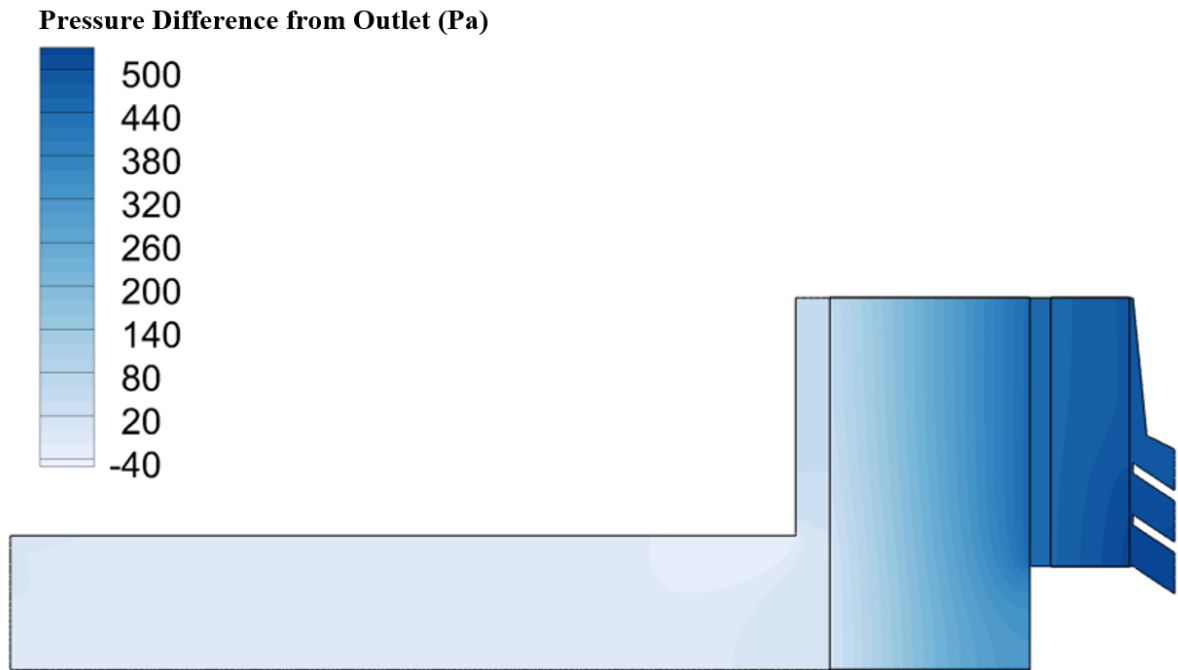


Figure 5.5: Distribution of pressure difference from the outlet in the case with curvature towards the outlet and extended spacing between the carbon bed and the canister rear wall (the case with the lowest pressure drop).

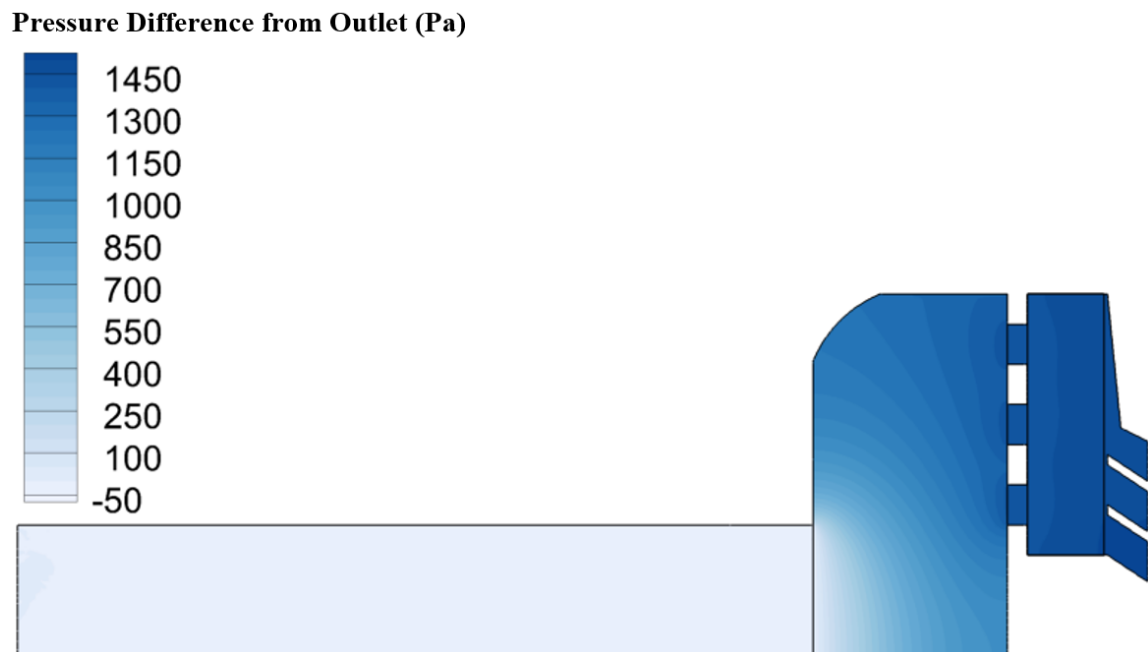


Figure 5.6: Distribution of pressure difference from the outlet in the case with the bracketing between the carbon and particulate filters and curvature of the outer wall (the case with the greatest pressure drop).

The air age distribution in the carbon bed was significantly affected by the porosity profile of the carbon bed. In all cases close to the canister wall, an area of much lower residence time could be

5.9 Results of the Steady State Analysis

seen in the area with the highest porosity, as this region offers weaker resistance to flow so air passes through more rapidly. The velocity close to the canister wall is indicative of the porosity profile, with alternating regions of high and low porosity as shown in Fig. 5.7, with higher velocities seen at radial distances where the porosity is low.

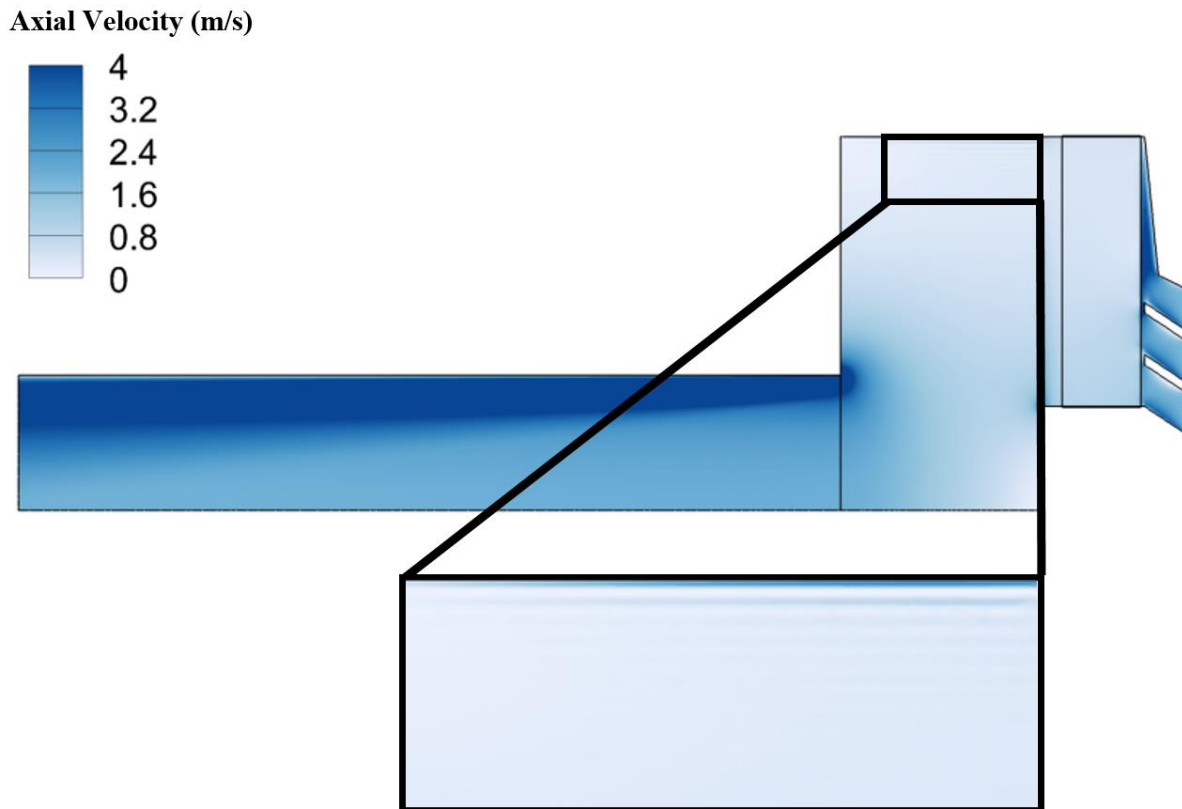


Figure 5.7: Alternating regions of high and low velocity close to the canister wall in the base geometry.

Similar to the mean pressure difference, the air age profile within the carbon bed depends significantly on whether or not the carbon bed backs directly onto the canister back wall. In cases where it does not, the air age increase is more uniform in the axial direction away from the canister wall as shown in Fig. 5.8. When the carbon bed backs directly onto the wall there is more flow in the radial direction, which creates the air age distribution shown in Fig. 5.9.

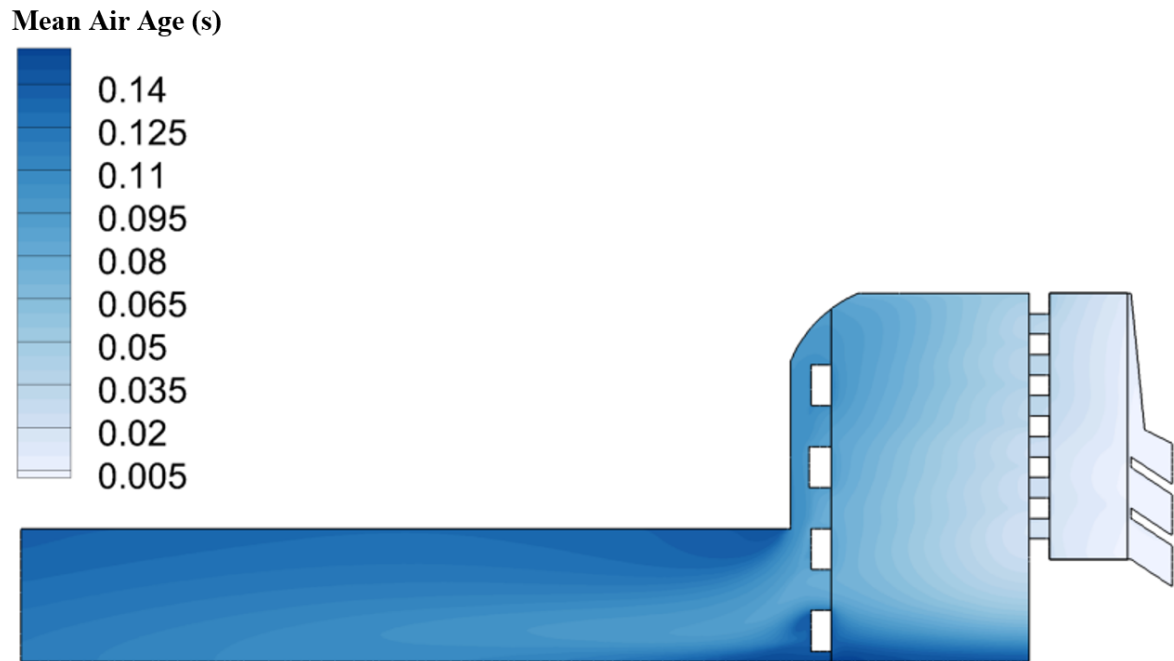


Figure 5.8: Mean age distribution throughout the canister in the case with a curved outer canister wall and bracketing between the carbon and particulate filter and bracketing between the carbon and the rear wall (the case with the smallest mean air age at the carbon outlet).



Figure 5.9: Mean air age distribution throughout the canister in the case with bracketing between the particulate filter and carbon bed (the case with the greatest mean air age at the carbon outlet).

5.9.2 Summary of Effects of Geometry Changes

The full effects of each parameter on each of the measured variables are described in more detail in the “Analysis of Variance” section. The following is a summary of the major trends.

Space between carbon bed and canister wall: Fig. 5.10 shows that the cases in which the carbon bed backs directly on to the wall have a far larger pressure drop than all other cases, typically by a

factor of three. This effect is somewhat diminished when the inner angle of the canister towards the outlet is also curved. The 2 mm rear spacing reduces the pressure drop by a factor of three in most cases, and the 6 mm rear spacing by a further 5-25%. Introducing bracketing into the rear gap slightly increases the pressure drop, typically in the range of 10-50 Pa compared to the 6 mm rear spacing, with the larger spaces between bracket holes generally causing a slightly larger pressure drop.

As Fig. 5.11 shows, the cases, where the carbon bed backs directly onto the canister wall, have a much larger mean residence time, ranging from 50% to 100% larger than all other cases. However, this does not provide a substantial benefit, as Fig. 5.12 shows that the minimum residence time is reduced by up to 50%.

Curving the canister wall: Curving the outside of the canister wall typically provided a small reduction (5% to 20%) in mean residence time (see Fig. 5.11), although this was possibly due to the reduction in carbon volume. It also provided a small increase (up to 20%) in the minimum mean residence time (see Fig. 5.12).

Curving the inside corner of the canister wall decreased the pressure drop and increased the mean and minimum residence times only in cases where the carbon bed backed directly onto the canister wall.

Bracketing between filter layers: Typically, both sizes of bracket caused a very small increase (20 Pa to 70 Pa) in pressure drop. This was larger for the finer bracket as demonstrated in Fig. 5.10.

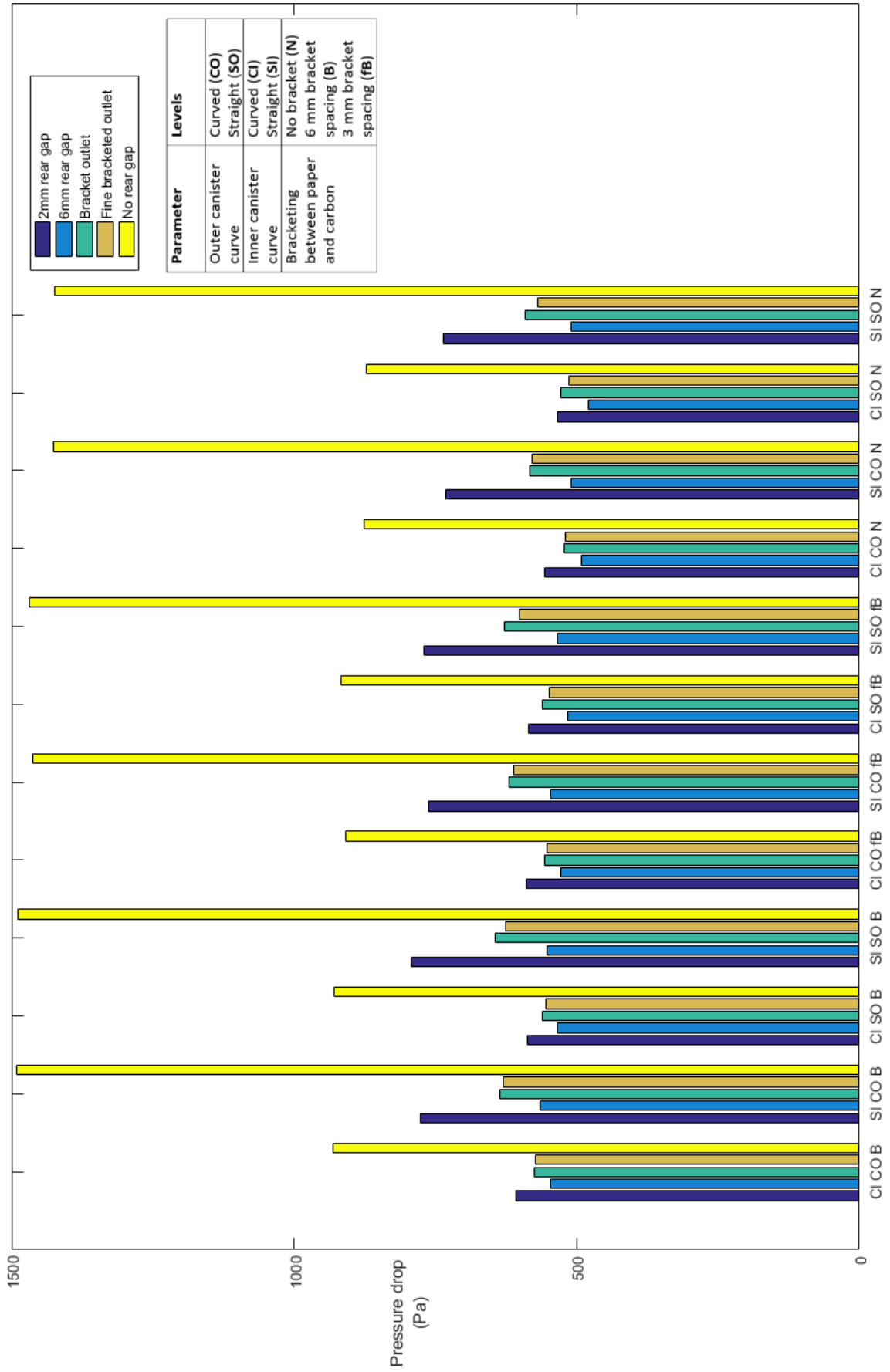


Figure 5.10: Pressure drop throughout the canister for all canister geometries.

5.9 Results of the Steady State Analysis

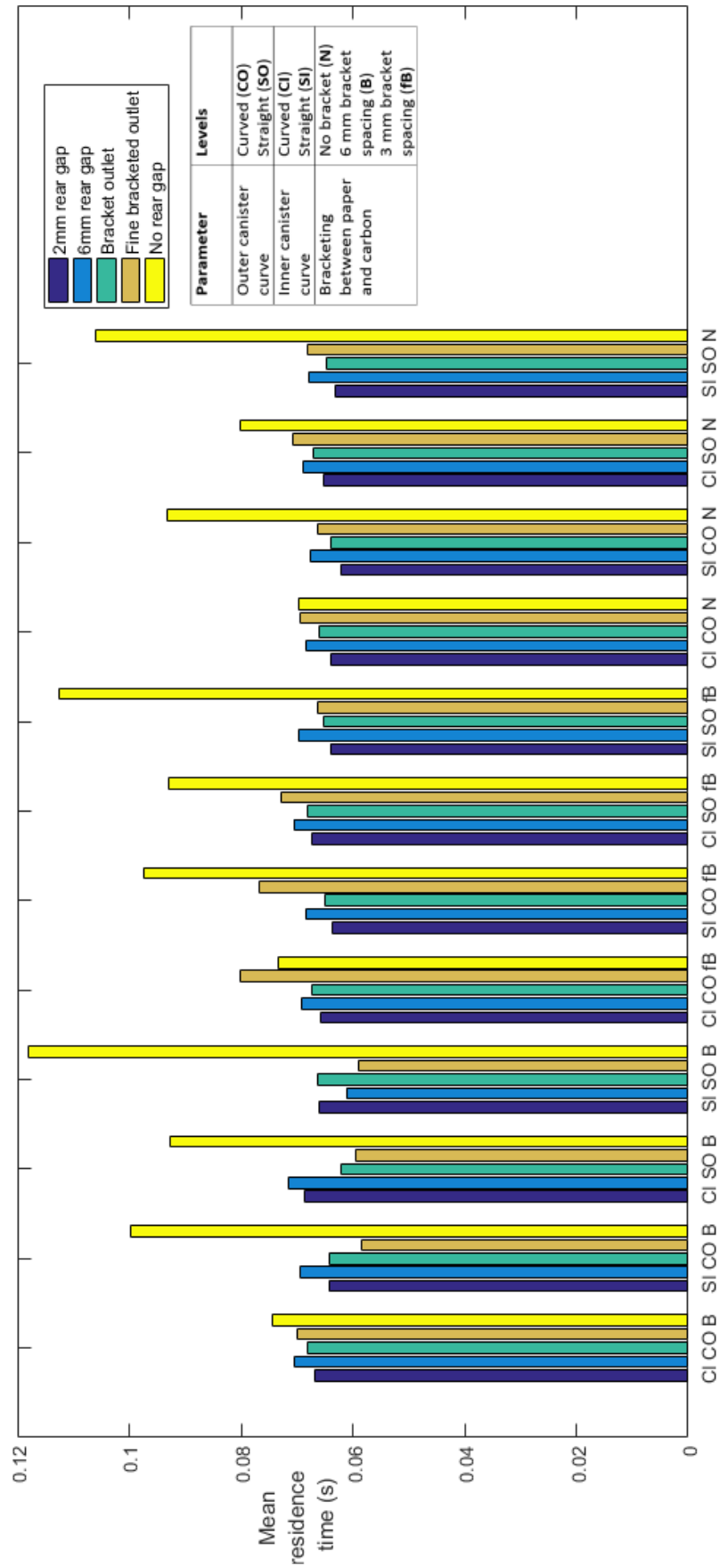


Figure 5.11: Mean residence time at the rear of the carbon bed for all canister geometries.

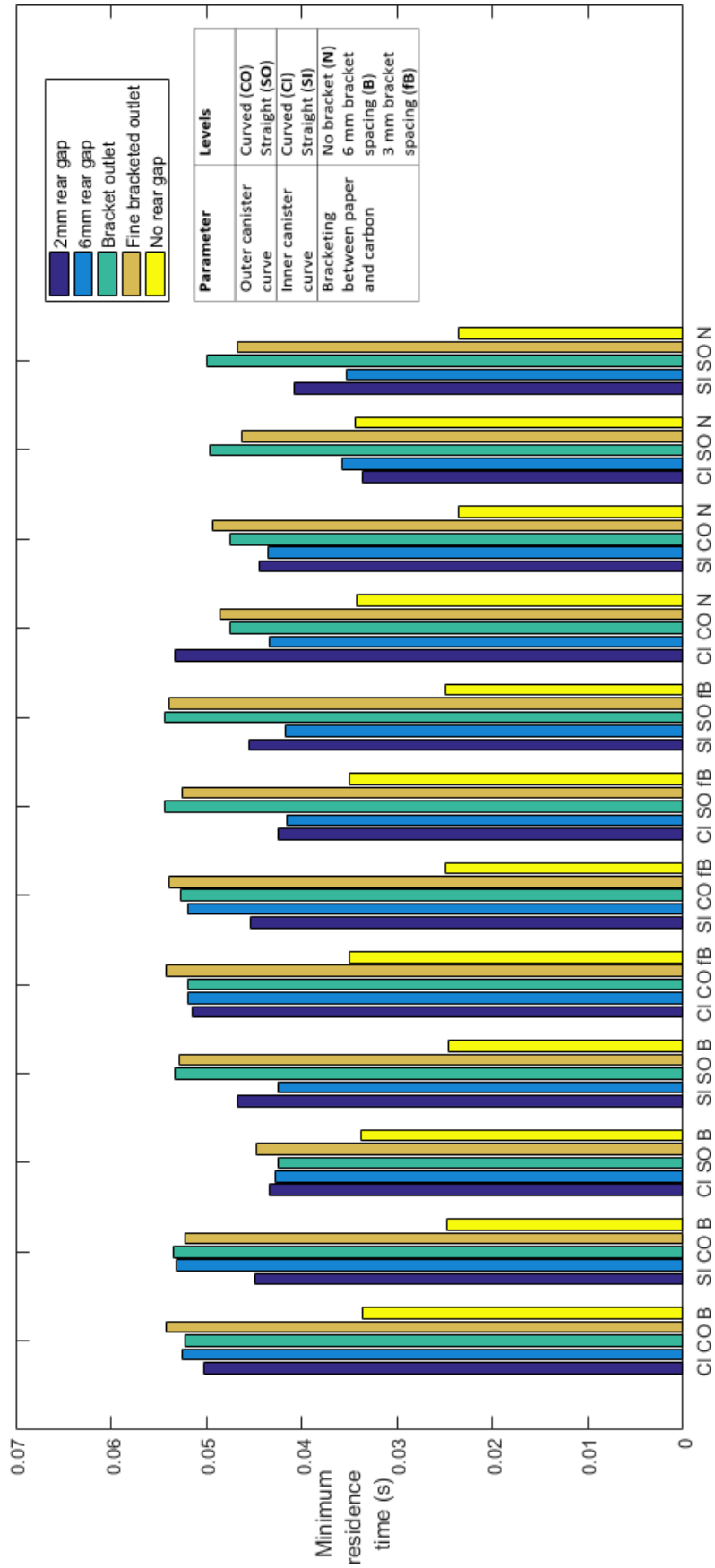


Figure 5.12: Minimum mean residence at the rear of the carbon bed for all canister geometries.

5.9.3 Analysis of Variance Results

Analysis of Variance (ANOVA) is a statistical technique which quantifies the significance of each parameter on the measured variable. In this case, it has been used to analyse the impact of altering each geometric parameter on the pressure drop, average mean air age at the rear of the carbon bed and the minimum mean air age at the rear of the carbon bed, over the whole range of cases investigated here. It also gives an indication of any two-factor interactions between geometric parameters. This allows a clearer assessment of which parameters are the most significant across the whole data-set.

The full ANOVA methodology is given in [111]. The key output of this method is the significance value, in which a significance of $P < 0.05$ is indicative that the change has a statistically significant impact across the whole range of data.

Pressure drop: The ANOVA results shown in Table 5.6 indicate that all factors have a significant impact on the mean pressure drop. By far the greatest factor influencing the mean pressure drop is the spacing at the rear of the carbon bed, as shown in Fig. 5.10. In cases, where the carbon bed backs directly onto the rear wall of the canister, the pressure drop is typically far higher than in cases that have a space between the carbon and the wall, typically by a factor of three. A modest decrease (of the order of 10%) in the mean pressure drop is seen increasing the length of this space from 2 mm to 6 mm, and an increase of approximately 10 Pa to 50 Pa in pressure drop was seen if that 6 mm gap featured either shape of bracketing.

There is a two-factor interaction between the shape of the inner canister curve and the gap at the rear of the carbon. Fig. 5.10 shows that this interaction is only significant in the cases which have no rear gap. The curve means that less of the carbon backs directly onto the carbon wall than the configuration where the back of the canister is straight. The impact of curving the outside edge of the canister on the mean pressure drop was found to be extremely small.

Bracketing between the particulate filter and carbon bed had some impact on the mean pressure drop. Applying a 6 mm spaced bracket increased the mean pressure drop by an average of

38 Pa over the un-bracketed cases. Applying a 3 mm spaced bracket increased the pressure drop by an average of 63 Pa over the un-bracketed cases.

Table 5.6: Results of the ANOVA analysis with respect to pressure drop.

Source	Significance
CI	0
CO	0.0055
Inlet bracket	0
Rear gap	0
CI*CO	0.004
CI*Inlet bracket	0.1668
CI* Rear gap	0
CO*Inlet bracket	0.2793
CO*Rear gap	0.0082
Inlet*Rear gap	0.3451
Error	

Mean air age at rear of carbon bed: The ANOVA results shown in Table 5.7 show that all factors have a significant impact on the mean residence time at the outlet of the carbon. As with pressure drop, by far the greatest factor influencing the mean air age at the carbon outlet is the spacing at the rear of the carbon. In cases where the carbon backs directly onto the rear wall of the canister the mean air age at the carbon outlet is typically 50% higher than in cases that have a space between the carbon and the wall, as can be seen from Fig. 5.11.

Curving the outer canister wall generally had a small reduction on the mean residence time, although this was likely to be largely due to the associated reduction in carbon volume, on average resulting in a mean residence time reduced approximately by 5%.

Bracketing between the particulate filter and carbon bed had a very small impact on the mean residence time at the carbon outlet. The 3 mm spaced bracket on average increased mean residence time by 2.5%, and the 6 mm bracket on average increased residence time by 5%.

There is a significant two-factor interaction between the shape of the inner canister curve and the gap at the rear of the carbon. The mean air age at the rear of the carbon bed significantly increases in cases where the carbon bed backs onto the canister wall when it is curved at the outlet. As less of the carbon backs directly onto the curved canister wall, the mean air age assumes values similar to those in cases where there is a space between the rear wall and the carbon bed.

5.9 Results of the Steady State Analysis

Table 5.7: Results of the ANOVA analysis with respect to the mean residence time in the carbon at the rear of the carbon bed.

Source	Significance
CI	0.0006
CO	0.001
Inlet bracket	0.0014
Rear gap	0
CI*CO	0.9292
CI*Inlet bracket	0.7031
CI* Rear gap	0
CO*Inlet bracket	0.7474
CO*Rear gap	0
Inlet*Rear gap	0
Error	

Mean Air Age (s)

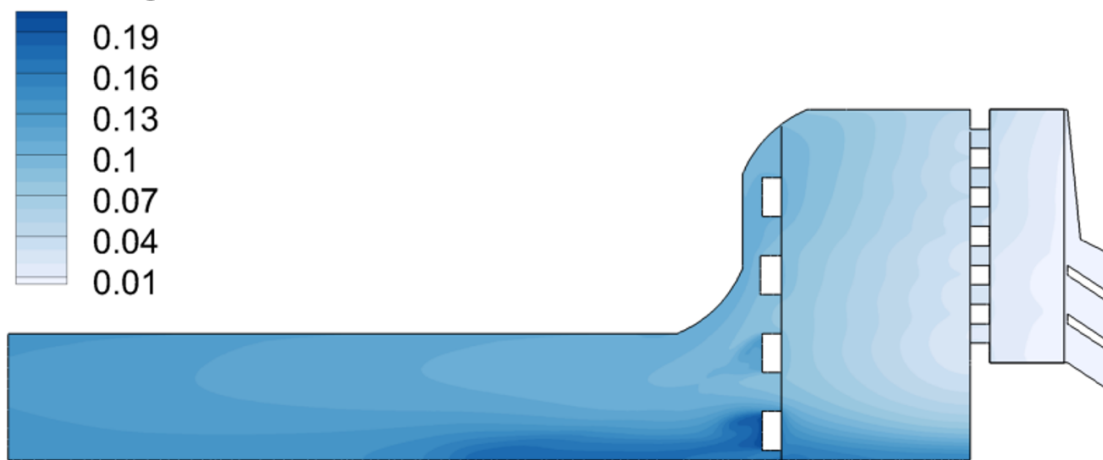


Figure 5:13. Distribution of mean air age throughout the canister in the case with the largest minimum residence time at the rear of the carbon bed.

Mean Air Age (s)



Figure 5:14. Distribution of mean air age throughout the canister in the case with the smallest minimum residence time at the rear of the carbon bed.

Minimum air age at rear of carbon bed: The most important factor affecting the minimum mean air age at the rear of the canister was the presence of a gap or bracket at the rear of the carbon, as shown in Fig. 5.12. Bracketing towards the outside of the canister had a significant effect in increasing the minimum residence time identified, typically by 10% to 50%. Because of the porosity profile towards the canister wall, there is an area of very low porosity approximately one particle diameter from the canister wall, where the minimum air age is likely to be found.

Curving the outer canister wall generally caused a modest increase of the minimum residence time, possibly due to the increased length of the canister wall, causing flow in the porous zone close to the wall to take a slightly longer path. On average, this increased the minimum mean residence time approximately by 10%.

Table 5.8: Results of the ANOVA analysis with respect to the minimum residence time in the carbon at the rear of the carbon bed.

Source	Significance
CI	0.037
CO	0
Inlet bracket	0
Rear gap	0
CI*CO	0.0134
CI*Inlet bracket	0.3846
CI*Rear gap	0
CO*Inlet bracket	0.5576
CO*Rear gap	0.0003
Inlet*Rear gap	0.124
Error	

5.10 Key Findings of the Steady State Analysis

Sixty steady-state axisymmetric CFD simulations have been carried out to assess the effects of small alterations to the geometry of a representative CBRN canister, with respect to the mean pressure drop and the mean residence time distribution throughout the canister. The cases in which the carbon filter backs directly onto the canister rear wall have a much larger pressure drop than all other cases, typically by a factor of three. This is due to the longer route through the porous medium the flow must typically take, as flow close to the cylinder wall will reach the rear wall and then have to flow inwards radially to reach the outlet. Increasing the distance travelled by the air through

5.10 Key Findings of the Steady State Analysis

the porous medium results in an increased pressure drop. This inward flow will also drive air entering the carbon bed closer to the canister axis more rapidly towards the outlet of the carbon bed, reducing the minimum air age observed. These cases exhibit the largest variation of mean air age, and rapid breakthrough of the filter is likely to occur for such a low minimum air age. This suggests that the mean air age alone at the carbon outlet is not a good indicator of filter performance. Moreover, the simulations show the carbon filter backing directly onto the canister rear wall is highly detrimental to the overall performance.

Bracketing in the space between the carbon and the canister rear wall has a large impact on the minimum residence time, significantly reducing it in nearly all cases. Both bracketing types have a similar impact; the most important requirement is that the region of highest porosity close to the wall is adequately blocked by the bracket. The bracketing used in axisymmetric simulations cannot be entirely representative of real 3D brackets. There is a possibility that in three dimensions some brackets may cause behaviour similar to that seen in cases where the carbon backs directly onto the wall, causing flow in the radial direction, which may be detrimental to performance.

Changing the curvature at the outer wall may help to direct the flow through the most porous region to take a longer path and improve the minimum value of mean air age at the outlet, with a very small impact on the average value of mean air age and mean pressure drop.

Although it is impossible for axisymmetric simulations to capture all of the features of a full 3D canister geometry, certain flow features such as the alternating regions of high and low porosity close to the wall (and the ensuing velocity) should remain consistent between two and three dimensions. Axisymmetric CFD modelling of adsorption through a simplified canister geometry has previously given a good match to experimental results [106]. The results of an axisymmetric study can therefore be used as a basis from which to inform some aspects of 3D canister design.

It is worth noting the present analysis focuses on steady-state simulations for a given flow rate but the qualitative nature of the present findings remains unaltered for steady flow rates within from 10 l min^{-1} to 150 l min^{-1} . However, in breath responsive PAPRs flow through the filters

remains unsteady and the filter performance for transient flow is yet to be analysed. This forms the basis for the following sections.

5.11 Geometries for Transient Analysis

The steady-state simulations highlighted the importance of the spacing between the carbon and the rear canister wall, and of the impact of the non-uniform porosity profile close to the canister wall. In most practical respirator applications, the inlet velocity is not in a steady state but will instead rise and fall according to the user's breathing rate. In order to supplement the previous work, three key canister geometries were selected to be representative of the effects of the major changes and these geometries were chosen for transient simulations. The geometries selected are shown in Fig. 5.15.

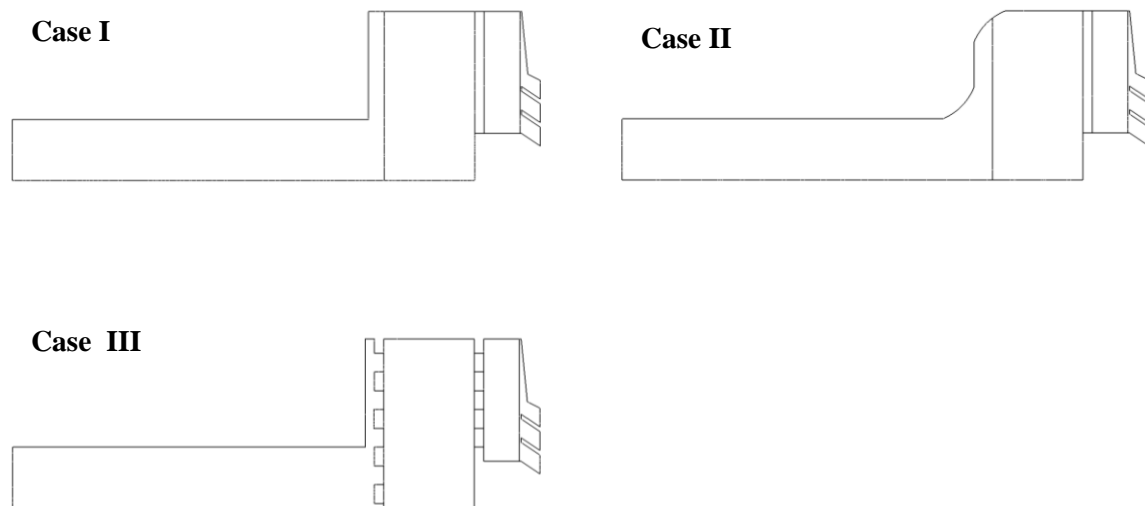


Figure 5.15: Canister geometries chosen for the transient simulations.

5.12 Transient Boundary Conditions

The inlet velocity profile was selected as a positive sine wave that would give a flowrate of 50 L/min with a period of 2 seconds. The times in which the flowrate was negative (i.e. when the user is exhaling) were ignored. The simulations were run over 1 second so were representative of a single breath. All other boundary conditions were the same as seen for the steady-state simulations as seen in Section 5.6.

5.13 Time-step Selection

The time-step was selected by means of a sensitivity analysis on case II. The mean air age at the rear of the carbon and the pressure drop across the whole canister were compared at each time step and verified to be within 1% of one another. Results using 300 time steps and 600 were shown to be in good agreement so 300 time steps were used for all cases.

5.14 Transient Results

For each of the cases, the mean air age of air leaving the carbon bed was investigated with respect to distance from the canister wall as the inlet velocity decreased from a peak at 0.5 s to zero, as shown in Figs. 5.16, 5.17 and 5.18 in 0.1 s increments. As the mean air age was smaller overall for higher velocities the results were normalised in order to better compare the profile at differing inlet velocities.

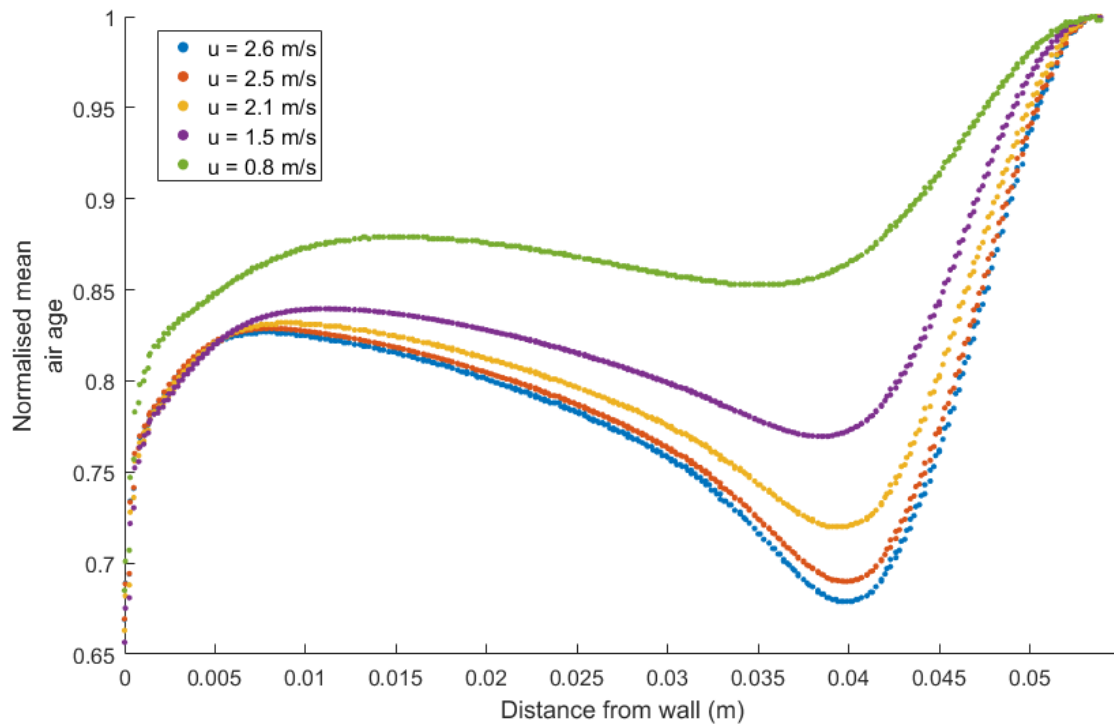


Figure 5.16: Normalised mean air age at the rear of the carbon bed with respect to distance from the canister outer wall for case I.

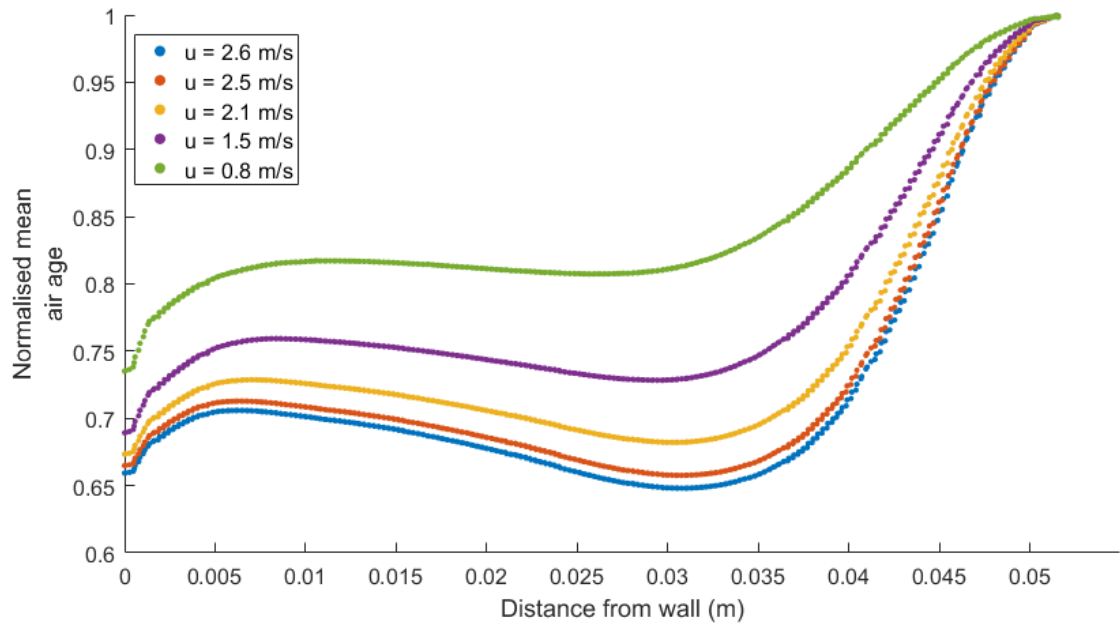


Figure 5.17: Normalised mean air age at the rear of the carbon bed with respect to distance from the canister outer wall for case II.

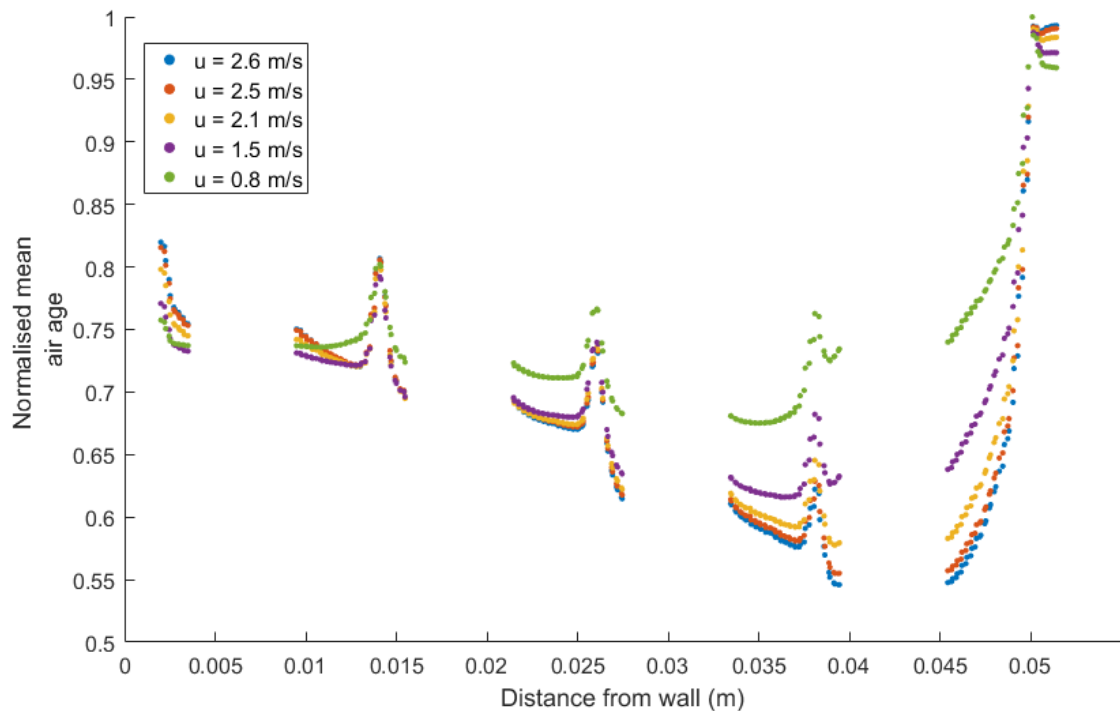


Figure 5.18: Normalised mean air age at the rear of the carbon bed with respect to distance from the canister outer wall for case III.

In all cases the very centre of the canister showed the highest value of mean air age as expected, as it provides the longest route from the inlet of the carbon bed to the outlet is situated in a region with

5.15 Key Findings of the Transient Analysis

potential for stagnation. This aspect of the residence time distribution is consistent whether at steady-state or under transient conditions.

Cases I and II broadly show a similar profile over time for mean air age distribution. In both cases, the impact of the region of high voidage close to the canister wall is apparent, with a clear region of low mean air age approximately one particle diameter away from the canister wall. This effect is mildly reduced by the curvature of the wall in case II. The effect is more significant at low inlet velocities. At higher inlet velocities in both cases I and II a transition is seen at the location of minimum mean air age from close to the canister wall to the region 30-40 mm from the canister wall. This corresponds to approximately the region in the shortest path from the canister inlet to the outlet. It is likely that this becomes more significant at higher velocities as there is less potential for flow to deviate from its path or recirculation with faster flows.

Case III shows a significantly different profile, as the bracketing close to the wall blocks off the region of low voidage. Consequently, the shape of the residence time distribution at the rear of the carbon bed did not significantly change with changing inlet velocity.

5.15 Key Findings of the Transient Analysis

The non-uniform voidage distribution described by the Mueller equation has been shown to result in regions of alternating high and low velocity close to the canister wall, leaving certain canister geometries in which this route is not closed by the canister or bracketing shape susceptible to a rapid breakthrough in this region. Transient simulations suggest that the distribution of mean air age throughout the canister is dependent upon the inlet velocity. In geometries where the low-voidage region close to the canister wall is left unobstructed, this route will typically have the lowest mean air age at low-flow rates. As the flow rate increases the region of low air-age will move into line with the shortest path directly from the canister inlet to the outlet. This suggests that the shape and positioning of the inlet may potentially be manipulated in order to control the residence time distribution at peak air-flow.

There is potential to optimise canister design and extend filter life by accounting for the expected flow-rate profile throughout the canister lifetime in order to make best possible use of the available filter material. Designs should be considered which exploit the difference in flow profile between high and low flow to ensure that adsorption sites are evenly used throughout the carbon bed. The expected usage of the canister can also be factored into this, as the flow profile will differ depending on the expected breathing rate of the user, which will vary under differing levels of labour.

The radial voidage profile has been shown to have a large impact on canister performance. In reality, there is likely to be a similar effect in the axial direction which has not been modelled here. Further investigation should be carried out to see if this significantly affects the overall flow field, as there is likely to be some regions of high voidage close to the outlet of the carbon bed in designs which feature bracketing at the rear of the carbon.

Mean air age distribution provides only a limited indication of canister performance, as adsorption is a complex kinetic process that depends on not only residence time but also on the number of available adsorption sites and the local contaminant concentration throughout the carbon bed. As such, these methods of canister optimisation should be used only as an early indicator in the design process.

Chapter 6

Transient Flow through a Generic CBRN Canister

In this chapter, a more detailed 3D model of a generic CBRN canister has been developed and used for unsteady RANS simulations in order to assess the performance of the canister under transient flow in a realistic breathing profile. The performance has been assessed with respect to pressure drop across the canister and residence time distribution within the carbon filter. Three representative breathing rates (for adult males under light, moderate and heavy workloads) have been analysed and compared to the equivalent steady state flow rates. The intent behind this work was to identify which trends persist between steady state and transient operating conditions.

6.1 Background

CFD has been used in the past to demonstrate that there is considerable scope to optimise both the pressure drop and service life of a CBRN canister by modifying the bracket geometry [46, 105]. These studies consider steady continuous flow throughout the canister. However, in most applications the flow through a CBRN canister is unlikely to be continuous but will instead follow a human breathing pattern, which somewhat resembles a half- sinusoidal curve (i.e. the positive component of a sinusoidal curve describes inhaled air entering the filter, which is then followed by a period of no flow as exhaled air does not pass through the filter but leaves via a valve in the mask). This means that compared to an equivalent continuous flow rate a real breathing pattern will show a much higher flow rate, which may affect the distribution of air throughout the canister. This effect has been observed in simple axisymmetric simulations in Chapter 5.

A previous study measured the breathing rates of healthy adult males and found that under light exercise a typical breathing rate of 30 L/min was expected. At this breathing rate, on average a peak airflow of 126 L/min was found [37].

The difference in inlet flow profiles may have significant ramifications on filter performance. The pressure drop across the filter is described by the Forchheimer equation, as described in Chapter 5 (Eq. 5.1). At lower flow rates, the viscous term dominates and the inertial term may often be

neglected [46]. A constant low breathing rate may therefore consistently neglect the inertial term. A real sinusoidal breathing profile, which provides the same total air supply as the constant rate, may however frequently temporarily rise to flow rates where the inertial term becomes significant and hence continuous air supply and real breathing profiles are not necessarily comparable.

An experimental study of non-CBRN respirator cartridges (which still featured a similar layer of activated carbon adsorbent) used a breathing machine to measure the breakthrough time of CCl_4 (chosen as a representative substance for volatile organic compounds, a common respiratory hazard) under steady flow rate and the equivalent average-breathing rate with a real breathing pattern. It was found that the breakthrough time reduces under real breathing patterns as compared to steady-state, and this effect becomes increasingly prominent for high mean flow rates [36].

Failure occurs in a canister when there exists a route through the adsorbent bed in which air passes through with insufficient time for the full adsorption of the challenge substance. Although it is not possible to predict the exact time to failure without fully modelling adsorption (which is computationally expensive and specific to the chemistry of the particular challenge substance), the existence of a route through the filter that will not allow sufficient adsorption can be predicted by use of the mean air age equation [105], which is further discussed in Chapter 3 (Eq. 3.1).

The best case for filter life occurs when flow throughout the filter is distributed in such a way that all routes through the filter fail simultaneously, ensuring that all available adsorbent has been used. This can be estimated by the mean air age at the rear of the canister. The objective of this study is to use CFD to investigate the impact of transient breathing patterns on the flow throughout a CBRN canister in order to optimise future canister design. In addition, the significance of the non-uniform porosity profile identified in packed beds is also investigated in the context of transient CBRN canister performance.

6.2 Mathematical background and Numerical implementation

The commercial CFD software Ansys Fluent [19] was used to solve the coupled mass and momentum conservation equations via the finite volume technique. All simulations were run to a

scaled residual convergence criteria of 10^{-4} for all variables. The full governing equations and numerical method used are given in detail in Chapter 2.

6.3 Turbulence Modelling

In a previous studies [105] a low Reynolds Number $k - \epsilon$ model which solves modelled transport equations of k and ϵ up to the wall was used, but this needs very small grid spacing adjacent to the wall. For a transient case using a sinusoidal breathing profile the velocities seen at the point of peak inhalation can be much larger than that obtained for the steady-state analysis for the corresponding average flow rate. Thus, the grid spacing that is sufficient for the low Reynolds number $k - \epsilon$ model in the context of steady-state analysis with the same average flow rate may not be sufficient for the whole duration of the breathing cycle. Thus, an alternative approach with a blended wall treatment was instead considered, which is less demanding than the low Reynolds number $k - \epsilon$ model in terms of wall adjacent grid spacing. For this purpose, the $k - \epsilon$ model with blended wall treatment has been used for transient simulations.

6.4 Geometry and Boundary Conditions

All simulations were considered for an industrial CBRN canister, which has been extensively studied in the past [46, 105], shown in Fig. 6.1. The geometry consists of four distinct chambers separated by bracketing. Air from the inlet enters a hollow inlet chamber, a chamber packed with particulate filtering medium, the activated carbon bed and a hollow outlet chamber. The canister was modelled as one eighth of the total geometry by exploiting the symmetry of the domain. The domain at the actual outlet location was extended in order to avoid any possible recirculation on the outlet plane (which can potentially affect the simulation predictions at the region of interest). In spite of this extension, the pressure drop is evaluated based on the values at the inlet and the exact outlet (instead of the outlet of the computational domain) locations. The precise nature of the downstream geometry is not expected to significantly affect the flow field within the filter.

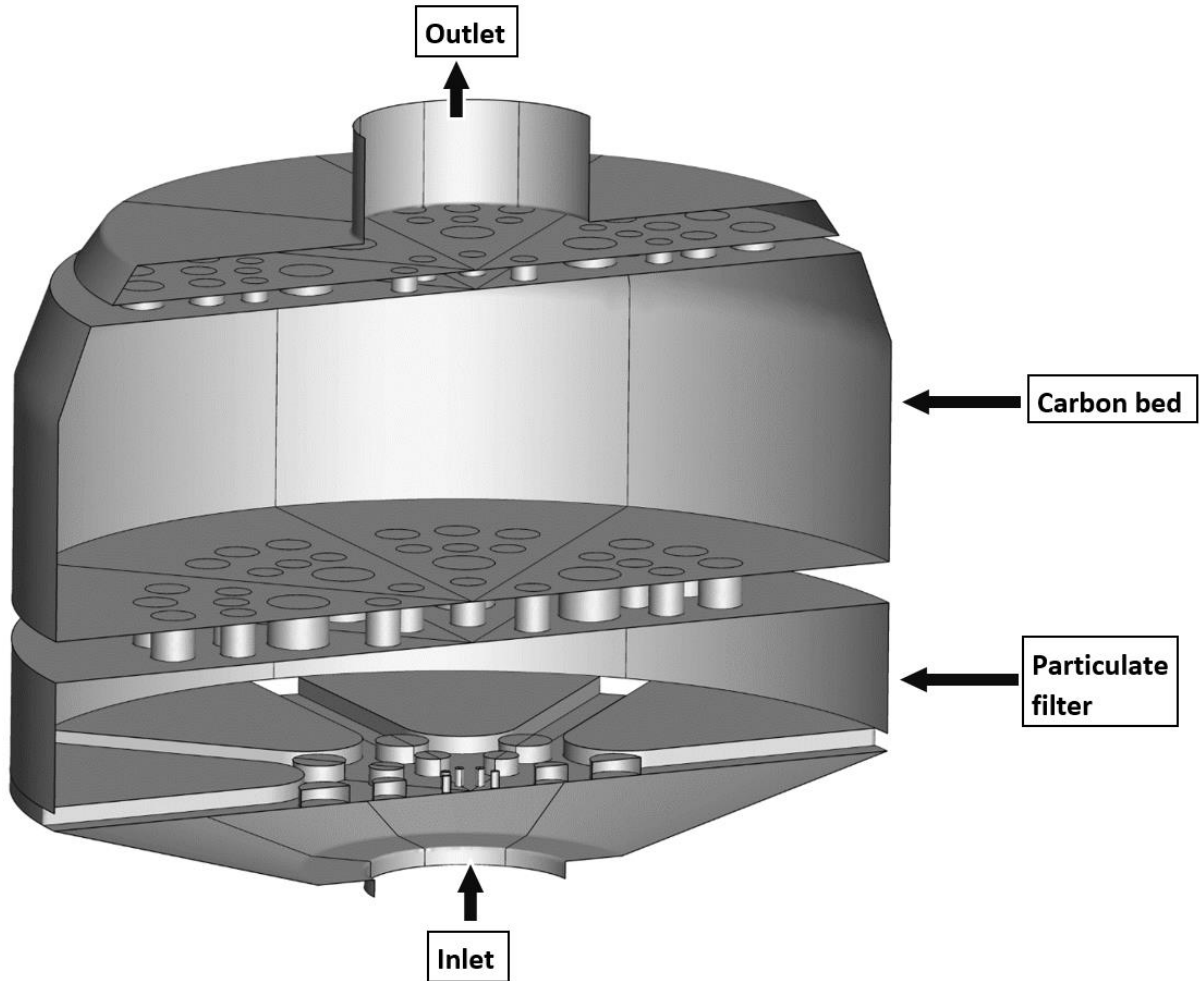


Figure 6.1: Geometry of the configuration considered for all simulations.

At the inlet the velocity is specified according to the flow rate. The turbulent boundary conditions are specified by means of a sensitivity analysis in terms of turbulence intensity I and turbulence length scale l_t which are taken to be:

$$I = \frac{\sqrt{\frac{2k}{3}}}{U} = 10\% \quad \text{and} \quad l_t = 0.07d \quad (6.1)$$

where d is the diameter of the canister inlet and $U = 4Q/\pi d^2$ is the mean velocity at the canister inlet where Q is the volume flow rate. It has been found that the results are insensitive to the choices of I and l_t as inlet turbulence was rapidly damped by the porous medium. All walls are taken to be no-slip and impenetrable. Turbulent kinetic energy was taken as zero at the walls. For the cases, which used the low-Reynolds number turbulence model, the turbulence dissipation rate at the wall is specified to be:

$$\epsilon_{wall} = 2\nu(\partial\sqrt{k}/\partial n)^2 \quad (6.2)$$

where ν is the kinematic viscosity and n is the wall-normal distance. The outlet obeyed the Neumann boundary condition such that there was no variation of the primitive variables normal to the outlet. The domain was reduced in size by exploiting the symmetry of the canister and there was no gradient of each variable in the normal direction at the planes of symmetry.

6.5 Grid independence

Three unstructured Cartesian meshes were generated for the purpose of grid independence analysis. Steady-state simulations at $Re_{inlet} = 1000$ and $Re_{inlet} = 8000$ have been carried out for each mesh to assess grid independence across the range of inlet velocities expected. These values were selected as the limits, which could be validated against the experimental data reported in [105]. The mesh sizes and the mean pressure drop across the canister for these meshes have been reported in Table 6.1.

It can be seen from Table 1 that the pressure drop does not change appreciably for meshes B and C for $Re_{inlet} = 1000$ and $Re_{inlet} = 8000$ and on the basis of this analysis mesh B was chosen for all subsequent cases.

6.6 Turbulence model and Porosity Sensitivity

A sensitivity analysis of the impact of the turbulence model used on the results has been conducted by considering steady-state flow through the canister at $Re_{inlet} = 1000$. Since the regions of high and low porosity near the wall may fall into the viscous sublayer at lower flow rates, the analysis was carried out using both a constant porosity and the porosity profile given by the Mueller equation. The resistances for the particulate filter layer were taken as:

$$(-\Delta\bar{p}/L) = 1.52 \times 10^9 \bar{u}_s + 6.41 \times 10^3 \bar{u}_s^2 \quad (6.3)$$

The mean pressure drop across the whole length of the canister is compared for each of these cases as shown in Table 6.2.

Table 6.1: Information related to the meshes used for grid independence study.

<i>Mesh Parameters</i>			
Mesh	Mesh size (number of cells)	Mean pressure drop at $Re_{inlet} = 1000$	Mean pressure drop at $Re_{inlet} = 8000$
Mesh A	562000	108.0	1199.4
Mesh B	742000	111.6	1245.3
Mesh C	1150000	111.6	1245.4

Table 6.2: Mean pressure drops across the canister for the different porosity treatments and turbulence models.

<i>Turbulence Model and Permeability</i>			
Case	Carbon Porosity	Turbulence model	Pressure Drop (Pa)
A	Constant	Low Reynolds	111.6
B	Constant	Blended Wall Treatment	111.6
C	Mueller	Low Reynolds	108.8
D	Mueller	Blended Wall Treatment	108.5

The impact of the turbulence model and porosity model on the flow distribution is exemplarily shown by the mean air age profile at a cross-section 1 mm away from the outlet of the carbon bed in Fig. 6.2. It is clear from Table 6.2 and Fig. 6.2 that the modelling the alternating regions of high and low porosity close to the canister wall according to the Mueller equation may have a significant impact on the resultant flow profile, with a lower mean air age seen close to the wall (corresponding with the area of high porosity).

Both the pressure drop from Table 6.1 and the mean air age profile from Fig. 6.2 indicate that the results are not overly sensitive to the choice of turbulence model. On the basis of this analysis, the blended wall treatment was preferred for two reasons. Firstly, a very large reduction in computational time was seen with the blended wall treatment as compared to the fully wall-resolved approach needed for the low Reynolds number $k - \epsilon$ model. Secondly, although it was always desired to keep the $y^+ = u_\tau y / \nu$ (where $u_\tau = \sqrt{\tau_w / \rho}$ is the friction velocity with τ_w being the wall shear stress) of the first layer of cells adjacent to the wall inside the viscous sublayer ($y^+ < 5$) for the low Reynolds number $k - \epsilon$ model, this could not necessarily be guaranteed for the high

6.7 Model Validation

fluid velocities seen in some parts of the canister at peak flow rates in the transient analysis. However, the blended wall-treatment has previously been shown to be less sensitive to y^+ values and can still give good results if $y^+ > 5$ is obtained for some wall adjacent cells [112].

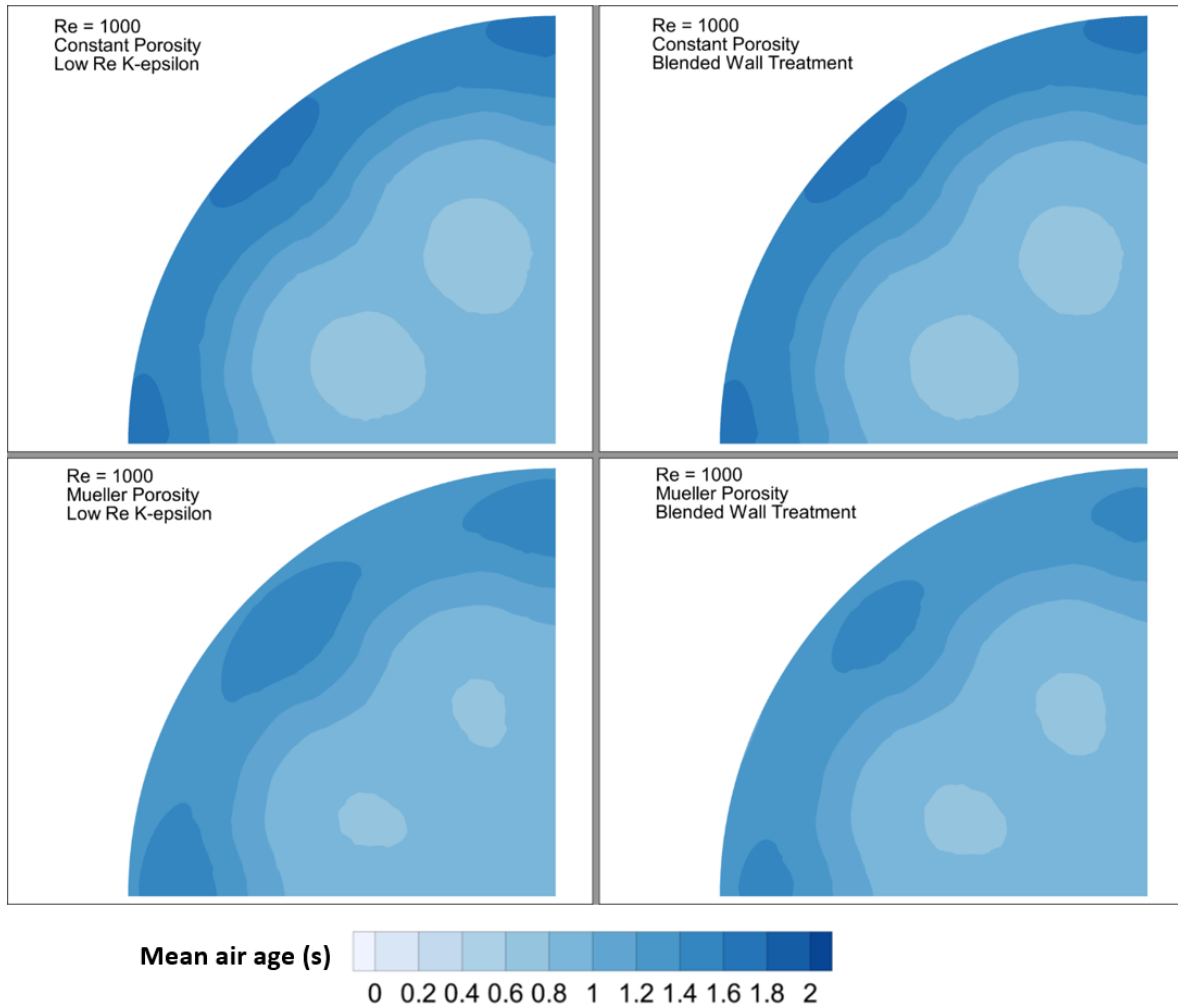


Figure 6.2: Mean air age distributions under steady flow at a cross-section 1mm from the outlet of the carbon bed for the two different turbulence models and descriptions of carbon porosity.

6.7 Model Validation

Validation for the numerical method used here has been conducted by carrying out steady-state simulations at eight different flow rates using both constant porosity and that described by the Mueller equation and measuring the mean pressure difference across the canister, in order to compare against the experimental data found in [105], as shown in Fig 6.3. The experimental data is taken from [105] over a wide range of data points and it was utilised to determine the parameters

(i.e. a_1 and a_2) of the Forchheimer equation (i.e. Eq. 5.1). This gives a very accurate continuous depiction of the pressure drops over the complete range. In both cases, a good agreement was found between the experimental and simulated results, with the porosity profile described by the Mueller equation providing a slightly closer agreement with experimental data than the constant porosity assumption.

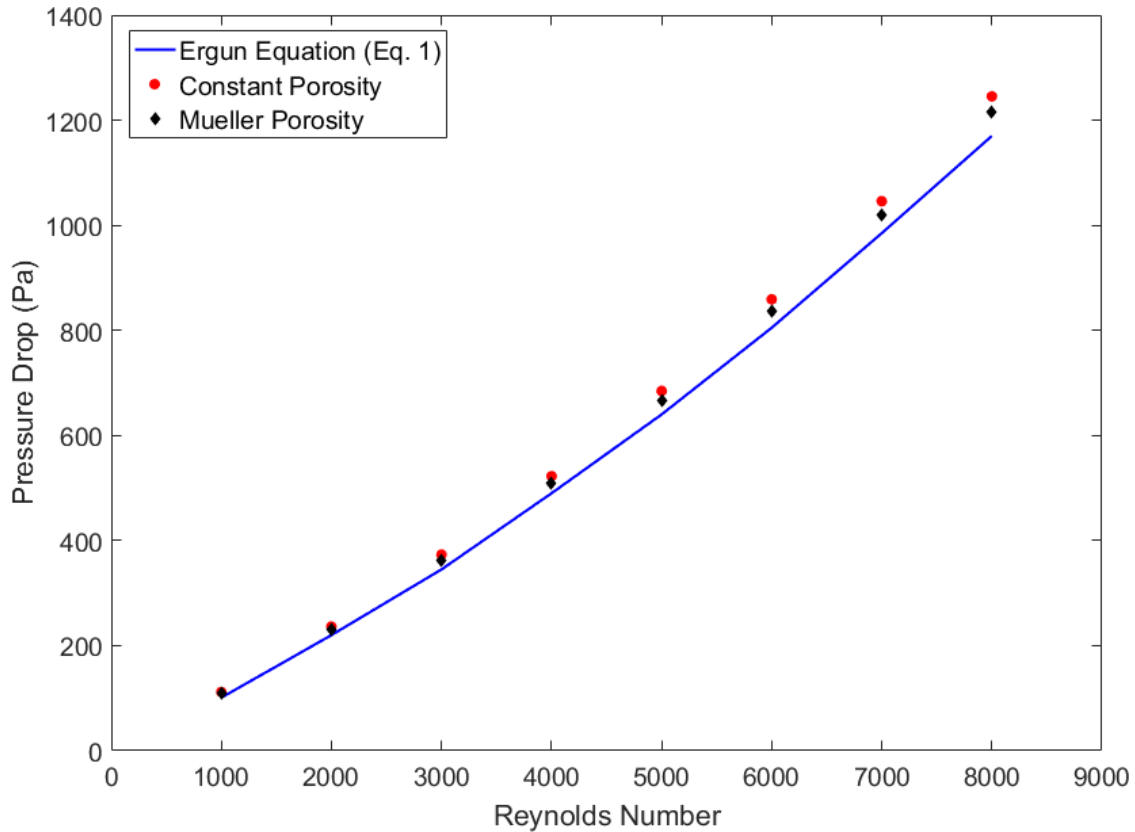


Figure 6.3: Pressure drop across the canister from CFD simulation for steady-state flow using both a constant porosity profile and the Mueller porosity profile compared with the predictions of viscous and inertial losses fit to experimental data.

6.8 Transient Breathing Profiles

Three breathing rates were chosen based on the measurements in [37], to represent breathing rates under light, moderate and heavy work for adult males, as listed in Table 6.3.

These breathing rates were each fitted to a sinusoidal profile of the following form:

$$Q = Q_{peak} \sin\left(\frac{2\pi t}{f}\right) \quad (6.4)$$

where Q is the volumetric flow rate and f is the breathing frequency [113]. Note that only the positive component of the breathing curve (the inhalation) was considered in the simulation, since only the inhalation passes through the filter, as shown in Fig. 6.4. In each simulation, the canister was held without flow for a period of time equal to the exhalation phase in order to calculate a more realistic mean air age. Three steady-state simulations were then carried out at the equivalent fixed flow rates. All cases for this analysis used the porosity profile described by the Mueller equation for the carbon bed.

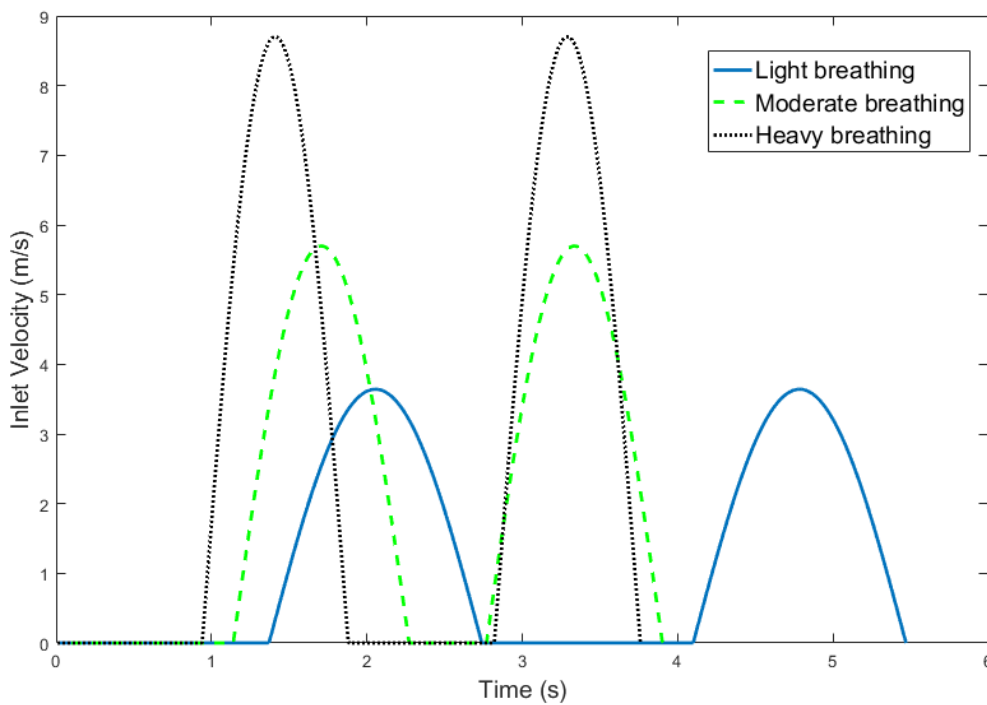


Figure 6.4: Representative breathing profiles used for each of the cases (showing 2 breaths).

6.9 Results & Discussion

6.9.1 Mean pressure drop

The mean pressure drop across the canister for each of the three breathing profiles throughout the complete breathing cycle was compared against the mean pressure drop for the equivalent steady-state flow rate, as shown in Fig. 6.5.

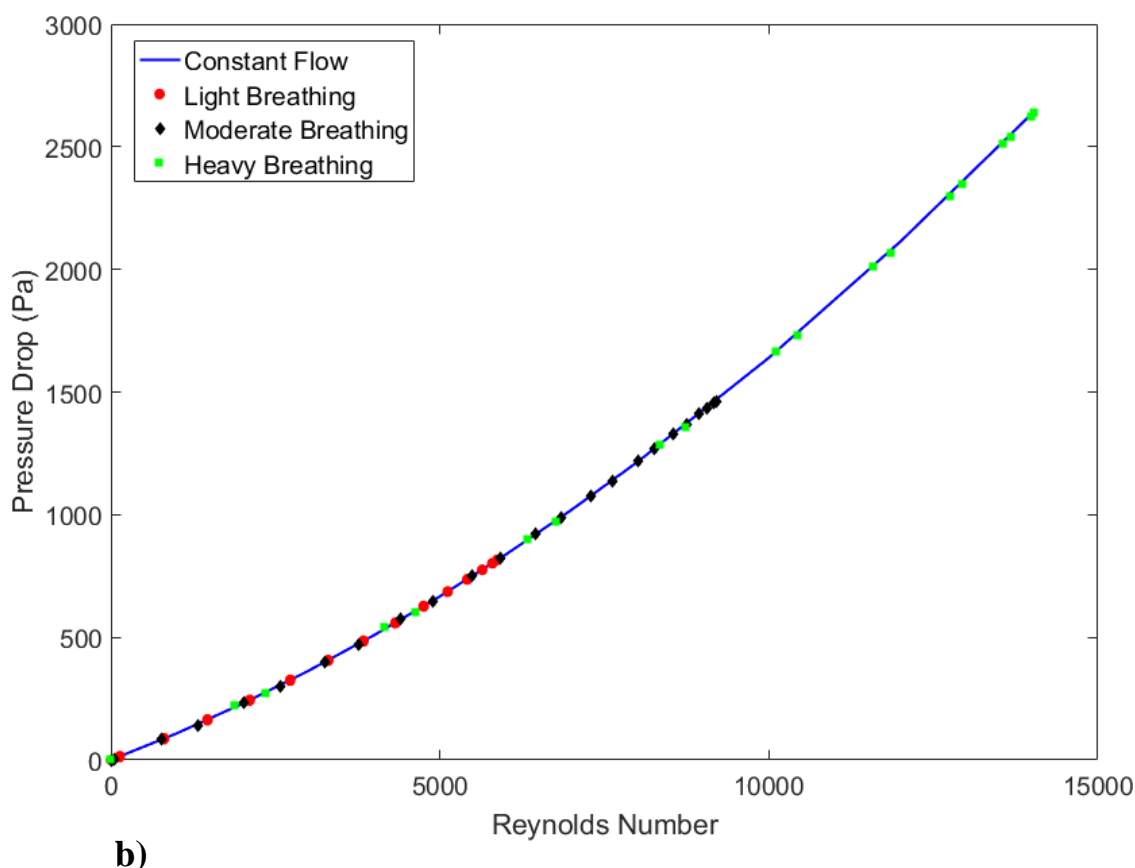


Figure 6.5: Pressure drop across the canister from CFD simulations at a range of flow rates covering all three complete breathing cycles.

From Fig. 6.5, it is clear that under transient conditions the pressure drop across the canister is very well predicted from the steady-state pressure drop for the corresponding mean inlet velocity. Since the peak inlet velocity for each transient case is far higher than for the equivalent continuous breathing rate, a comparison has been made between the maximum pressure drop seen for each breathing profile and the pressure drop that would be seen under continuous flow, and this comparison is shown in Table 6.3.

Table 6.3: The pressure drops seen across the canister under equivalent steady-state flows and the peak pressure drop for each transient case.

Breathing pattern	Mean flow rate (L/min)	Breath frequency (min^{-1})	Continuous flow pressure drop (Pa)	Peak flow pressure drop (Pa)
Light breathing	30.3	21.9	215.4	816.9
Moderate breathing	47.4	26.5	357.5	1464.5
Heavy breathing	72.3	31.9	586.2	2643.5

It is evident from Table 6.3 that assessing the pressure drop of a canister using the mean breathing rate will not give a good indicator of canister pressure drop, whereas continuous flow at the maximum flow rate of a given breathing pattern will effectively predict the maximum pressure drop (see Fig 6.5). The maximum pressure drop seen for a breathing pattern is a more useful metric than that for the equivalent mean breathing rate, as if the breathing resistance at any point in the cycle becomes excessive breathing will become difficult [37].

6.9.2 Residence Time Distribution

An estimate of the time available for adsorption within the filter can be made by analysing the mean air age and its distribution. A cross-section of the canister was considered 1 mm below the outlet of the carbon bed for all cases.

It is desirable to know the extent to which the residence time distribution may be related to the flow rate. A qualitative comparison of the mean air age close to the carbon filter outlet at two different flow rates for each of the breathing profiles is compared.

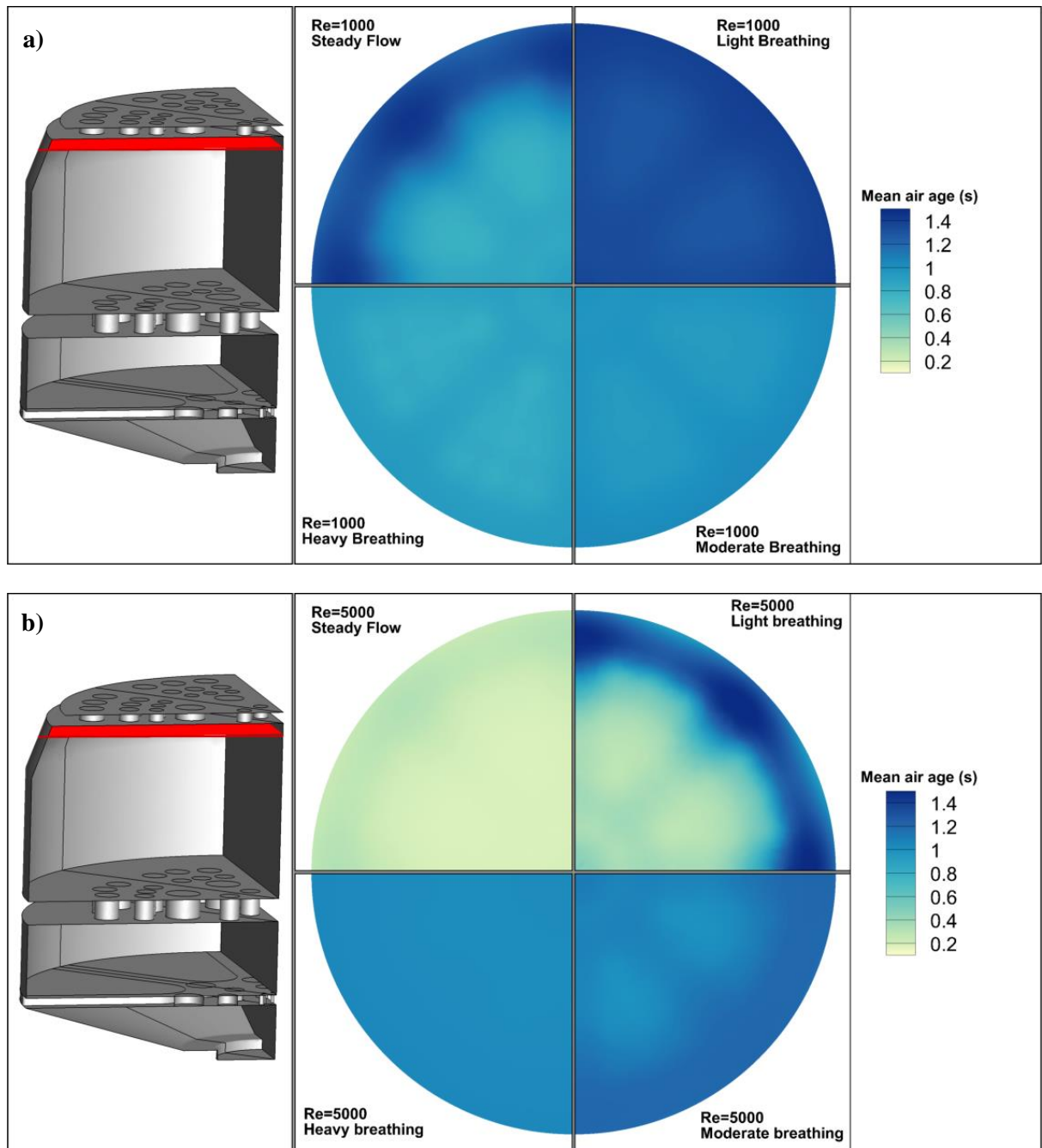


Figure 6.6: The residence time distribution at the carbon outlet at the same flow rate for each case and the equivalent steady-state flow at two different flow rates.

The mean air age distributions for different breathing rates have been compared to the corresponding continuous steady flow distribution in Fig. 6.6 for $Re = 1000$ and 5000 . It is clear from Fig. 6.6 that there is little in common in the profile seen for identical flow rates. The performance of the canister under continuous flow will therefore not be representative of the performance of an equivalent flow rate under transient conditions. The residence time distribution of the same cross-section is considered in Fig. 6.7 by taking the average residence time at each

radial distance throughout the canister over various points of progress through the breathing cycle. Each of the transient profiles is compared to the profiles at the equivalent steady-state flow rate over the whole cycle. It can be clearly seen that a somewhat similar residence time profile exists for all the steady-state cases, revealing the same areas of high and low mean air age, although the magnitude of residence time varies from case to case, with heavier breathing resulting in lower residence time. All steady-state cases indicate an area of high mean air age which peaks at approximately 88% of the canister radius, corresponding to a large dead zone.

A comparison of Fig. 6.7 ai, bi and ci shows that a roughly similar mean air age profile will be seen for comparable progress through the inhalation cycle. An initial period can be seen at 10% through inhalation in which the mean air age is very evenly distributed. This corresponds to the period where the air age distribution is primarily governed by the air that has been left stagnant from the previous cycle. Subsequently, a period is seen at 30% inhalation in which the mean air age towards the canister centre reduces, but the dead zone seen in the steady-state simulations is prominent. At 50% inhalation, the mean air age is considerably lower than that predicted under continuous flow. The dead zone seen under continuous flow is still visible at this stage, but is diminished compared to the steady-state case. A similar comparison of Fig. 6.7 aii, bii and cii indicates that after peak inhalation the mean air age distribution at the carbon outlet is consistently below that predicted under continuous steady flow for all breathing profiles. In all cases, the dead zone seen clearly under continuous flow is still visible, but the overall distribution is more uniform.

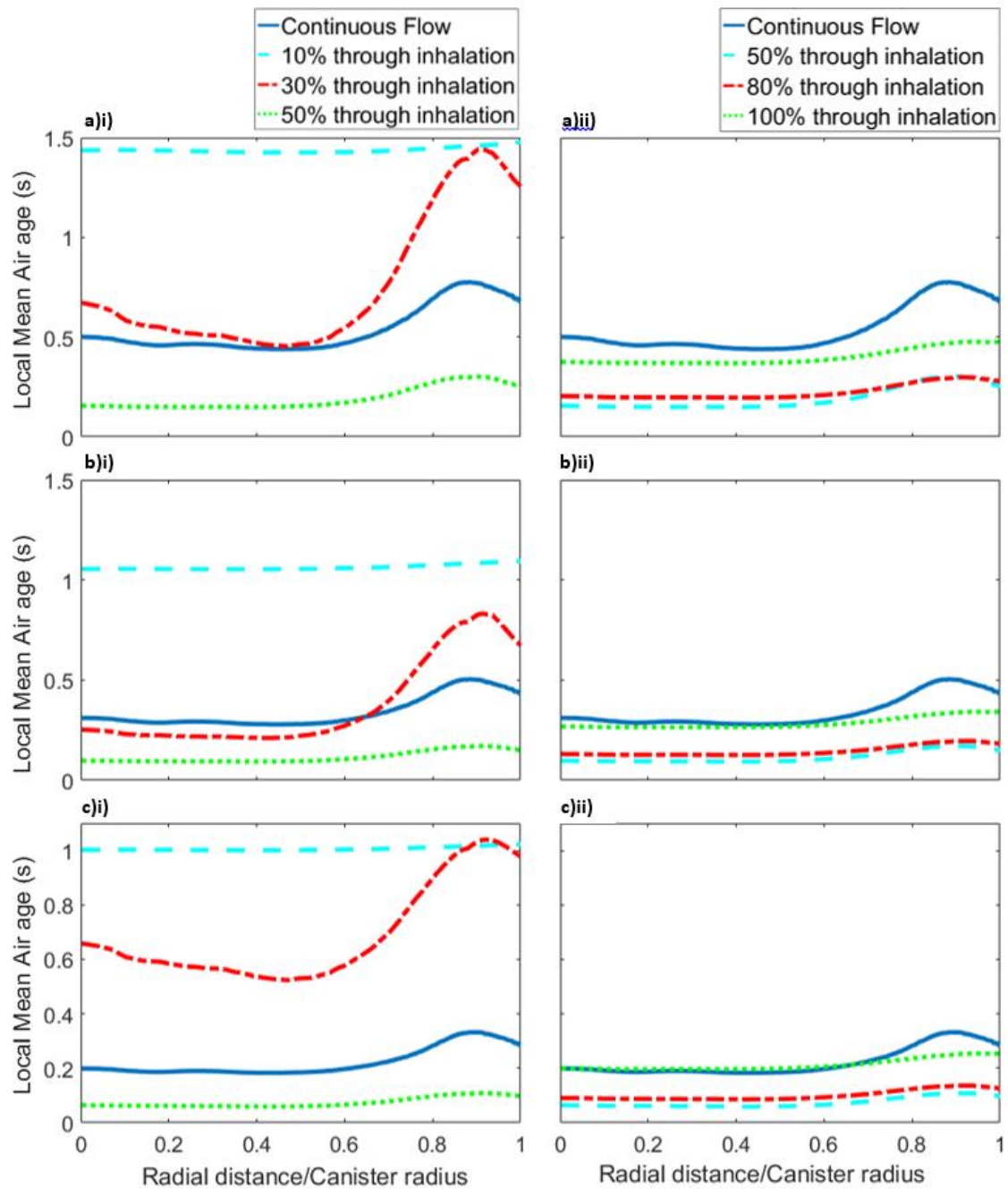


Figure 6.7: Distribution of average residence time with canister radius for (a) light breathing, (b) moderate breathing and (c) heavy breathing in the (i) first half of the inhalation (i.e. while flow rate is increasing) and (ii) the second half of the inhalation (i.e. while flow rate is decreasing).

An iso-surface of mean air age throughout the bed can be used to provide additional information about the efficiency of filter usage and predict the locations of dead zones. For purposes of exemplary demonstration, an arbitrary mean air age of 0.15 s is chosen in Fig. 6.8. Across all three stages of inhalation shown in Fig. 6.8, it is clear that the dead zone towards the canister wall predicted from Fig. 6.7 can be also be seen as a region where the front of low mean air age trails.

An additional dead zone, which is not apparent in Fig. 6.7, can also be seen at the centre of the canister base in the early stages of inhalation. For the mean air age chosen, breakthrough can be seen occurring 33% of the way through the inhalation, occurring first towards the centre of the canister.

A comparison can be made between the residence time profiles for the transient breathing patterns and the equivalent continuous steady flow rate. For the mean residence time chosen here the continuous flow does not predict the breakthrough that is seen under transient conditions.

6.9.3 Breakthrough Profiles

An understanding of the performance of the filter can be gained by investigating the flow at the moment of first breakthrough (i.e. the instant at which air leaving the carbon bed has resided for insufficient time for full adsorption to take place. This is defined for a given contaminant concentration and chemistry, and bed condition)

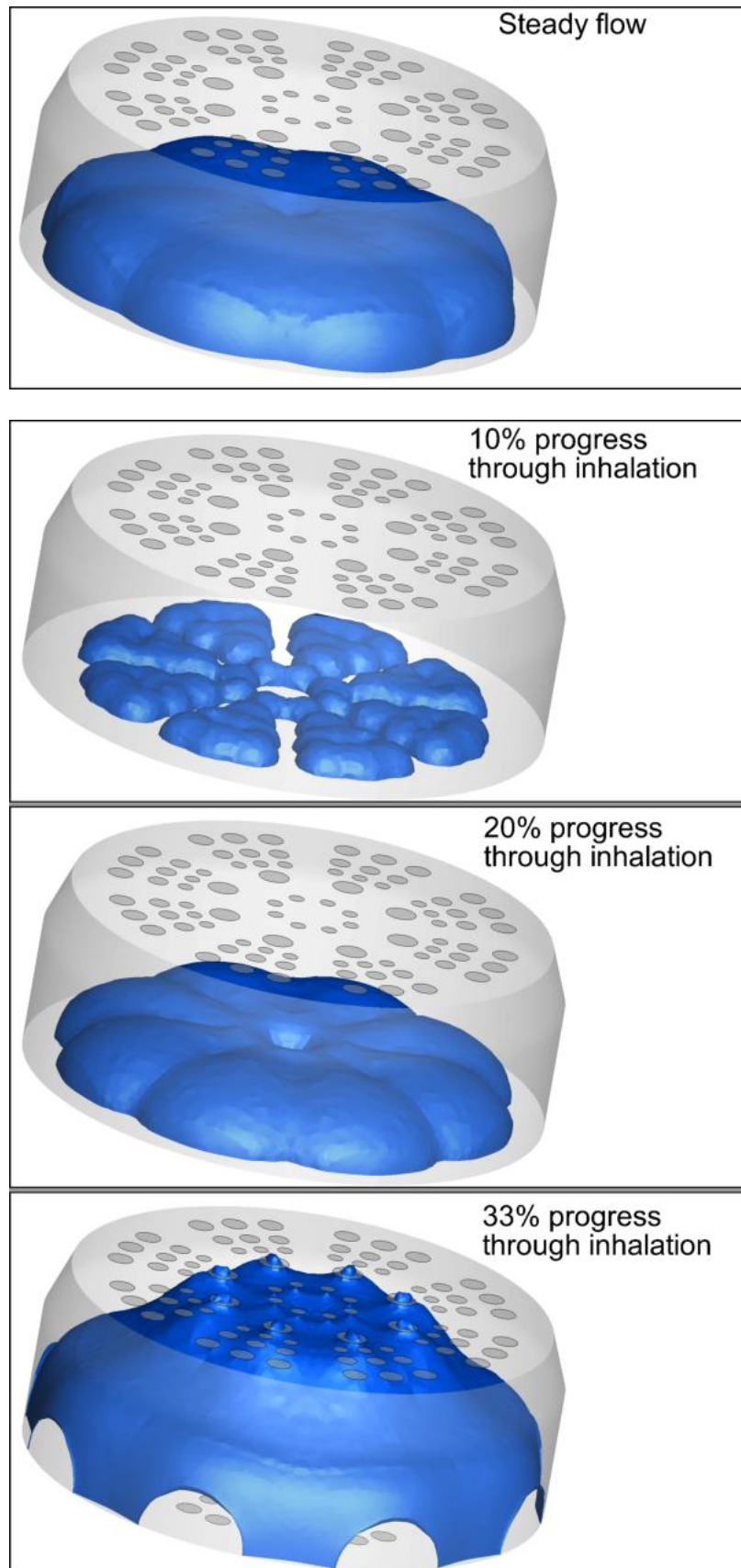


Figure 6.8: The advancing front of a mean air age of 0.15 s throughout the moderate workload breathing cycle and for the equivalent continuous steady flow.

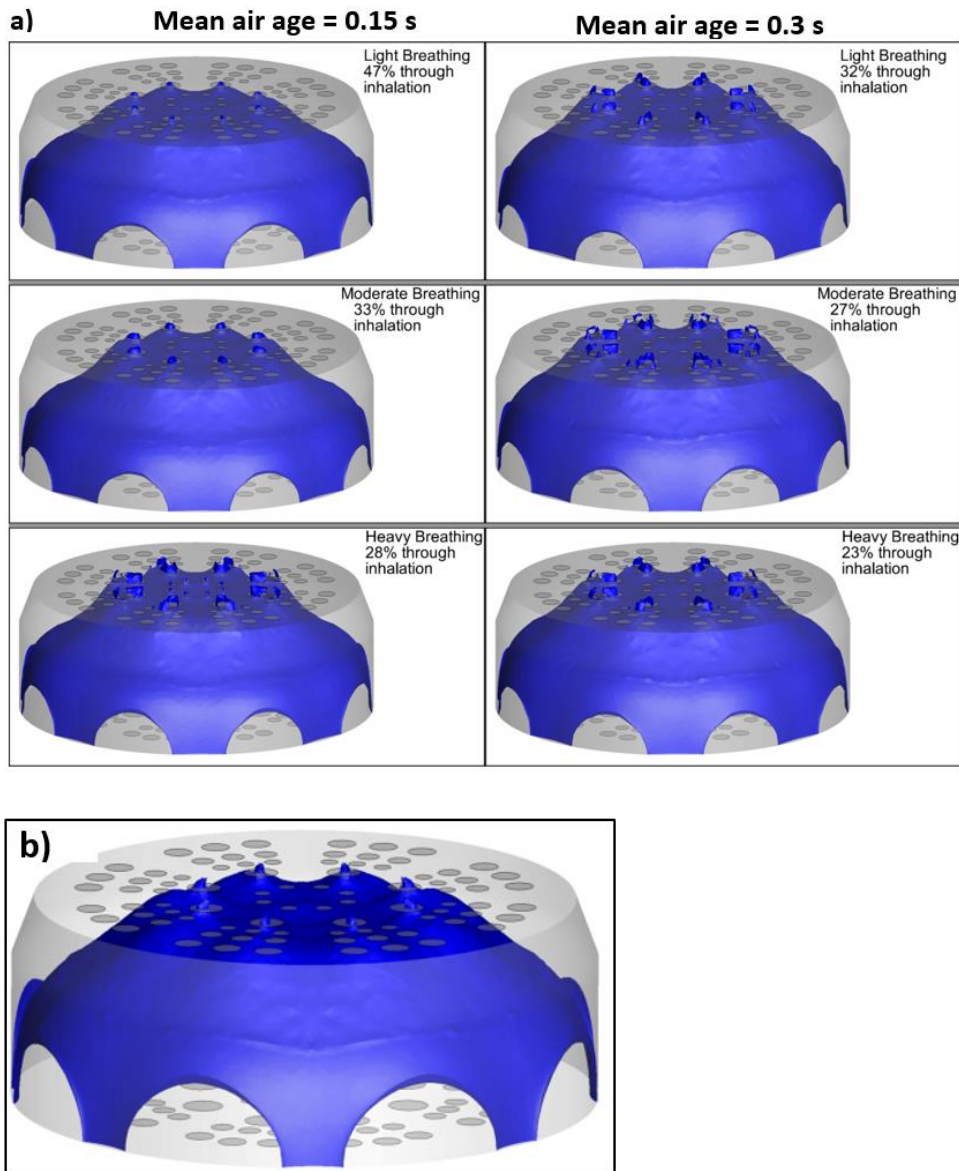


Figure 6.9: a) Distributions of mean air ages of 0.15 s and 0.3 s for each transient breathing cycle at the moment of first breakthrough and b) Profile for the steady-state equivalent of light breathing for a mean air age of 0.434 s, the lowest residence time at which breakthrough will occur.

The distributions of mean air ages of 0.15 s and 0.3 s for each transient breathing cycle at the moment of first breakthrough are shown in Fig. 6.9a. It can be seen from Fig. 6.9a that the distribution at the moment of breakthrough is similar in all cases, independent of both the breathing profile and the mean air age chosen. Breakthrough occurs entirely at the central ring of holes and the low mean air age front trails considerably over the outer edge of the canister, where there are no holes in the base of the carbon bed. This means at the moment of breakthrough there are large regions of carbon, which may remain unutilised. A similar approach is taken for the equivalent

steady-state breathing profiles by inspecting the mean air age profile at the lowest mean air age where breakthrough occurs. This is shown in Fig. 6.9b for light breathing. The profile is extremely similar for the lowest breakthrough mean air ages for each of the other equivalent steady-state cases.

The volume fractions of the carbon bed under two threshold residence times (i.e. 0.15 s and 0.3 s) over the course of each breathing profile are exemplarily shown in Fig. 6.10. It can be seen from Fig. 6.10 that the volume fraction of the carbon bed, which exhibits a residence time smaller than the threshold value, can be considerably greater than the corresponding volume fraction obtained from the equivalent continuous flow under steady-state. This qualitative behaviour remains valid for other mean air ages. Thus, the residence time distribution and accordingly the performance of the canister in terms of breakthrough cannot be reliably estimated from the steady-state equivalent continuous flow simulations.

6.9 Results & Discussion

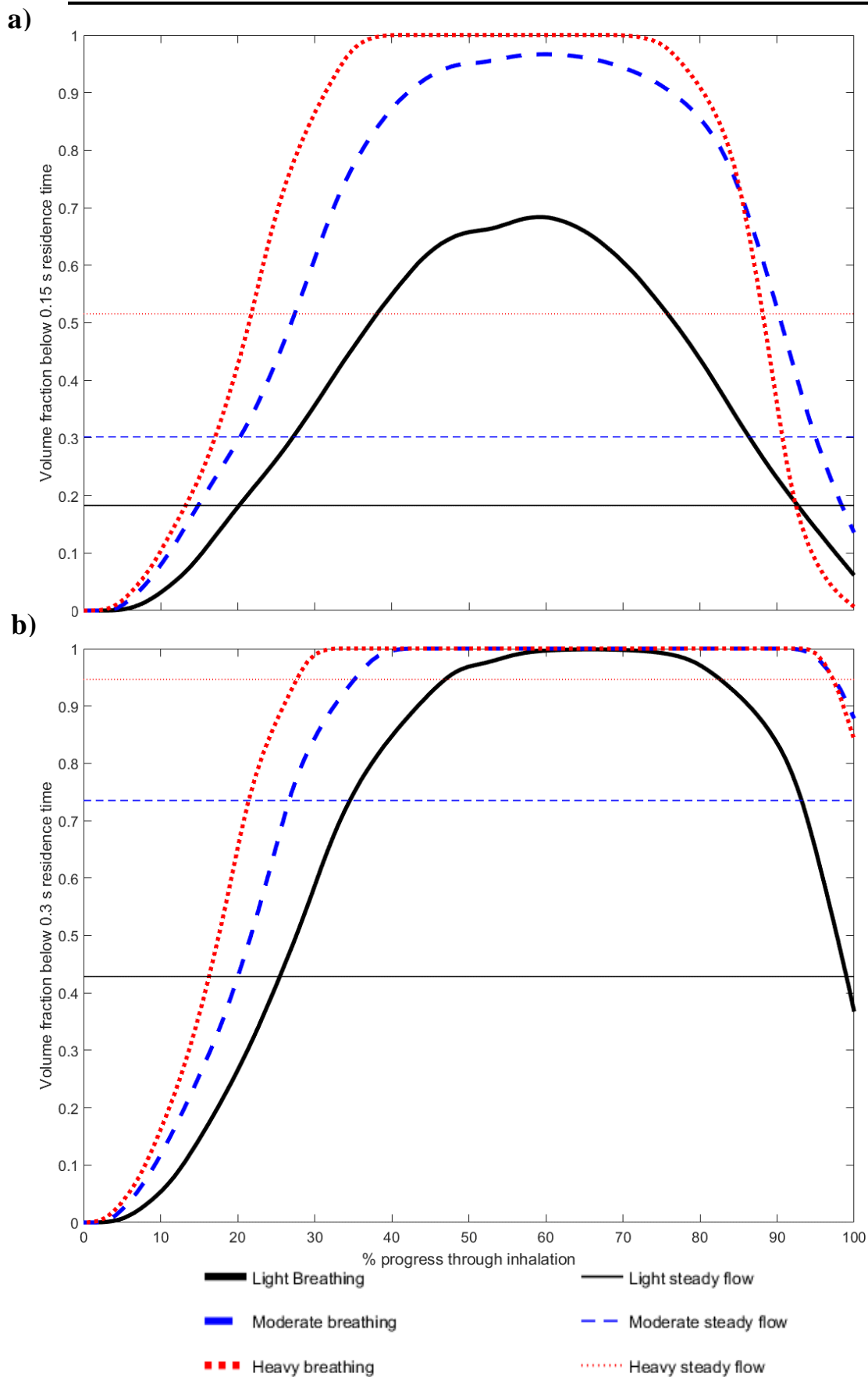


Figure 6.10: The volume fraction of the carbon bed below (a) 0.15 s residence time and (b) 0.3 s residence time throughout each of the breathing profiles

Although residence times under transient flow cannot be reliably estimated from equivalent steady-state continuous flow calculations, it is possible to infer breakthrough times under real breathing patterns from steady-state results in this canister. The lowest residence time that would result in breakthrough for each of the breathing profiles and their steady-state equivalents is shown in Table 6.4.

Table 6.4: A comparison of the lowest residence time seen at the carbon filter outlet for all three breathing patterns and the equivalent steady-state flows

Breathing profile	Lowest breakthrough mean air age under transient flow (s)	Steady-state equivalent lowest breakthrough mean air age (s)	Ratio of transient breakthrough mean air age to steady-state breakthrough mean air age
Light breathing	0.145	0.434	0.334
Moderate Breathing	0.091	0.277	0.329
Heavy Breathing	0.059	0.183	0.322

Although the minimum residence time does not account for adsorption kinetics within the carbon bed, it does provide some indication of whether or not the gas would have spent sufficient time in the bed for full adsorption to occur. As shown previously, it is clear that the minimum residence time predicted under transient flow is considerably smaller than that would be expected under steady-state conditions. Significantly, the ratio of the transient mean air age at time of breakthrough to that under continuous flow remains almost constant (approximately a third) for a range of different flow rates. This suggests that there is considerable potential to estimate if breakthrough will occur under transient breathing profiles even when using steady-state data.

6.10 Key Findings

Transient 3D RANS simulations were carried out on an existing model of a CBRN canister to understand how the transient performance differs from that predicted under steady-state conditions. Simulations have been carried out at three separate breathing rates corresponding to light, moderate and heavy workloads measured previously for an average adult male. The $k - \epsilon$ turbulence model with blended wall functions was found to give a good similarity to the low Reynolds number $k - \epsilon$ model while being both computationally economical and sufficiently accurate. The numerical

modelling has been validated against experimental steady-state pressure drop measurements and it has been shown to give a good agreement.

The pressure drop over the whole canister for each of the transient cases throughout the breathing cycle was compared to that predicted under steady-state flow of the corresponding instantaneous flow rate and it has been found that the transient and steady-state pressure drops were identical, showing that steady-state measurements are an adequate method of estimating pressure drop under transient conditions. The maximum pressure drop for each transient case was much larger than for the steady-state case that corresponded to the same average flow rate, since the peak flow rate was much higher in the transient case.

A study of the mean air age at the top of the carbon bed showed that there was a very large variation in residence time distribution for each of the three transient cases at the same flow rate, suggesting that there is a considerable “history” effect with regards to residence time. The profile of mean air age (averaged across the top of the carbon bed) against radial distance over time was used to relate the steady-state performance and the three separate transient cases. It has been demonstrated that the transient cases corresponding to heavy, moderate and light breathing rates showed somewhat similar residence time profiles at the same fractional duration through the inhalation, with a large area of high mean air age early on, and a more even distribution at the latter stages of the inhalation (although some evidence of a dead zone was seen throughout the inhalation in all cases).

A selection of minimum residence times have been chosen to give an indication of the distribution of flow throughout the canister at the first moment of breakthrough (that is the first point at which air passing out of the carbon bed had not resided in the bed for some arbitrary threshold time). For this particular canister geometry, breakthrough occurs by an identical mechanism across all breathing rates and independent of the mean residence time for breakthrough, and the failure of the filter takes place entirely at the central rings of holes, far from the dead zone at the outer filter.

The minimum residence time seen throughout a breathing cycle was considerably smaller than that predicted using the equivalent steady-state flow rate. However, it was noteworthy that the ratio of minimum residence time under transient flow to continuous flow remained roughly constant (approximately a third) between light, moderate and heavy breathing rate profiles. This implies that there is considerable scope for estimating breakthrough times under transient conditions from continuous flow data, although it remains to be seen if this holds true for other canister geometries.

Chapter 7

Experimental and Numerical Investigation of Linear Driving Force Kinetics in Adsorbent Beds

Previous chapters have used mean air age as a representative indicator of adsorption performance. In this chapter, a numerical model has been developed with the intention of better understanding the relationship between flow characteristics and adsorption behaviour in small activated carbon beds.

7.1 Background

In large beds of porous material, the axial radial velocity profile is expected to be near plug flow, with a thin boundary layer adjacent to the wall [77]. In this case, the plug flow assumption used in the Wheeler-Jonas model discussed in Chapter 3 (Eq. 3.8) will be approximately valid. However, in the case of small beds (or faster axial velocities) such as those seen within a CBRN canister, it is expected that a greater proportion of the flow will be within the boundary layer, and there will hence be a greater deviation from plug flow. Under plug flow conditions, the axial concentration profile associated with adsorption kinetics is well-understood [114]. As the velocity profile deviates from plug flow, there will be coupling between the adsorption kinetics and the flow field, as adsorption reduces the fluid volume flow rate and hence its velocity. Likewise, the fluid velocity will affect the local concentration and residence time and hence the degree of adsorption. It is therefore useful to gain better understanding of flow characteristics in adsorbent beds. This is achieved by carrying out a detailed CFD analysis in this study.

The purpose of this study is to understand the coupled relationship between the adsorption kinetics and the flow profile throughout the bed and relate this to the breakthrough time.

Understanding of the flow profile is achieved by means of unsteady RANS simulations which incorporate an adsorption model. This relationship can then be used to identify how a carbon bed will perform for a range of target adsorptives without the need for detailed adsorption modelling,

with the objective of optimizing future adsorbent bed designs. This would also more easily allow for predicting the behaviours of novel adsorbent materials, such as ordered mesoporous carbons (OMCs) which show improved adsorption kinetics over existing activated carbons [115].

In this study, an experimentally determined adsorption isotherm for cyclohexane on activated carbon has been used as the basis for CFD simulations to predict adsorption behaviour over a variety of inlet flow rates through a cylindrical packed bed of granular activated carbon. These simulations were then repeated, but with modified values of K_M , the LDF kinetic constant (defined in Eq. 3.6), to see how the adsorption kinetics affected the flow field and adsorption performance.

The simulations were validated by conducting experiments to find the breakthrough time of various depths of carbon bed at different flow rates.

7.2 Experimental Method and Results

Isotherm data has been measured using a DVS Advantage sorption analyser from Surface Measurement Systems. A small mass of dry granular activated carbon (approximately 25 mg, supplied by Emcel Filters Ltd) was exposed to a regulated continuous stream of dry air at 298 K. A stream of air contaminated by a known concentration of cyclohexane was then introduced and the change in mass of the activated carbon relative to an inert reference sample was recorded as cyclohexane was adsorbed. When the mass of the carbon remained unchanged for ten minutes the uptake was recorded. The inlet cyclohexane concentration was then increased until the full range of relative pressure (up to $p/p_{sat} = 0.95$) had been covered. Isotherm measurement takes place under automatic control from the instrument software.

This isotherm data (in the p/p_{sat} range of 0.0 – 0.2) was then fitted to the Dubinin-Radushkevich equation presented in Chapter 3 (Eq. 3.5) to identify best-fit values of W_0 and βE_0 , the adsorption energy. The experimental isotherm results and the fitted Dubinin-Radushkevich equation can be seen in Fig. 7.1. The fitted Dubinin-Radushkevich equation clearly gives a close representation of the experimental data and is therefore used in the numerical component of this study.

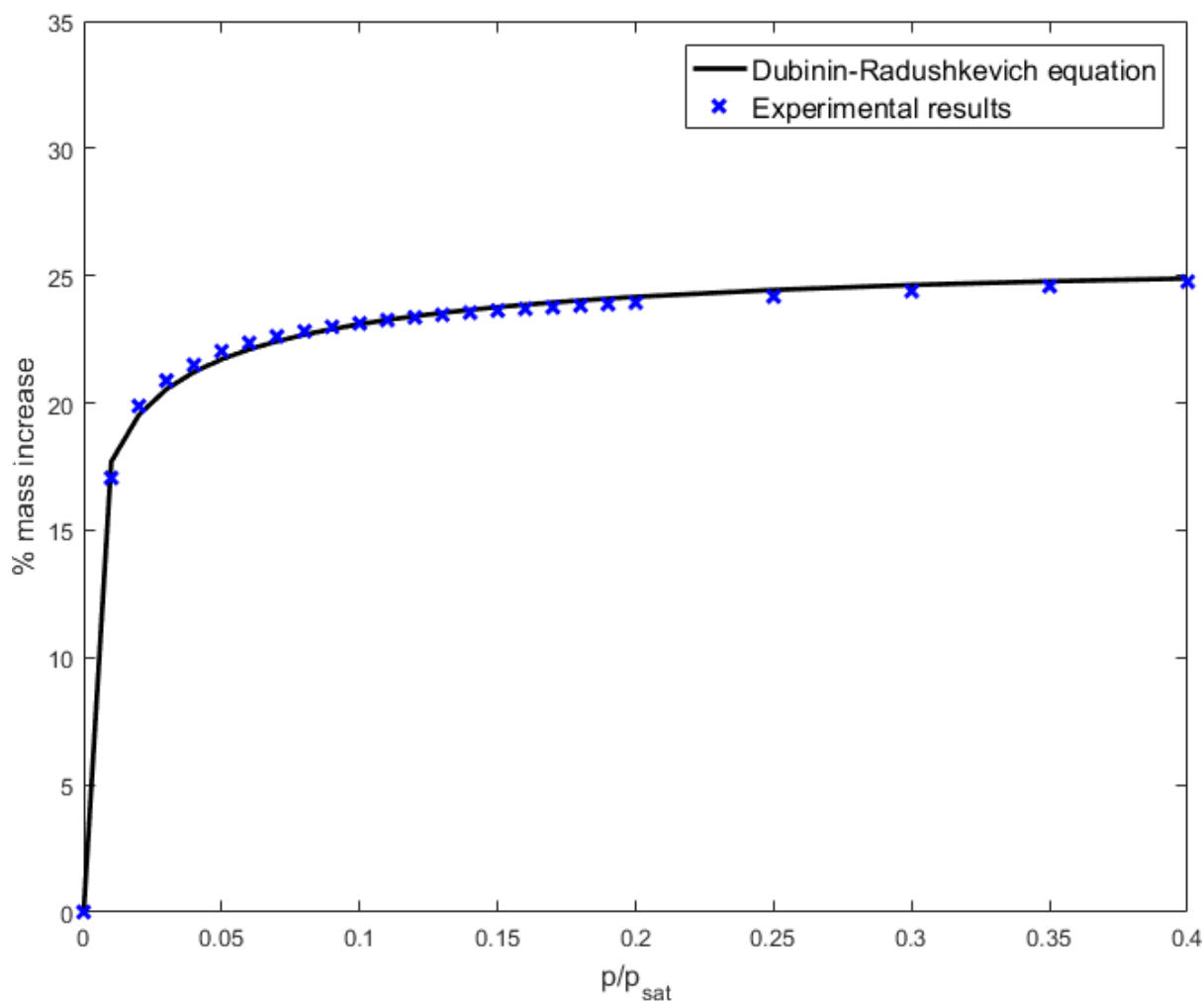


Figure 7.1: The adsorption isotherm for cyclohexane on activated carbon at 295 K and the mass uptake predicted using the Dubinin-Radushkevich equation fitted to this experimental data.

Cylindrical carbon beds with a diameter of 86.5 mm and depths of 15 mm were used to evaluate the breakthrough time of cyclohexane. The beds were packed using the snowstorm filling technique [109] with activated carbon of a mean particle size of 1 mm and a nominal density of 550 kg m^{-3} . The particles exhibited a high degree of heterogeneity with respect to size and shape.

A continuous stream of dry air at flow rates of 15, 30 and 50 L/min (corresponding to inlet velocities of 0.0425, 0.0851 and 0.142 m/s respectively) was drawn through fixed beds of clean activated carbon for a duration sufficient to measure a steady baseline reading at a sampling mass spectrometer at the outlet. An influent concentration of 2000 ppm was then introduced to the air stream. The concentration of cyclohexane in the outlet was measured by mass spectrometry

(monitoring for the mass-to-charge ratio $m/z=84$, the molecular ion for cyclohexane) at one second intervals until a clear breakthrough was observed. The results of this are shown in Fig. 7.2.

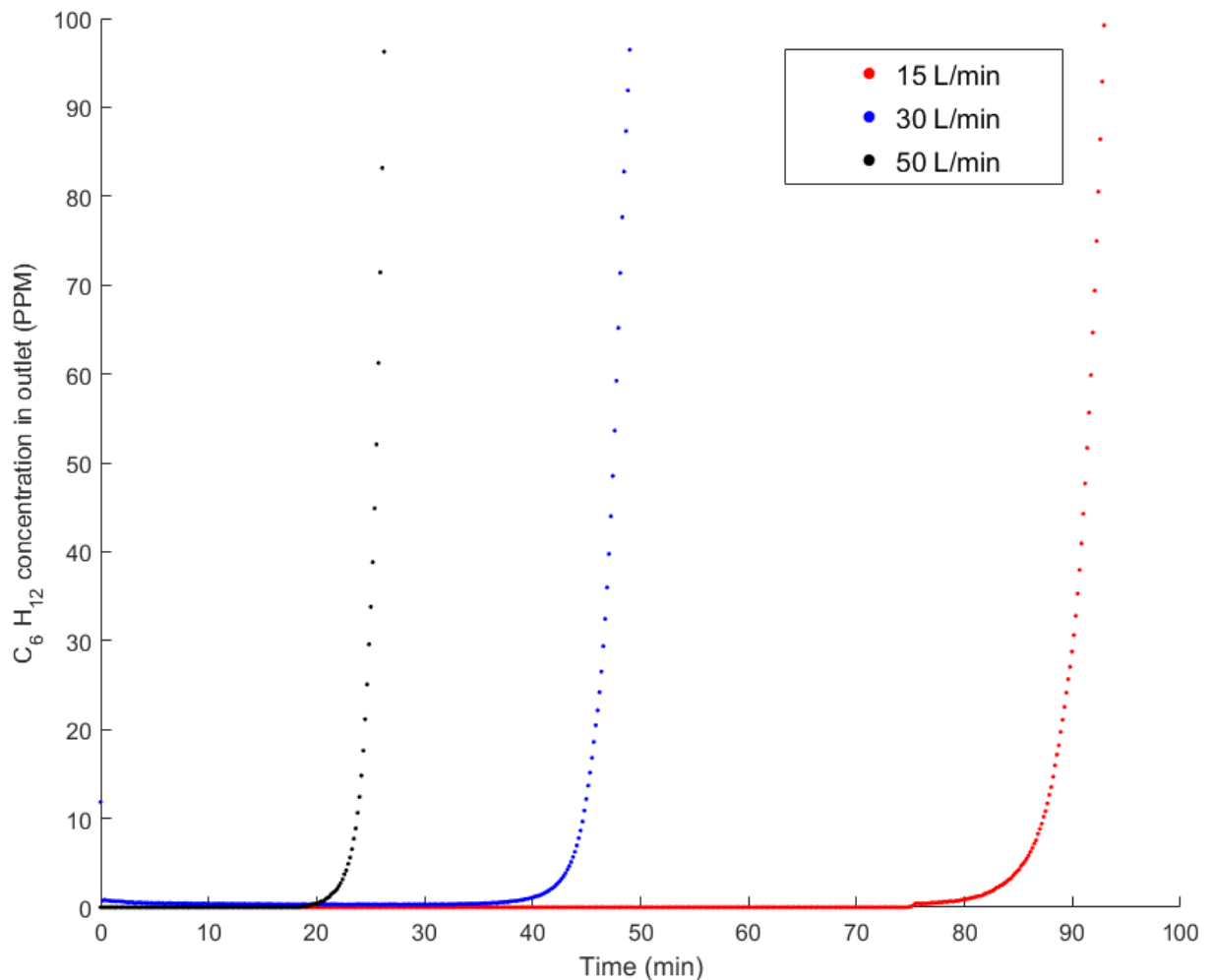


Figure 7.2: Outlet stream concentration of cyclohexane for a 15 mm activated carbon bed exposed to three different inlet flow rates with a concentration of 2000 ppm.

7.3 Numerical Implementation

Simulations have been carried out using Ansys Fluent [19] to solve the modelled unsteady Reynolds averaged equations for the conservation of mass, momentum, energy and species throughout the domain using the finite volume method. The convergence criteria have been given by a scaled residual of 10^{-6} for the energy equation and 10^{-4} for all other equations. Full details of the governing equations and numerical method used are given in Chapter 2.

7.3 Numerical Implementation

In this current study source terms are required for the mass and species conservation equations to account for adsorption. As only one species is adsorbed, the source terms are identical and are given by:

$$\bar{S}_{mi} = \bar{S}_{\alpha,i} = K_M \rho_s (W - W_e) \quad (7.1)$$

Here, W_e is the equilibrium uptake as given by Eq. 3.5. This equation has been selected due to its widespread use with volatile organic compounds and its good match to the experimental data

Within the momentum equation, the source term \bar{S}_{ui} originates from the viscous and inertial resistance of the porous medium:

$$\bar{S}_{ui} = a_1 V_{i,s} + a_2 V_{i,s}^2 \quad (7.2)$$

where a_1 and a_2 are the viscous and inertial resistances specific to the porous medium and $V_{i,s}$ is the superficial fluid velocity in the i^{th} direction.

For the energy conservation equation, the source term $\bar{S}_{ei} = -\beta E_0 \bar{S}_{mi} / M_w$ depends on the experimentally measured βE_0 which is given in Table 7.1.

Turbulence is modelled using the $k - \epsilon$ turbulence model with blended wall functions, as discussed in Chapter 2 (Eq. 2.15 and Eq. 2.16).

The local species concentration is subject to effects of fluctuations in the flow field due to turbulence [116]. However, for larger kinetic constants, the adsorption rate would be governed by both the reaction kinetics and the effect of turbulent mixing. For all cases considered here the kinetic constant is far below the threshold required for turbulent mixing to become significant, so the mean values of mass fraction are used to describe the source term for adsorption seen in Eq. 6 without accounting for turbulent fluctuations [117].

The numerical model used here has been used previously used to give good predictions of pressure drop across an activated carbon bed [118].

7.4 Mesh independence

Mesh independence has been ensured by assessing the initial depth of penetration into the bed and the speed of the advancing contaminated front for three representative cases. The results are shown in Table 7.1. The coarser of the two meshes was selected for use in the main study as the results did not change significantly with grid refinement.

Table 7.1: Results of the mesh independence and validation studies study for the selected cases.

Mesh		No. of cells in axial direction within carbon bed	No. of cells in radial direction within carbon bed	No. of cells in axial direction within open pipe	No. of cells in radial direction within open pipe	Expansion ratio	Total number of cells
A		163	98	142	98	1.1	29890
B		214	115	150	115	1.1	41860
Inlet Flowrate (L/min)	Inlet velocity (m/s)	K_M (s^{-1})	Mesh	Initial contaminated front length (mm)	Contaminated front speed (m/s)		
50	0.142	0.01	A	12.08	1.13×10 ⁻⁵		
			B	12.10	1.13×10 ⁻⁵		
1000	2.836	0.004	A	57.55	2.11×10 ⁻⁴		
			B	57.40	2.11×10 ⁻⁴		
1000	2.836	0.01	A	23.30	2.04×10 ⁻⁴		
			B	23.34	2.04×10 ⁻⁴		

7.5 Operating and Boundary Conditions

All simulations have been conducted on an 86.5 mm diameter cylinder as used for the experimental results. For the simulations, a 15 mm packed bed of carbon with 50 mm clear cylinder at the inlet and outlet has been considered to allow the flow to develop fully. All simulations exploited the axisymmetric nature of the geometry to reduce the computational cost.

An average bead diameter of 1 mm, as used in the experiments is considered in all cases. The carbon bed was treated as a uniform porous medium with a fixed bulk porosity throughout the domain to depict the heterogeneous nature of the carbon used within the experimental study. The viscous and inertial losses throughout the bed are given as follows [105]:

$$\bar{S}_{ui} = (-\Delta\bar{p}/L)_i = 2.39 \times 10^9 \bar{u}_{s,i} + 3.21 \times 10^4 \bar{u}_{s,i}^2 \quad (7.3)$$

7.6 Validation

Cyclohexane was chosen as the test contaminant, as it is commonly used as a representative agent for a variety of volatile organic compounds in the testing of respirator canisters [8], a common application of shallow activated carbon beds. The inlet flow rate was initially chosen to be 50 L/min (corresponding to an inlet velocity of 0.142 m/s) as it has been used previously as representative of a human breathing rate [107]. Inlet flow rates up to 1000 L/min (inlet velocity of 2.836 m/s) were also studied, as it was expected that a greater deviation from the plug flow assumption at higher flow rates. The relevant properties of cyclohexane at 295 K are given in Table 7.2.

Table 7.2: Physical properties used for this study

Cyclohexane Molecular Weight (kmol/kg)	84.17
Cyclohexane Diffusion Coefficient in air (m ² /s) [119]	7.84×10^{-6}
Heat of adsorption (kJ/kmol)*	18945.5
Micropore volume (cm ³ micropore/g carbon)*	0.324
Effective mass transfer coefficient (s ⁻¹)[120, 121]	0.004
Bulk porosity (-)	0.365
Bulk Density (kg/m ³)	550
Mean particle diameter (m)	0.001

*taken from the experimental data discussed in Section 7.2

Turbulence at the inlet was specified in terms of turbulence length scale l and turbulence intensity I which are specified as $I = \sqrt{(2k/3)/V_L} = 10\%$ and $l_t = 0.07d$. A sensitivity analysis revealed that the simulation results are not significantly affected by the numerical values of I and l_t . For each of the inlet velocities investigated the kinetic constant for the LDF model K_M was varied over a range that covers the majority of organic vapours (a range from 0.001 s⁻¹ to 0.01 s⁻¹).

7.6 Validation

The computational method was validated by comparing the breakthrough times for simulations at three different inlet flow rates to the experimental data gathered by the method seen in Section 7.2. A threshold value of 10 ppm cyclohexane at the outlet was considered to be the criteria for breakthrough, as this is this the value used in NIOSH certifications of CBRN canister performance [122].

The simulation results for 15 mm beds are listed in Table 7.3. It is clear from Table 7.3 that the computational method used here provides a good representation of the breakthrough process.

Table 7.3: Comparisons between experimental and numerical breakthrough times at each flow rate.

Flowrate (L/min)	Inlet velocity (m/s)	Experimental breakthrough time (s)	CFD breakthrough time (s)
15	0.0425	5208	5010
30	0.0851	2688	2631
50	0.1418	1407	1440

7.7 CFD Results

Analysis of the adsorption performance has been carried out with respect to the distance through the bed that contamination could be seen. The breakthrough front distance was defined as the furthest point in the bed at which the threshold concentration (1×10^{-6} by mass fraction) was present in the vapor phase. The results have been found to be insensitive to the specific choice of threshold.

The variation of the front distance L_f over time is shown in Fig. 7.3 for cases with $K_M = 0.004 \text{ s}^{-1}$ and $K_M = 0.01 \text{ s}^{-1}$.

7.7 CFD Results

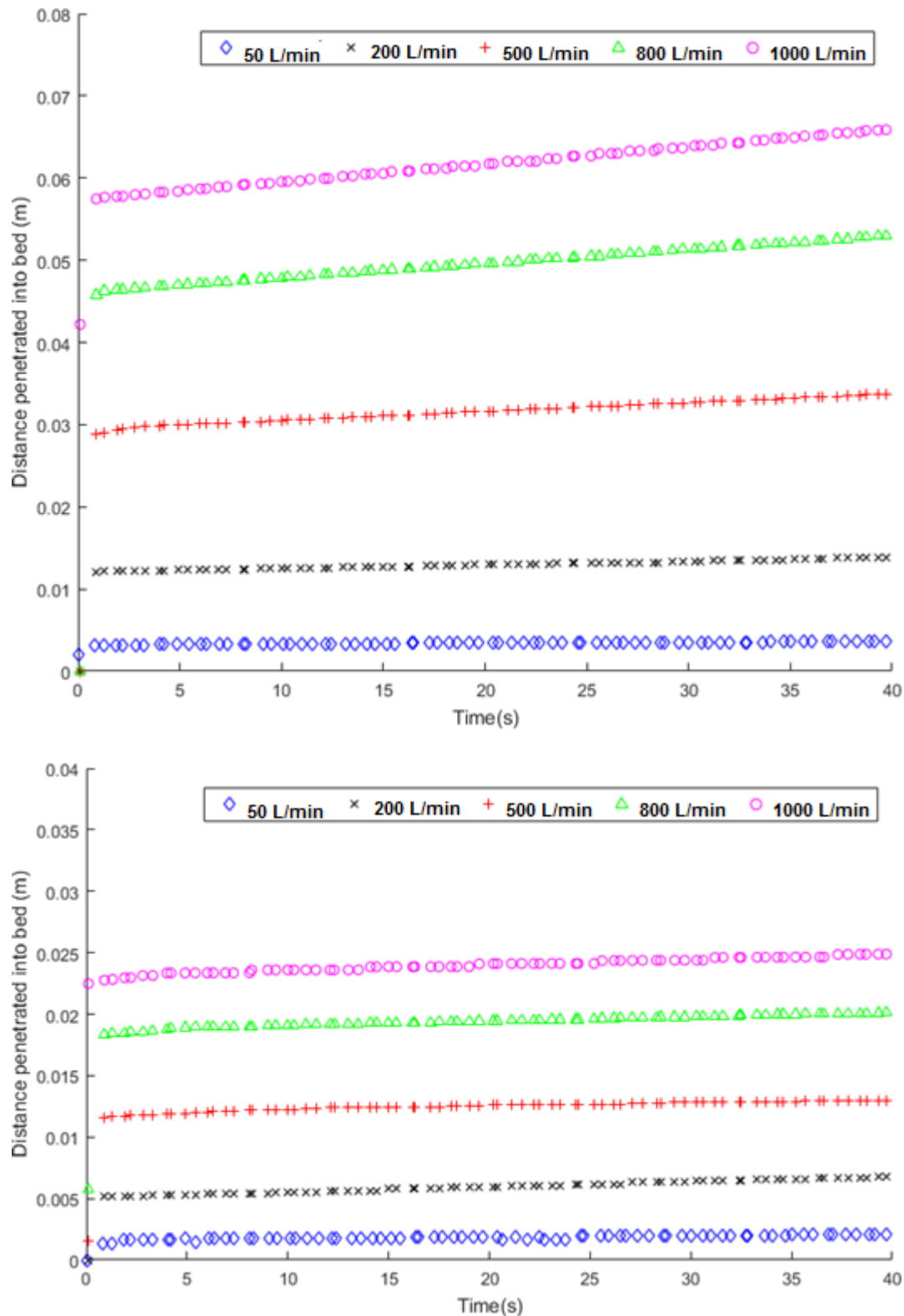


Figure 7.3: The distance into the bed a threshold vapor concentration of $Y_{C_6H_{12}} = 0.0001$ can be seen for (a) $K_M = 0.004 \text{ s}^{-1}$, (b) $K_M = 0.01 \text{ s}^{-1}$.

It can be seen from Fig. 7.3 that a near instant jump in L_f occurs as the contaminant first enters the bed. The magnitude of this initial penetration into the bed is much greater at low values of K_M . In

all cases, after this initial penetration into the bed, the front progresses gradually at a reduced speed, v_f , which increases with increased inlet velocity, until breakthrough occurs.

A comparison can be made to the Wheeler-Jonas equation (Eq. 3.8), which may be re-written to express the front distance (L_f) into the bed over time in the following manner:

$$L_f = \left(\frac{C_{in} v_{in}}{\rho_B W_e} \right) t + \frac{V_L}{k_{WJ}} \ln \left(\frac{C_{in}}{C_{out}} \right) \quad (7.4)$$

In this equation, the penetration of the target vapor concentration into the bed is composed of two distinct elements:

- A steady constant increase in penetration length over time, which is independent of the adsorption kinetics.
- An initial, instantaneous penetration into the bed, which is inversely proportional to the kinetic constant.

The relationship between the simulated results and the Wheeler-Jonas model is investigated by separating the bed penetration into two components, the initial penetration length L_{IP} and the front speed v_f . Both these quantities can be defined with respect to some threshold concentration C_{out} .

In the simulated results, L_{IP} can be clearly identified from Fig. 7.3 as the near instantaneous jump in L_f within the first few seconds of each case, whereas v_f can be identified by the gradient of each set of data in the time that follows the almost instantaneous jump.

The time-independent term of the Wheeler-Jonas equation (Eq. 7.4) suggests that the initial breakthrough distance should be inversely proportional to the kinetic constant [123]. The relationship between V_L/K_M and L_{IP} can be seen from Fig. 7.4 for all cases investigated. It is evident from Fig. 7.4 that using the LDF model for adsorption kinetics gives a similar trend to the Wheeler-Jonas model (Eq. 7.4). This behaviour appears consistently over the full range of flow rates used in this study.

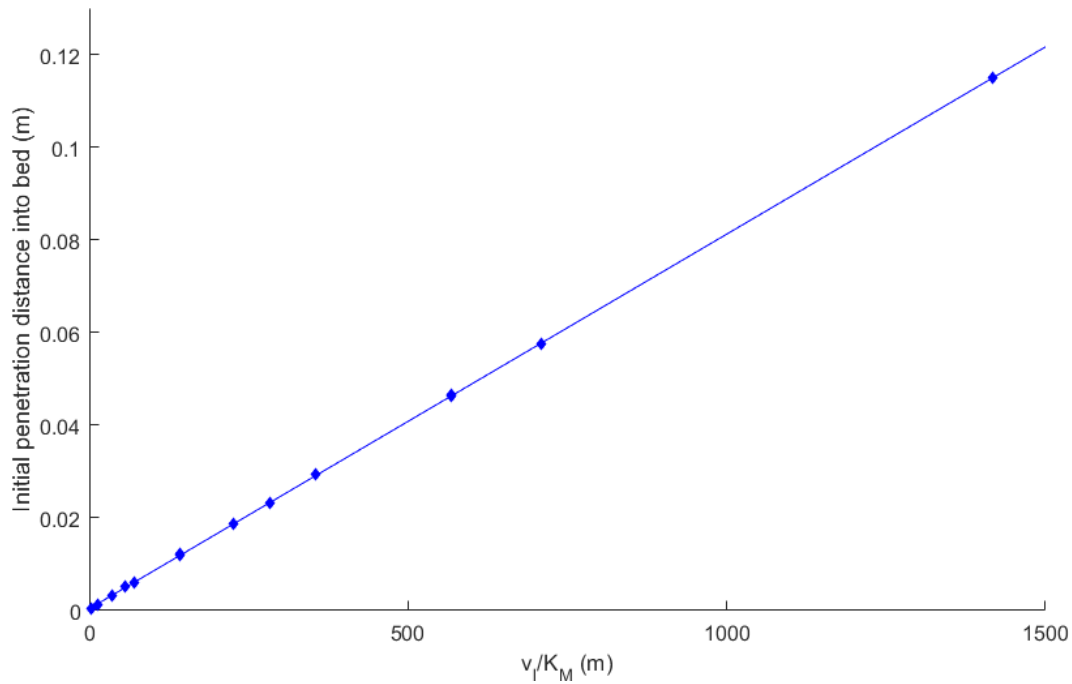


Figure 7.4: Distance contaminant penetrates into the bed in the initial rapid stage, seen against V_I/K_M .

The speed of the front v_{WJ} moving through the bed after the initial period of rapid penetration can be investigated by comparison with that predicted by the Wheeler-Jonas equation as:

$$v_{WJ} = \frac{c_{in}V_L}{\rho_B W_e} \quad (7.5)$$

where $c_{in}V_L$ gives the rate at which contaminant enters the bed, whereas $\rho_B W_e$ represents the total adsorbent capacity of the bed at equilibrium with the inlet contaminant concentration. This gives v_{WJ} as the rate at which contaminant enters the bed over the adsorption capacity of the bed. The ratio of the front speed seen in the results of the CFD simulations to v_{WJ} is a key parameter for identifying deviations from plug flow in a small activated carbon bed, which is presented in Fig. 7.5.

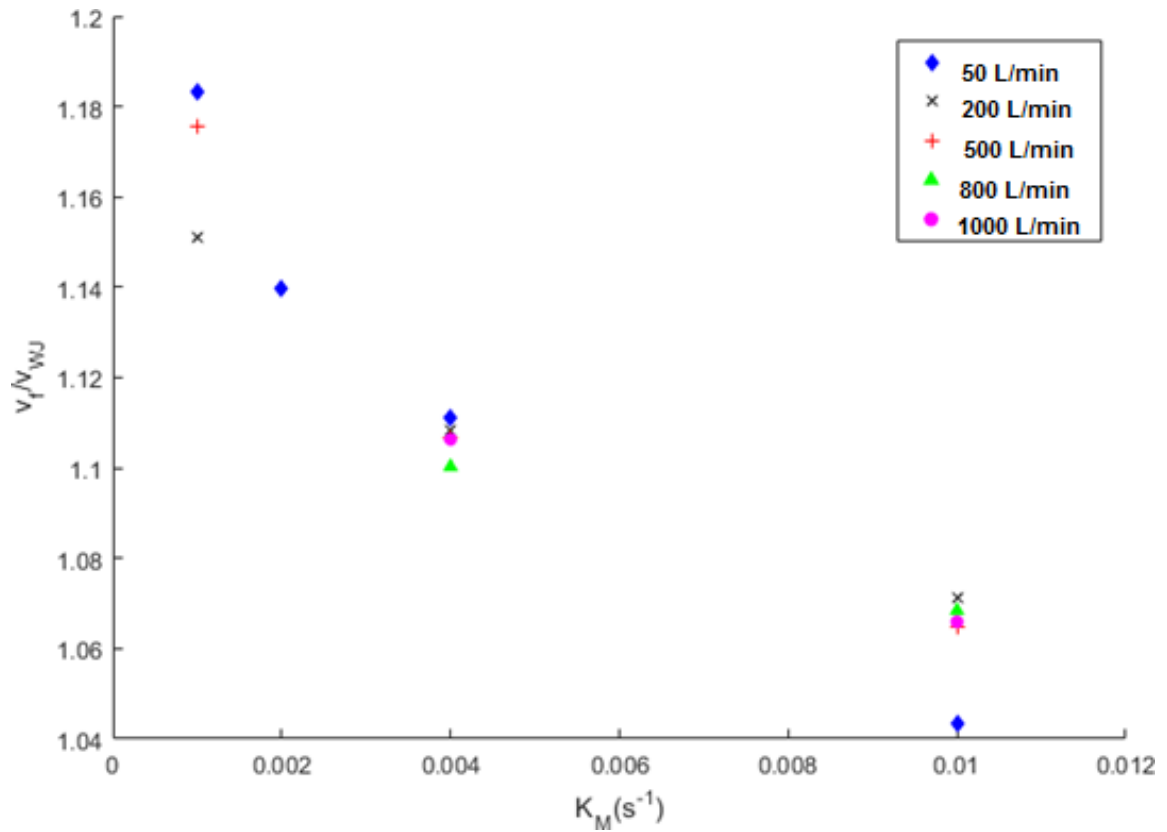


Figure 7.5: Ratio of front speed to front speed predicted from the Wheeler-Jonas equation for different inlet velocities and values of K_M .

As expected, in all cases the front speed slightly exceeds the value that would be predicted by the Wheeler-Jonas equation (Eq. 7.3), as true plug flow is impossible due to the no slip condition at the canister wall. It can be seen from Fig. 7.5 that there is a slight but significant tendency for lower values of K_M to produce greater front speeds, an effect that is not predicted by the Wheeler-Jonas equation.

An explanation for this kinetic-dependent deviation from the plug flow case may be seen by investigation of the distribution of uptake throughout the bed, as seen for each value of K_M investigated for two example flow rates in Fig. 7.6.

7.7 CFD Results

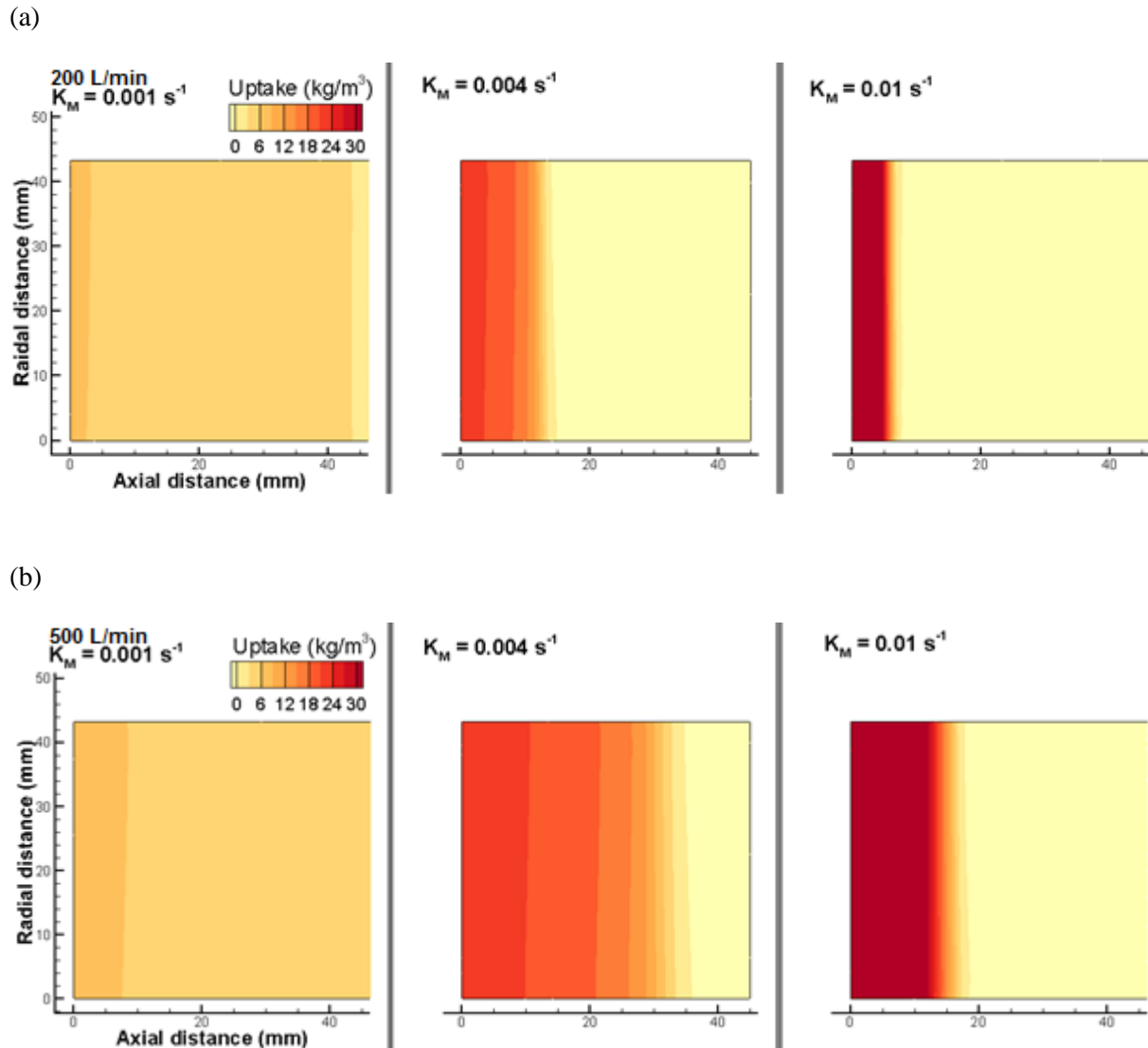


Figure 7.6: Distribution of uptake of contaminant throughout the bed after 60 s exposure at (a) 200 L/min (inlet velocity 0.567 m/s) and (b) 500 L/min (inlet velocity 1.418 m/s).

For each of the cases, after an equivalent time under exposure (and hence an equivalent total amount of contaminant within the bed) the distribution of contaminant can be seen to differ greatly. In general, this results in a greater contaminated volume with slower adsorption kinetics, as the contaminant spreads deeper into the bed. In contrast, when the kinetics are fast a small region of high concentration can be seen.

As adsorption occurs, the volume of fluid flowing through the filter decreases. This will result in a slight reduction in fluid velocity as the flow area remains unchanged. This coupling between the adsorption kinetics and the front speed is not accounted for by the Wheeler-Jonas model. An example of the variation in fluid velocity distributions seen at equivalent flow time is shown in Fig.

7.7. This is in contrast with a typical uniform bed without adsorption, in which the expected velocity profile is a thin boundary layer at the wall, with plug flow seen throughout the center of the domain [77].

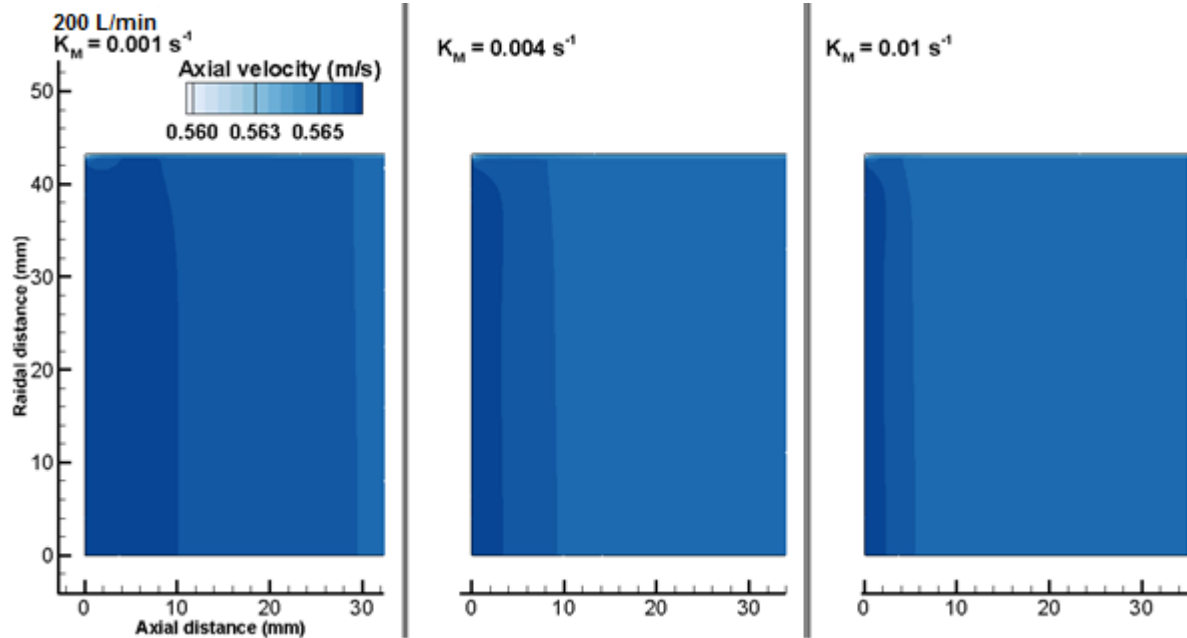


Figure 7.7: Axial velocity distribution close to the inlet of the bed for an inlet flowrate of 200 l min^{-1} (corresponding to an inlet velocity of 0.567 m/s) seen 60 s after first exposure.

Moreover, the generation of turbulence within the carbon bed may also influence the velocity profile. The generation of turbulent kinetic energy is driven by the velocity gradient, as can be seen from Eq. 2.9. An increased velocity gradient due to adsorption taking place over a smaller volume (as seen in the cases with faster adsorption kinetics) will result in greater generation of turbulent kinetic energy and alter the mean velocity profile.

The distribution of contaminant in the inlet stream will also have some impact on the distribution of uptake in the bed, which may affect the speed at which the front then advances through the bed. A sample mass fraction profile just before the contaminant reaches the carbon bed is shown in Fig. 7.8. Although the contaminant is introduced as a plug flow, a non-uniform radial distribution is observed as it flows through the cylinder towards the bed. This is due to the velocity profile caused by the no-slip condition at the wall, and the turbulent mixing in the axial direction towards the axis. This results in a low concentration of contaminant at the centerline reaching the carbon first, and a maximum concentration further from the axis.

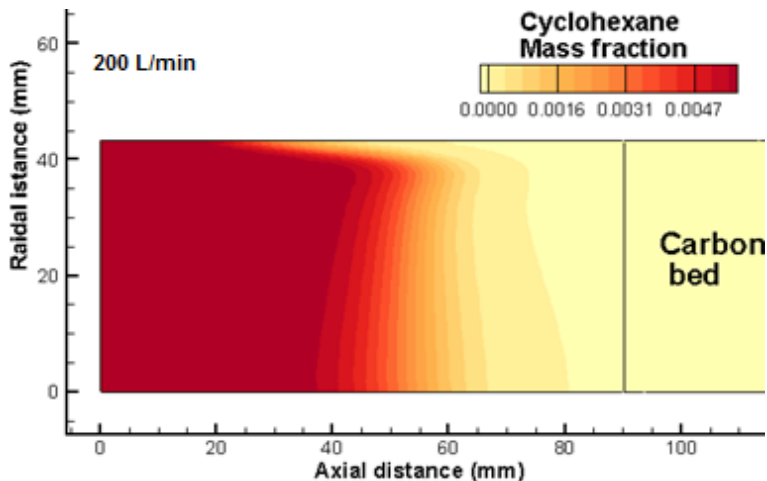


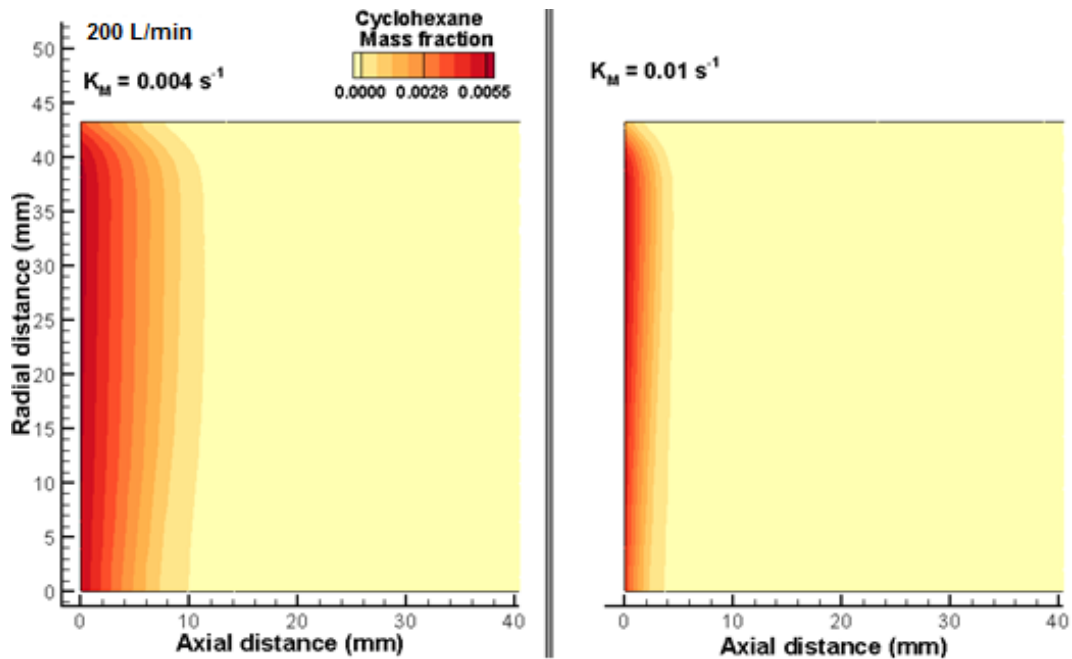
Figure 7.8: The distribution of contaminant in the inlet stream at 200 L/min (inlet velocity 0.567 m/s) immediately before it first contacts the carbon bed.

The effect of this distribution can clearly be seen on the shape of the front when the contaminant first penetrates into the bed. Examples of this behaviour are shown in Fig. 7.9 for two different flow rates. Although the first point of entry into the bed occurs along the centre line, the axial distribution of contaminant results in a much shorter initial penetration into the bed. In contrast to this, further from the axis where the peak concentration is higher, the initial penetration distance is significantly increased.

The impact this has later after the initial moment of exposure can be seen in Fig. 7.10 for flow rates of 200 L/min and 500 L/min. A close inspection of the contaminant distribution in the vapour phase close to the center line shows that the adsorption profile in the radial direction at the front is dependent on the adsorption kinetics. At $K_M = 0.004 \text{ s}^{-1}$, the maximum distance the threshold cyclohexane concentration is obtained along the axis within the carbon bed. However, for $K_M = 0.01 \text{ s}^{-1}$, this maximum distance is found to be slightly offset from the axis, in a manner reminiscent of the profile seen when the contaminant first enters the bed. This suggests that for faster kinetics, the distribution of concentration at the earliest stage of exposure results in an effect, which is retained for much longer. The difference in contaminant distribution at different stages in filter lifetime for different adsorption kinetics may account for the variations in front speed. The precise effect seen here is specific to the geometry considered and the inlet contaminant distribution; however, in any case where contaminant is introduced there is likely to be a non-uniform

distribution in the inlet stream and a similar relationship between kinetics and entry contaminant distribution.

(a)



(b)

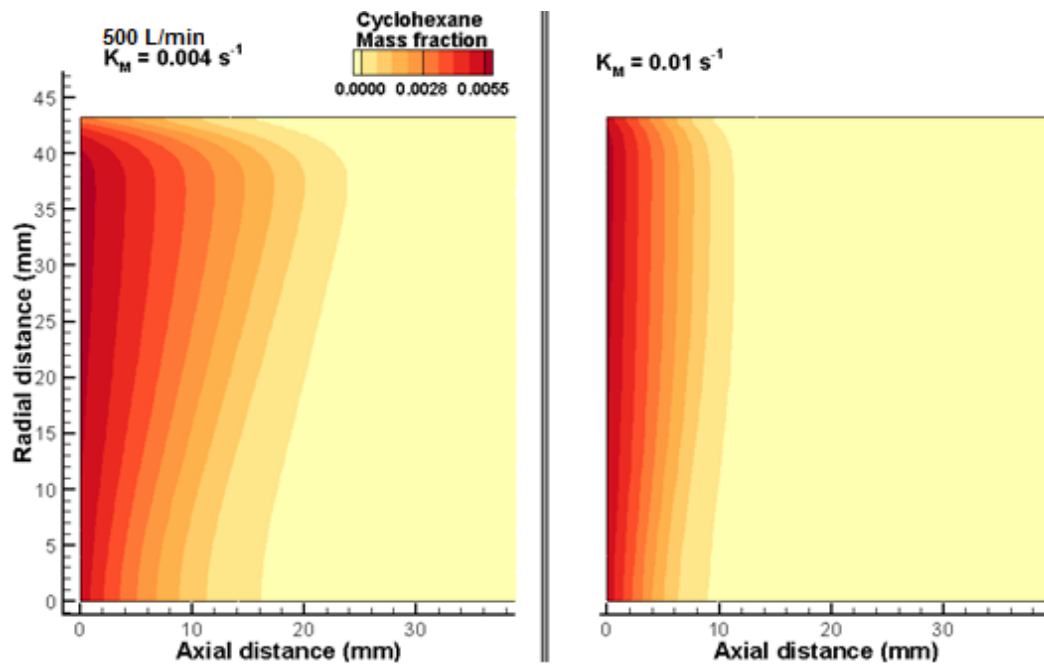


Figure 7.9: Distribution of contaminant in the carbon bed 0.1 s after initial exposure at (a) 200 L/min (inlet velocity 0.567 m/s) and (b) 500 L/min (inlet velocity 1.418 m/s) for $K_M = 0.004 \text{ s}^{-1}$ and $K_M = 0.01 \text{ s}^{-1}$.

7.8 Key Findings

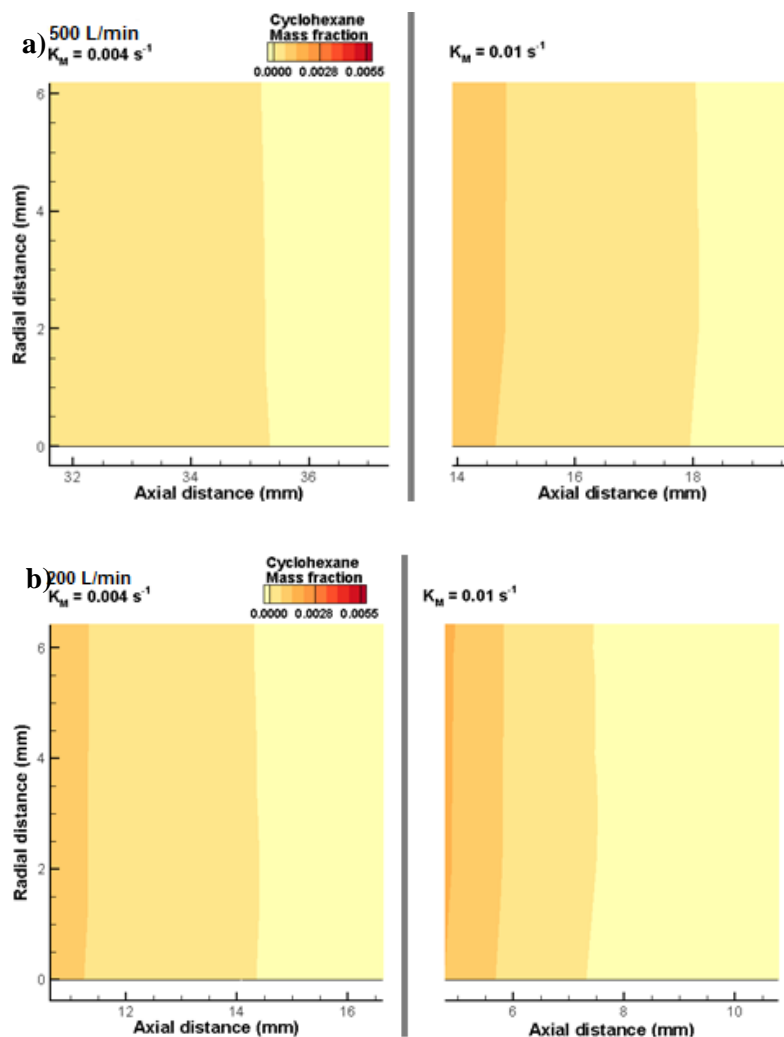


Figure 7.10: Distribution of contaminant close to the center line 60 s after initial exposure at (a) 200 L/min (0.567 m/s inlet velocity) and (b) 500 L/min (1.418 m/s inlet velocity) for $K_M = 0.004 \text{ s}^{-1}$ and $K_M = 0.01 \text{ s}^{-1}$

7.8 Key Findings

A numerical model has been developed to predict the flow behavior in small activated carbon adsorbent beds. Cyclohexane has been chosen as the test contaminant and its adsorption was modelled in accordance with the Dubinin-Radushkevich isotherm with linear driving force (LDF) kinetics. Breakthrough times predicted by the model have been shown to provide an excellent match to experimental breakthrough data for cyclohexane. The model has been utilized to analyze the effects of flow rate on adsorption performance so that the assumption of plug flow, which is commonly held as an assumption in the analysis of carbon beds, can be assessed.

Simulations have been carried out over a range of flow rates from 50 L/min to 1000 L/min, as it was expected that the deviation from the plug flow assumption would be greater at higher inlet flowrates. The contaminant used represented cyclohexane, to match the experimental data. The LDF kinetic constant has been varied over a range from 0.001 s^{-1} to 0.01 s^{-1} , which is representative of a wide range of volatile organic compounds, to isolate the effects of kinetics on adsorption performance.

The distance at which a threshold contaminant concentration could be seen into the bed at a given time has been investigated over the bed lifetime. In general, it has been noted that a period of very rapid (<1 second) penetration into the bed occurred after the initial exposure. The contaminant (in the vapour phase) has been seen to advance at a constant rate for the rest of the bed lifetime. This behaviour is similar to that predicted from the mass-balance derived Wheeler-Jonas equation for plug flow in carbon beds.

It has been found that the initial period of rapid penetration into the bed was directly proportional to the flow velocity and inversely proportional to the kinetic constant ($\propto V_L/K_M$), a trend that was closely followed for all flow rates and kinetic constants. This was in line with the expected behaviour seen from the plug flow analysis.

The speed at which a front of a given concentration would advance through the bed after this initial period would be expected to be entirely independent of K_M from the plug flow analysis. In all cases, the front speed has been found to be slightly quicker than the plug flow analysis would predict, although over the range of inlet velocities used in this study there was no apparent greater deviation from plug flow for the higher inlet velocities. However, a trend has been seen in which the ratio of front speed seen to the expected plug flow front speed has been found to be greater when the adsorption kinetics were slower.

It can be seen that the kinetics modify the velocity profile throughout the bed, as the volume flow rate of the fluid decreases with adsorption, resulting in an overall decreased velocity downstream. In the cases with fast kinetics, the adsorption takes place over a smaller overall volume

7.8 Key Findings

of carbon, resulting in a more rapid fluid deceleration. This increased velocity gradient in the axial direction will result in increased generation of turbulence, which may modify the flow field.

Additionally, the concentration profile of contaminant in the inlet stream at the moment of first exposure affects the shape of the contaminated region in the bed. The contaminant has been found to enter the carbon bed first at the axis but at a lower concentration, while the peak concentration at the earliest stages of exposure will be seen further from the axis. This results in the contaminated front in the early stages of exposure having a distinctive shape where the furthest contaminated distance into the bed does not fall on the centre line. In the cases with low kinetic constants, this front shape has been obtained only shortly after initial exposure. However, in the cases with fast kinetics the forward-most contaminated point in the bed has been found to be offset from the axis for the whole duration of the simulation. This suggests that there is a “history” effect of the inlet contaminant distribution when the adsorption kinetics are fast. The precise nature of this effect is likely to vary with different inlet contamination profiles. Porosity effects on the adsorption performance within the bed are further examined in Chapter 9.

Chapter 8

Modelling the Stochastic Nature of Porosity in a Respirator Canister

In this chapter, a model has been developed to represent the stochastic nature of the activated carbon bed within a generic Chemical Biological Radiological and Nuclear (CBRN) respirator canister. The porous region is subdivided into discrete sections which are assigned a porosity based on their radial position according to a longitudinally-averaged porosity model, and then perturbed by some amount according to a Gaussian distribution. The porosity model was used in Reynolds-Averaged Navier-Stokes (RANS) simulations in order to assess the impacts that the choice of section size and the porosity variation would have on the pressure drop and residence time distribution of the canister.

8.1 Background

Previous chapters have considered that for the packed spheres within a carbon bed, the interaction between the particles and the walls can be adequately depicted by a longitudinally-averaged porosity profile, such as the Mueller equation. It has been found that, for given particle and cylinder diameters and particle mass fraction, the longitudinally averaged porosity will show little variation between individual packings [124]. However, in real packed beds the exact nature of the packing is highly stochastic in nature, and individual cross sections at different longitudinal distances throughout the bed may vary greatly in terms of their individual porosity profiles. Previous studies using Magnetic Resonance Imaging (MRI) [125] and Gamma-ray tomography [126] have demonstrated considerable heterogeneity throughout the bed, which can have a significant impact on the flow profile. A precise understanding of the porosity distribution throughout an entire bed can only presently be gained by use of similar observation techniques, which are expensive, impractical and highly specific to the single individual packing. A statistical approach to understanding the voidage is therefore preferred.

Several studies have represented the porosity distribution as random perturbations around the longitudinally averaged radial porosity profile according to a probability distribution function (PDF) [85, 96, 97, 127]. A Gaussian distribution has previously been shown to give a good depiction of the porosity profile for small particles [96, 128].

A number of previous studies have used CFD to consider the impact of flow characteristics throughout the activated carbon bed [46, 105, 118, 129], considering the effects of bracket shaping, canister geometry and different breathing patterns. In all cases the porosity has been modelled using an “effective porous medium” approach, in which individual particles are not represented but the porosity is instead included as a source term within the momentum conservation equation. Modelling of discrete particles is highly computationally expensive and is impractical for such applications[124]. Previous works have therefore considered either a uniform porosity throughout the adsorbent bed, or a longitudinally averaged radial porosity profile.

CFD studies that incorporate the statistical nature of the porosity distribution in trickle-bed reactors by pseudo-randomly varying the porosity about the expected longitudinally averaged porosity have been conducted in the past [85, 96].

In this chapter a porosity model is developed which subdivides the carbon bed within an existing CBRN canister into sections. Each section is then assigned a constant porosity based on its radial position according to the Mueller equation (Eq. 3.10) and perturbed according to a Gaussian distribution. The impact that the section size and porosity variation have on pressure drop over the length of the canister, and on the residence time of air leaving the canister has been assessed for a fixed inlet flow rate. The range of section sizes over which a section based model would be appropriate was also assessed, and a limited number of cases were also simulated at higher inlet flow rates to see if the same trends would persist.

8.2 Numerical Modelling

RANS simulations were conducted using the commercial software Ansys Fluent [19]. The discretised mass and momentum conservation equations were solved using the finite volume

technique. A scaled residual convergence criterion of 10^{-6} was used for all variables. Full details of the numerical scheme and governing equations are given in Chapter 2. Turbulence is modelled using the $k - \epsilon$ turbulence model with blended wall functions,

In addition to the mass, momentum and turbulence equations, an additional scalar transport equation has been included in the form of mean air age τ transport equation (Eq. 3.1)

The mean air age represents how long on average air at a given location will have been resident within the adsorbent bed. It has previously been used as a good indicator of the bed's adsorption capability [6, 41, 42], without the computational expense of detailed adsorption modelling.

8.3 Geometry and Boundary Conditions

The computational domain considered here is identical to that used in Chapter 6, shown in Fig 8.1.

At the inlet the mean velocity U was specified as 0.619 m/s, to give an inlet Reynolds number of 1000. Turbulence at the inlet was specified using a turbulence intensity $I = \sqrt{2k/3}/U = 10\%$ and a turbulence length scale and $l_t = 0.07d$ where d is the inlet diameter. The results were found to be insensitive to the choice of turbulence boundary conditions as turbulence is rapidly damped by the first layer of filtration. The outlet obeyed the Neumann boundary condition (no change in primitive variables in the normal direction to the outlet). The walls obeyed the no-slip condition and were impenetrable, and the turbulent kinetic energy was taken as zero at the walls.

8.4 Porosity model

The porosity of the activated carbon bed is incorporated into the CFD model by means of a source term in the momentum equation, which is described by the Ergun equation (Eq. 5.2).

A model has been developed to incorporate the global statistical nature of the porosity distribution into the CFD simulations. The activated carbon domain was subdivided into regular tetrahedral units of uniform size (of a larger size than the computational mesh). If a cell centre fell within one of these units the whole cell was considered to be within. This resulted in the domain

being divided into roughly uniformly-sized sections of roughly tetrahedral shape – the sections were not perfectly uniform due to the unstructured nature of the computational mesh.

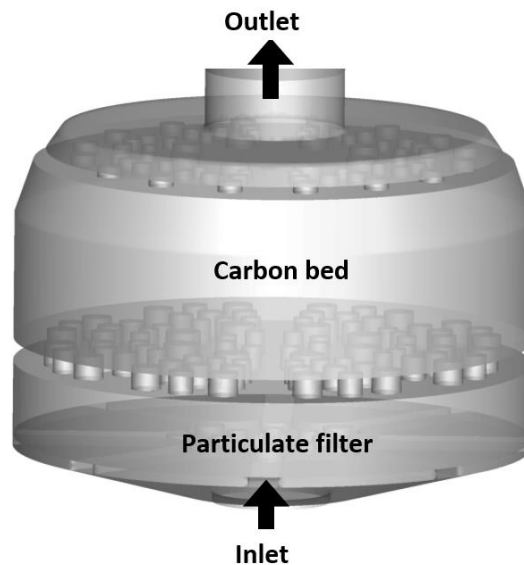


Figure 8.1: Geometry of the CBRN canister simulated in the current study.

Each section is assigned a porosity, which is uniform throughout that particular section. An initial estimate for the section porosity is taken from the Mueller equation (Eq. 3.10) based on the radial position of the section centre. The stochastic nature of the porosity distribution is represented by perturbing the porosity according to a Gaussian distribution. This results in a pseudo-random porosity profile which is defined by two new parameters:

- The length scale of the section subdivisions.
- The standard deviation of the Gaussian distribution which is used to perturb the Mueller porosity.

Simulations were conducted using section sizes of 0.5 mm, 0.72 mm, 1 mm, 2 mm and 5 mm, chosen based around the particle diameter of 0.72 mm.

The porosity standard deviations used for each section size were 1%, 2%, 5%, 10%, 25% and 50% of the bulk porosity. This was based on an initial sensitivity study which revealed that higher degrees of variation resulted in unrealistically large pressure drops when compared to experimental results [45].

The porosity for the particulate filter was treated as uniform using parameters fitted to the Forchheimer equation (Eq. 5.1) as [45]:

$$(-\Delta\bar{p}/L) = 1.52 \times 10^9 \bar{u}_s + 6.41 \times 10^3 \bar{u}_s^2 \quad (8.1)$$

8.5 Grid independence

Two unstructured meshes were generated in order to conduct the grid independence analysis. Steady-state simulations at $Re_{inlet} = 1000$ were conducted with the intention of covering the range of porosity distributions considered here. The mean pressure drop, and spatially-averaged, and minimum values of mean residence time at the bed outlet were compared between the two separate meshes as listed in Table 8.1.

Table 8.1: Results of the mesh independence study

Mesh size: 1484111 cells				
Section size (mm)	Section standard deviation (%)	Mean pressure drop across canister (Pa)	Spatially-averaged value of the mean residence time 1 mm from carbon bed outlet (s)	Minimum value of mean residence time 1 mm from carbon bed outlet (s)
0.5	1	96.91	1.175	0.972
0.5	50	143.0	1.090	1.073
1	50	114.8	1.112	1.051
2	1	96.6	1.180	0.959
Mesh size: 884189 cells				
Section size (mm)		Mean pressure drop across canister (Pa)	Spatially-averaged value of the mean residence time 1 mm from carbon bed outlet (s)	Minimum value of mean residence time 1 mm from carbon bed outlet (s)
0.5	1	97.0	1.175	0.974
0.5	50	141.6	1.090	1.076
1	50	114.8	1.112	1.051
2	1	97.2	1.178	0.963

For each of the parameters observed, a difference of <1% was seen between meshes. On the basis of this analysis a mesh size of 884189 cells was used for the remainder of the study.

8.6 Validation

The domain studied here is identical to that used in Chapter 6 and was therefore validated using the same data. The numerical method used here was validated by comparison of the simulated data to previously obtained experimental data [45]. The baseline performance of the numerical method

used here was assessed by conducting simulations using both a constant, uniform porosity within the carbon bed and a longitudinally averaged porosity described by the Mueller equation. A comparison of simulation results to experimental results was made by means of the pressure drop across the canister, over a range of flow rates from an inlet Reynolds number of $Re_{in} = 1000$ to $Re_{in} = 8000$, which covers the complete range of normal human breathing rates from light to heavy workloads [37]. The experimental data was fitted to the Forchheimer equation in order to provide a continuous curve. The results of this analysis can be seen in Fig. 6.3.

It is clear from Fig. 6.3 the numerical method used gives a good representation of the experimental data, with only a slight deviation at very high flowrates.

8.7 Results and Discussion

8.7.1 Porosity distribution

The effects of changing section size and porosity standard deviation on the porosity profile of a cross section for four different cases are exemplarily shown in Fig. 8.2a.

The porosity profiles bear a superficial resemblance to the expected longitudinally averaged Mueller porosity profile. It is apparent that the section-based porosity model still predicts the expected areas of alternating high and low porosity close to the canister wall, particularly in cases with low values of porosity variation. This is more apparent in Fig. 8.2b in which beyond a short distance from the canister wall the value of porosity maintains an almost uniform distribution around its mean value.

Identifying the extent to which the porosity distribution affects the flow field within the canister and the canister performance is the key aim of this study.

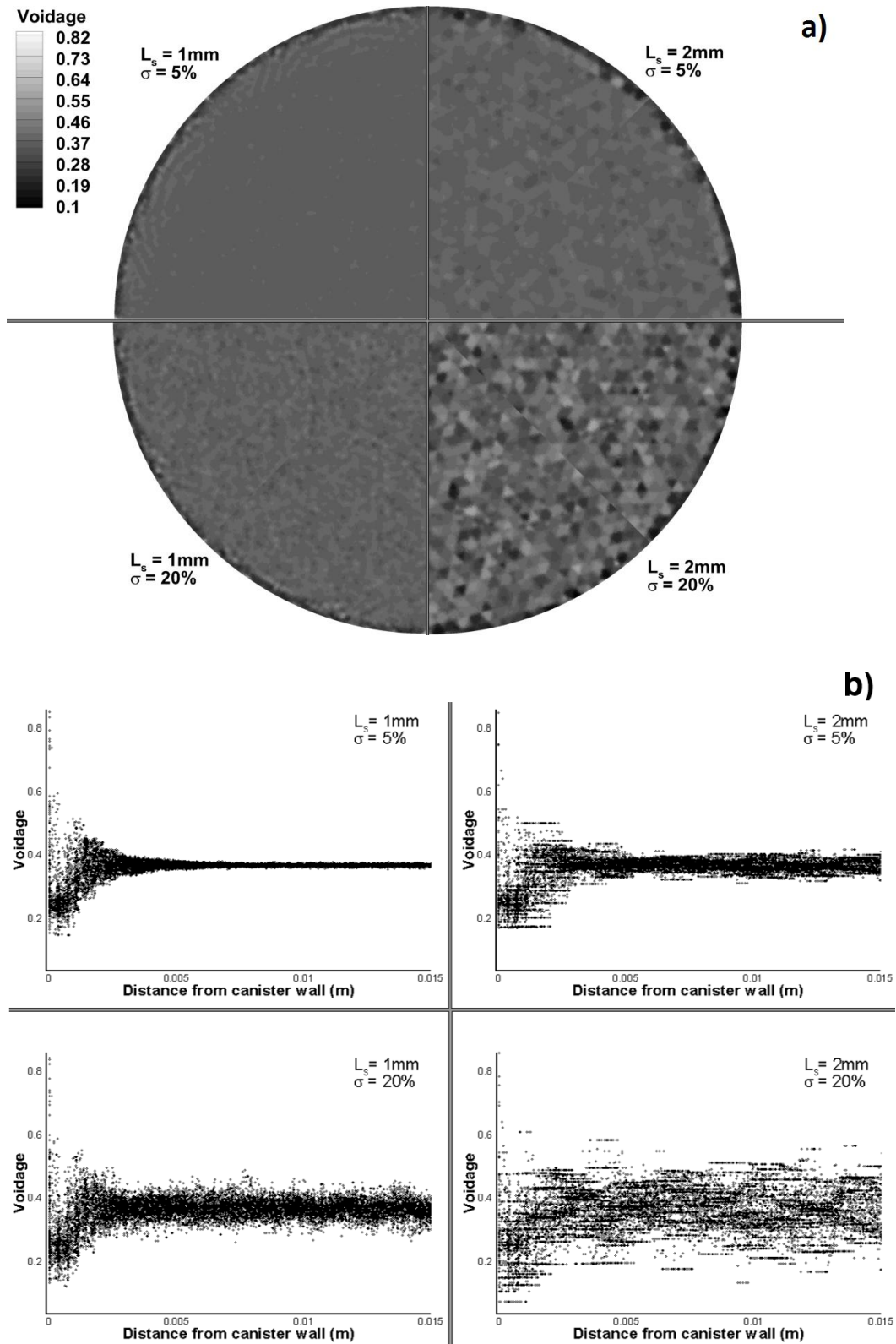


Figure 8.2:a) Voidage distribution of a cross section taken halfway through the length of the canister for two separate section sizes and b) the radial voidage profiles of these sections.

8.7.2 Model Appropriateness

As the porosity model used here was based upon the generation of random numbers, the appropriateness of the model was assessed. The ratio of section size to domain size has potential to significantly alter the results - excessively large sections would result in a porosity distribution which produced results which could not reliably be repeated. In order to have an appropriate pseudo-random model, it is necessary that use of the same parameters give the same results across separately seeded realisations. This was expected to primarily depend on the ratio of section size to bed size. To assess this, five realisations per parameter-set of select cases were carried out and the values and variance of key outputs compared. Cases were selected to best indicate the appropriateness of the model at the extreme cases of section size and porosity standard deviation.

The results of the appropriateness analysis are shown in Table 8.2.

Table 8.2: Mean results of key performance parameters and their standard deviations over five measurements for a range of section sizes and porosity variations.

Section size (mm)	Section standard deviation (%)	Pressure drop across canister (Pa)		Spatially-averaged value of mean residence time 1 mm from carbon bed outlet (s)		Minimum value of mean residence time 1 mm from carbon bed outlet (s)	
		μ	σ	μ	σ	μ	σ
0.5	1	97.0	0.15	1.175	0.0004	0.974	0.0006
0.5	50	141.6	0.77	1.09	0.0011	1.076	0.0008
0.72	1	97.2	0.29	1.174	0.0030	0.968	0.0045
0.72	50	121.0	0.67	1.095	0.00225	1.070	0.0009
1	1	97.5	0.27	1.175	0.0023	0.978	0.0019
1	50	114.8	0.36	1.112	0.012	1.051	0.0099
2	1	97.2	0.65	1.178	0.0057	0.963	0.0048
2	50	193.7	0.35	1.13	0.0242	0.998	0.034
5	1	95.5	5.29	1.01	0.0643	0.88	0.086
5	50	89.9	4.85	0.89	0.0851	0.81	0.12

For cases using 0.5 mm, 0.72 mm and 1 mm, the variation between separate realisations of the same case remained extremely low regardless of the porosity standard deviation for each of the output parameters assessed. For 2 mm sections the variation between realisations became somewhat more noticeable but remained small relative to the absolute values. When the section size was increased to 5 mm a steep increase in variation between individual cases was seen, indicating that the section

size to bed size ratio was too great for accurate results to be gained using this method. The 5 mm section size model was therefore rejected for the remainder of the study.

8.3.3 Pressure drop

The impact of increasing the porosity variation over the length of the canister can be seen in Fig. 8.3. For each of the section sizes considered below 2 mm there was a narrow range of values over which pressure drop remained constant, followed by a clear trend of increasing pressure drop with increasing porosity variation.

An explanation of this behaviour may be seen by considering the cross-sectional velocity distributions exemplarily shown in Fig. 8.4. An increase in porosity variation with constant section size results in a clear increase in the variations of velocity magnitude, with regions of high and low velocity seen throughout the bed. An inspection of Eq. 5.1 shows that this will result in a change in the nature of the losses seen throughout the bed; viscous losses will increase linearly with increased mean velocity, whereas inertial losses increase quadratically with an increase in mean velocity. Therefore an increase in velocity by some amount will have a larger impact than an equivalent decrease in velocity.

For cases with a section size of 2 mm the opposite trend was shown. At low values of porosity variation, similar pressure drops are seen as for small section sizes. However, as the variation is increased the pressure drop decreases. Fig. 8.5, which shows the velocity magnitude of a vertical cross section of the carbon bed provides some insight as to the origins of this discrepancy. At low porosity variations, the 2 mm section size appears similar to that seen with smaller section sizes. When the porosity variation is large, some long connected regions of high porosity begin to form, significantly altering the flow field by providing routes of low flow resistance.

8.3.4 Residence time

The residence time of air leaving the bed is assessed by the mean air age transport equation. The mean age of air averaged over the whole cross section and the minimum mean air age in that cross section were both taken as indicators of canister behaviour, as seen in Fig. 8.3.

In general, for cases of 1 mm, 0.72 mm and 0.5 mm, it was seen that an increase in porosity variation would result in a reduction in the average age of air leaving the carbon bed. In contrast to this, the minimum value of mean residence time of air leaving the bed was shown to increase with increasing porosity variation.

As seen in Figs. 8.4 and 8.5, a higher degree of porosity variation results in a greater variation in velocity throughout the bed. As seen in Eq. 2.9, velocity gradients are associated with a corresponding increase in the generation of turbulent kinetic energy.

An inspection of an iso-surface of arbitrarily selected mean-age reveals that in the case of an increased porosity variation, a flatter overall profile of mean air age can be seen from Fig. 8.6, which is a result of the increased rate of generation of turbulent kinetic energy. This flatter overall profile leads to a reduction in flow-channelling both as a result of the canister geometry and due to the longitudinally averaged porosity profile.

Cases using a section size of 2 mm showed the reverse trend to those with a smaller section size. As with the pressure drop, this is likely due to the formation of some large regions of high and low porosity forming throughout the bed, significantly modifying the resultant flow field as flow is channelled through more porous regions.

Assuming that the behaviour seen for smaller particle sizes is more indicative of the true physical behaviour of flow in packed beds, it is likely that numerical simulations conducted using a longitudinally-averaged representation of porosity will tend to over-predict the average residence time of air leaving the bed, while under-predicting the minimum value of the mean residence time.

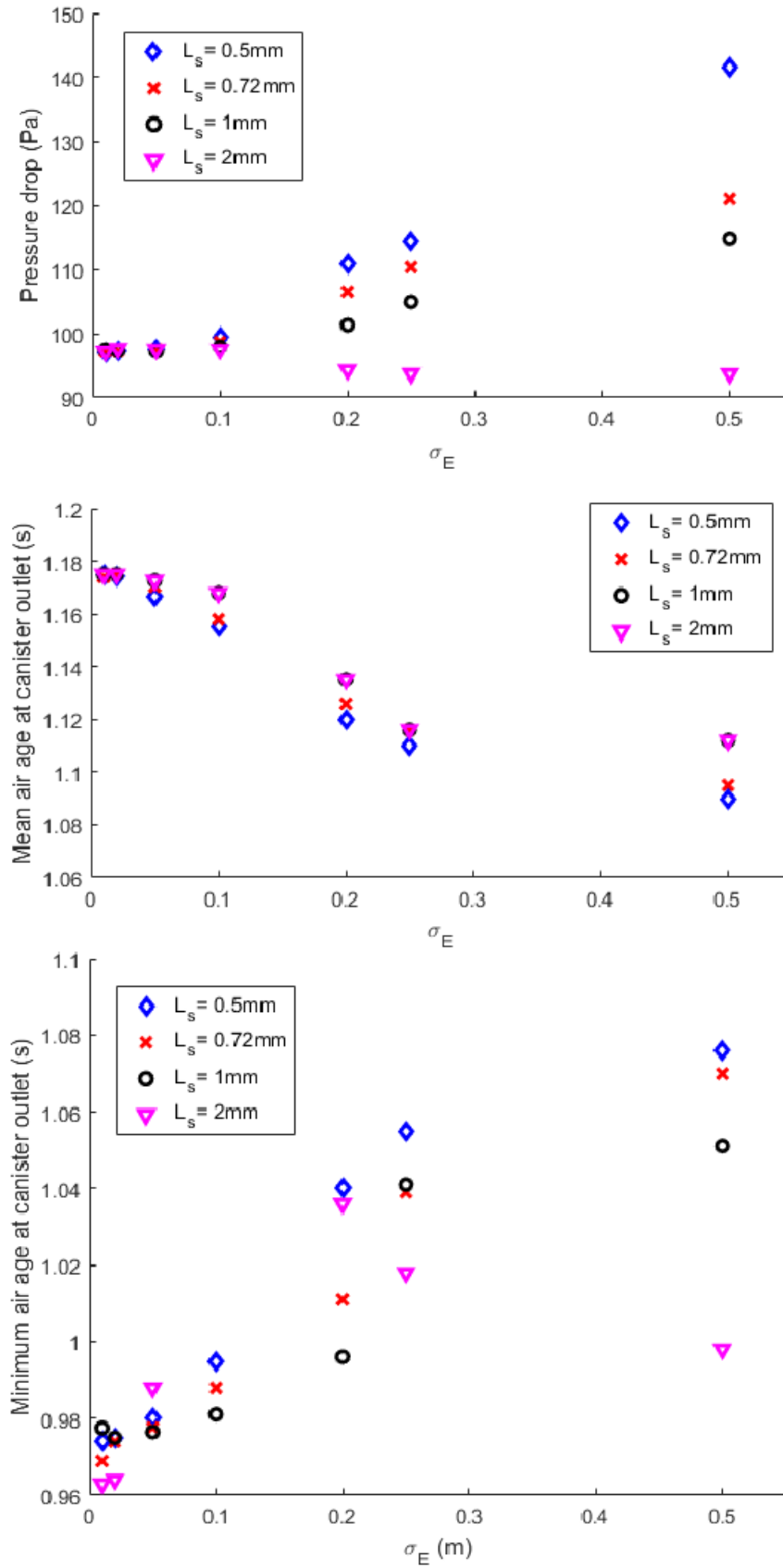


Figure 8.3: Profiles of pressure drop across the canister, average mean air age at a cross section at the carbon bed outlet, and the minimum value of the mean air age seen there.

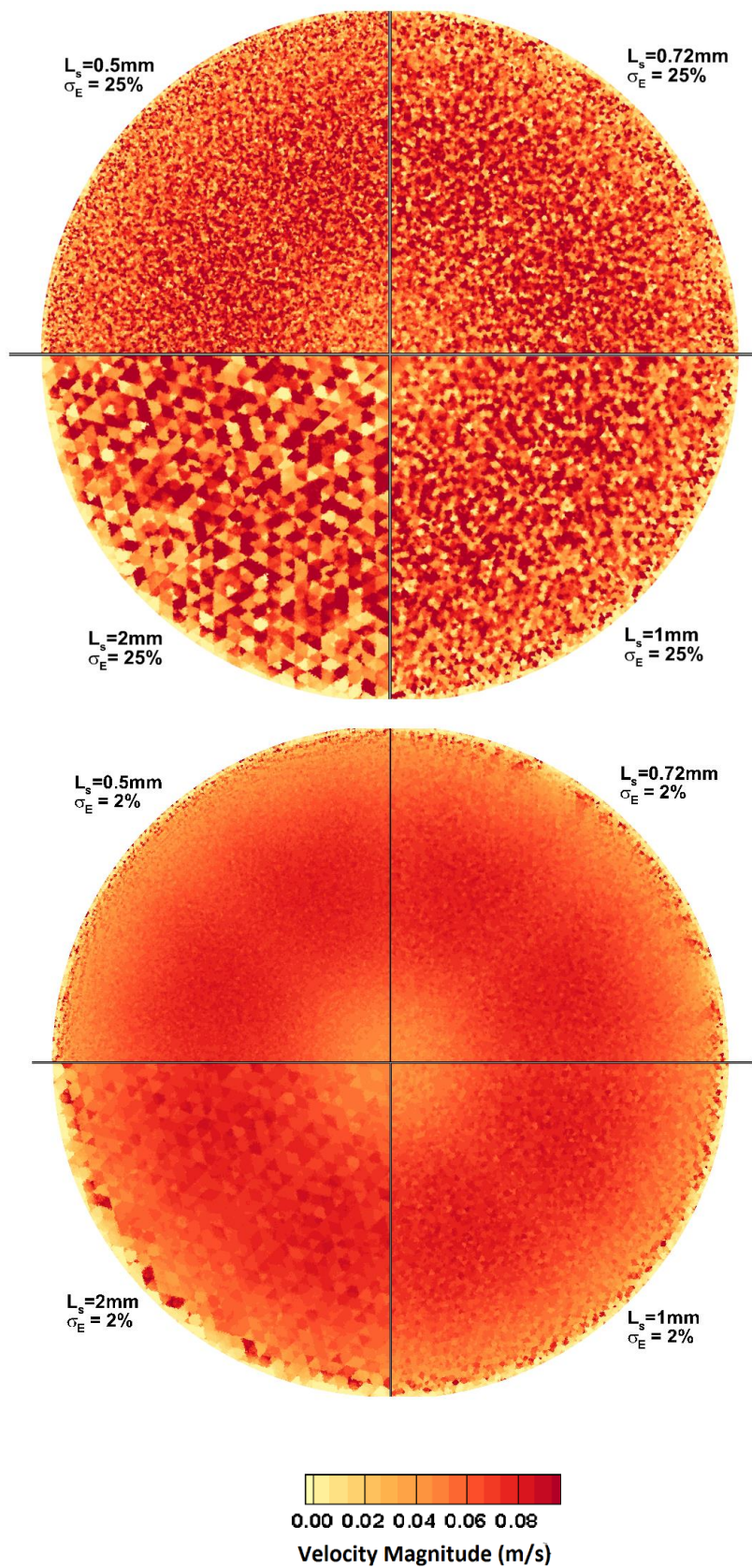


Figure 8.4: Velocity magnitude distribution 10 mm from the outlet of the carbon bed for $\sigma_E = 2\%$ and $\sigma_E = 25\%$ for a range of section sizes

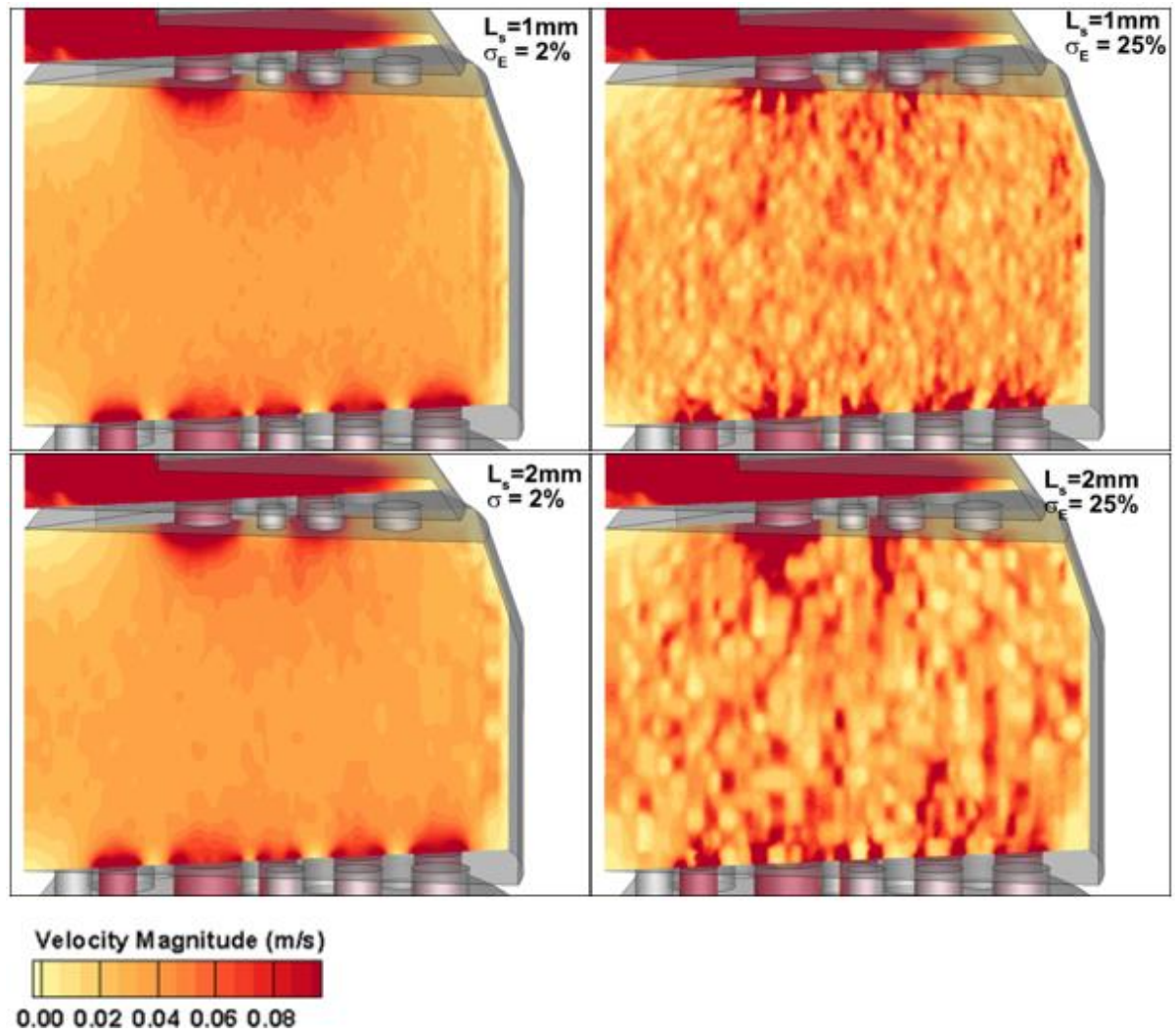


Figure 8.5: Representative velocity magnitude distributions of a vertical bed cross section.

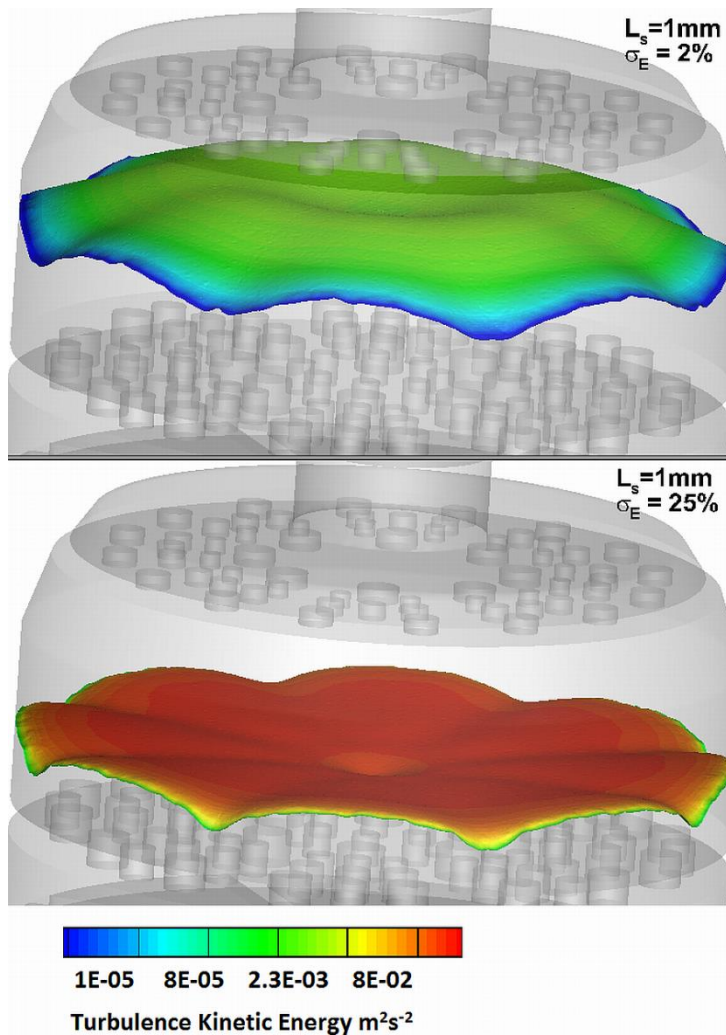


Figure 8.6: Iso-surfaces of a mean air age of 0.7 s coloured by the local turbulent kinetic energy.

8.3.5 Relationship between σ_E and L_s

It is expected that a relationship should exist between the section size and the porosity variation. It is clear from the previous results that while similar trends for pressure drop and residence time distribution were seen for cases of 0.5 mm, 0.72 mm and 1 mm section sizes, the exact results depended on the section size. For a real bed, sampling of the bed shows that the standard deviation of the bed should approach zero as the sample size is increased [97]. The ratio of L_s/σ_E was therefore compared to the numerical results for each of the key parameters, as shown in Fig. 8.7. The results for section sizes of 2 mm were left out of this analysis, due to the inconsistencies with the general trends seen previously.

It is clear from Fig. 8.7 that, over the narrow range of section sizes used here, performance of the pseudo-random porosity model might be dictated by a single parameter, L_S/σ_E . This suggests there is some scope for reducing the number of experimental degrees of freedom required to develop future section-based models. For example, if a section size close to the particle diameter is selected arbitrarily, the porosity standard deviation may be assigned based only on an experimental measurement of pressure drop, leaving any additional experimental output available for validation of the numerical model.

8.3.6 Canister performance at higher flowrates

A limited selection of the cases seen here were also investigated at inlet Reynolds numbers of $Re_{in} = 2000$ and $Re_{in} = 5000$ in order to analyse if the previously observed relationship between section length and porosity variation would remain over the range of flow rates expected to be seen under normal canister usage.

Values of section size and porosity variation were selected on the basis of including each of the three section sizes while still covering a wide range of values of L_S/σ_E . Results in terms of pressure drop and residence time as seen previously were taken.

It is apparent from Fig. 8.8 that the general relation between L_S/σ_E seen at $Re_{in} = 1000$ can also be seen for higher flow rates.

8.7 Results and Discussion

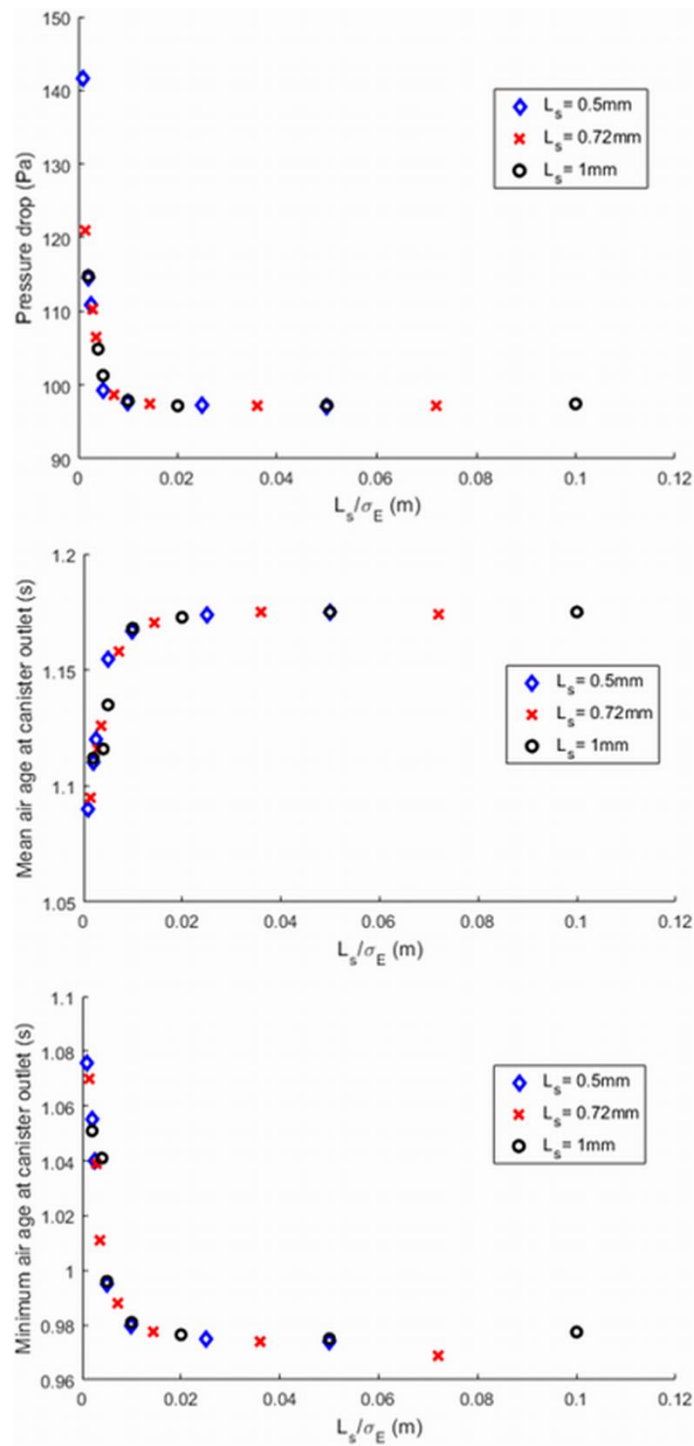


Figure 8.7: Profiles of pressure drop across the canister, average mean air age at a cross section at the carbon bed outlet, and the minimum value of the mean air age seen there, against ratio of section size to standard deviation.

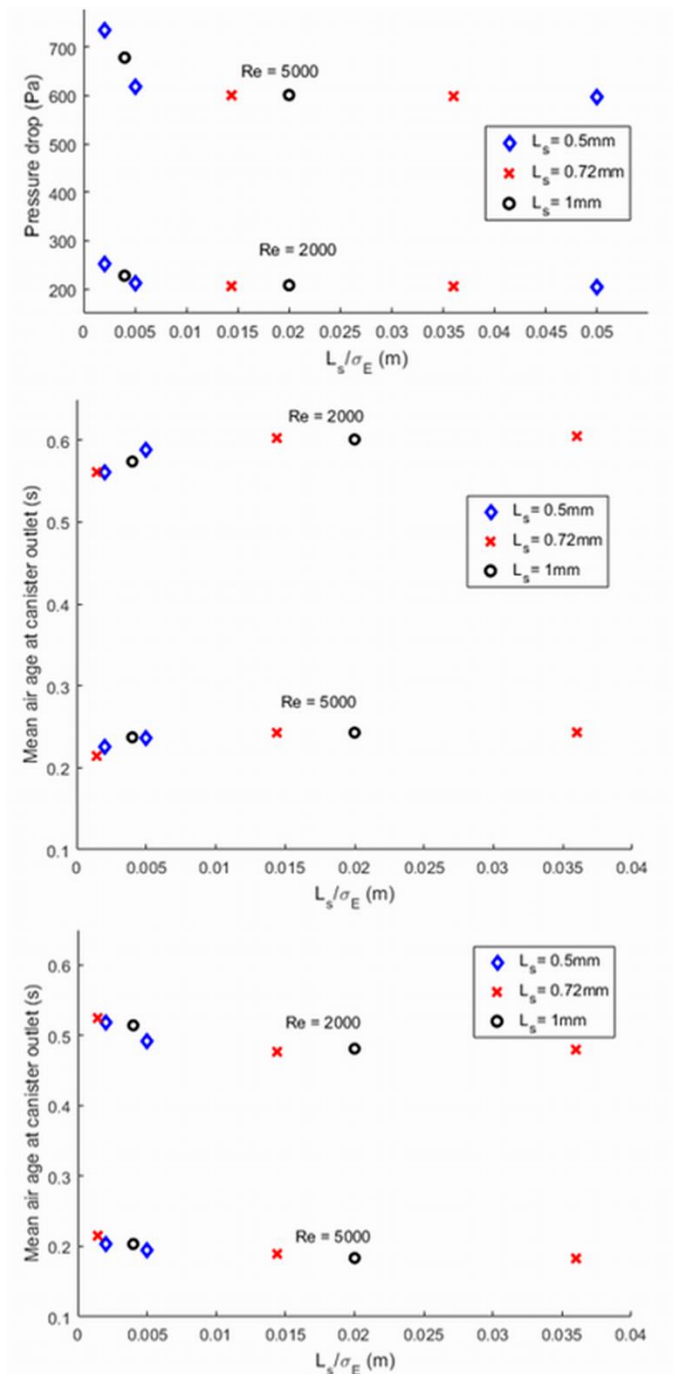


Figure 8.8: Profiles of pressure drop across the canister, average mean air age at a cross section at the carbon bed outlet, and the minimum value of the mean air age seen there, against ratio of section size to standard deviation for select cases at high flow rates.

8.5 Key Findings

A new model has been developed to represent the stochastic nature of a porous bed of packed activated carbon particles within a CBRN respirator canister. The bed was represented as a continuous porous medium which is subdivided into discrete sections. Within each section a

baseline local porosity was assigned based on its radial position according to the longitudinally averaged Mueller equation. The section porosity was then perturbed according to a Gaussian distribution. This resulted in a porosity distribution, which accounted for longitudinal variations in porosity while still showing the correct radial distribution when averaged longitudinally. For a given particle size and bulk porosity, the model is therefore defined by two parameters: the section dimension and the porosity standard deviation. The aim of this study was to assess the impact that these parameters would have on canister performance based on the pressure drop across the canister, and the spatially-averaged and minimum values of the mean residence time seen at the canister outlet. All initial cases were conducted at an inlet Reynolds number of $Re_{in} = 1000$.

Model appropriateness was assessed by comparing separately seeded realisations of the model with the same parameters, and it was shown that for cases of 1 mm and below the domain was large enough relative to the section size that separate realisations with the same parameters would produce very similar results. For cases with a 2 mm section size the variation became more noticeable, and at 5 mm the degree of variation between individual realisations became extremely large. Cases with a section size smaller than 5 mm also gave a good depiction of the expected longitudinally averaged porosity profile.

Although it was desirable to study the effects of a wider range of section sizes, the range of sections investigated was limited by the domain size and the size of the computational grid required.

In general, it was seen that for section sizes of 1 mm and below, an increase in porosity variation above some threshold would result in an increase in pressure drop over the length of the canister. This was attributed to an increase in inertial flow resistance caused by areas of higher velocity related to areas of high local porosity, which was greater than the corresponding reduced flow resistance in areas of low velocity flow, as the inertial losses scale quadratically with mean velocity. The spatially-averaged and minimum values of mean residence times seen at the outlet of the carbon bed were used as indicators as to the adsorption potential of the bed. For section sizes below 2 mm, an increase in porosity variation resulted in a decrease in the averaged value of the

mean air age seen at the outlet of the bed, but an increase in the minimum value of the mean air age. This could be explained by large velocity gradients throughout the bed due to the varying porosity, which resulted in an increased generation of turbulent kinetic energy and an overall flatter residence time distribution. It is therefore expected that numerical models which rely only upon the longitudinally averaged porosity distribution without consideration to porosity variations will tend to under-predict pressure drop and the minimum value of mean residence time, while over-predicting the mean residence time of air leaving the canister.

Variation between separately seeded realisations did not alone give an adequate assessment of model appropriateness. For each of the key parameters monitored, it was shown that cases using 2 mm sections with higher porosity variations would produce good agreements between separate realisations. However, the 2 mm cases generally showed the reverse trends to cases with smaller section sizes. This was due to a high degree of flow channelling through about connected regions of similar porosity, which was likely an unrealistic depiction of the true physical situation.

For cases of section sizes 0.5 mm, 0.72 mm and 1 mm, it was seen that results for pressure drop, spatially-averaged and minimum values of mean air age at the outlet all depended on the ratio L_s/σ_E , rather than the parameters individually, which significantly reduces the amount of experimental data needed for developing and validating an appropriate section based model.

A limited number of cases were conducted at higher inlet flow rates of $Re_{in} = 2000$ and $Re_{in} = 5000$ for section sizes 0.5 mm, 0.72 mm and 1 mm, and were shown to give similar trends to those at $Re_{in} = 1000$.

Chapter 9

Modelling Adsorption and Residence Time in

Porous Beds

Mean air age has been extensively used in the past as a tool to provide an indication of adsorption and breakthrough performance without the need for detailed and time-consuming adsorption modelling. In this chapter axisymmetric simulations have been carried out on a cylindrical domain with a central inlet that introduce a contaminant into an adsorbent bed using different flow rates and porosity models in order to gain a better understanding of the relationship between mean air age and adsorption characteristics.

9.1 Background

Adsorbent beds are commonly used for the cleaning of effluent streams in a wide range of industries. Usually a contaminated inlet stream is passed entirely through a packed bed of a suitable adsorbent, where the contaminant is adsorbed and the resultant outlet stream will have a contaminant concentration below some threshold value. Over time, adsorption sites within the bed will become occupied and the capacity of the bed to sufficiently adsorb from the stream will become compromised; eventually this will result in the outlet stream containing contaminant above the threshold concentration. At this point breakthrough is deemed to have occurred and the bed has failed [130]. It is extremely useful to understand the time taken to failure, and the process by which it occurs.

For large cylindrical beds, a mass balance of contaminant entering the bed can be used to give an estimate of the time taken for breakthrough to occur. If the bed is considered to have failed when the outlet concentration crosses a threshold C_{out} then the time to failure t_b can be estimated as [131]:

$$t_b = \frac{\rho_B W_e}{C_{in} V_L} \left[L_B - \frac{V_L}{k_{WJ}} \ln \left(\frac{C_{in}}{C_{out}} \right) \right] \quad (9.1)$$

where ρ_B is the bed bulk density, L_B the bed length, V_L the inlet flow rate and k_{WJ} the overall kinetic constant. The Wheeler-Jonas equation is predicated upon the assumption that the contaminant will immediately spread some distance into the bed forming a characteristic front shape, and this front will then advance through the bed unchanging. The shape of the front will be affected by the porosity distribution and adsorption kinetics [78].

There are a large number of cases in which the Wheeler Jonas equation will not be accurate. Many beds will not have a perfectly cylindrical geometry, or may feature brackets, baffles or other features which will alter the shape of the adsorption front over time. The inlet flow rate or contaminant concentration may vary over time. Even in cylindrical beds under constant flow conditions the extent to which the front shape remains constant may vary on a case by case basis [79, 80]. A particularly widespread case of adsorbent beds falling outside of the range of applicability of Eq. 9.1 are respirator canisters, in which the inlet may be more centrally located, rather than extending over the whole diameter of the bed [82].

It is therefore useful to be able to predict performance of adsorbent beds under a broader range of circumstances than those which conform to Eq. 9.1. The use of CFD has become widespread for this purpose, as it provides a relatively inexpensive method of predicting the flow field through an adsorbent bed, and the resultant bed performance characteristics such as pressure drop or adsorption behaviour [45-47, 117, 130, 132].

One limitation of CFD for adsorption beds is that detailed adsorption modelling is highly time consuming and computationally expensive, as it requires the solution of species and energy conservation equations over many time steps. One alternative to adsorption modelling is the use of residence time distribution to give an indication of adsorbent bed performance. Predicting the residence time distribution requires only the solution of a single additional passive scalar equation, the mean air age equation [44]. It is thought that the residence time distribution will give a good indication of adsorption performance by highlighting dead zones and areas where rapid breakthrough will be seen; although each contaminant will have different exact adsorption

9.2 Domain and Boundary Conditions

performance it is expected there should be some generality with regard to these features. However there is comparatively little literature directly relating residence time and adsorption performance.

In this study adsorption of an activated carbon bed with a centred inlet has been simulated using CFD. The distribution of contaminant throughout the bed over time has been compared to the residence time distribution to assess the extent to which residence time can be used as a proxy for adsorption performance within CFD simulations of such configurations. The simulations are repeated with three different porosity models over two different inlet flowrates and are validated against experimental data.

9.2 Domain and Boundary Conditions

The simulation domain was an axisymmetric bed of 86.5mm diameter and depth, with a 20mm inlet located centrally on the left-hand side and the outlet taking up the whole right-hand side, representative of a typical CBRN canister configuration as shown in Fig. 9.1. The walls obeyed the no slip condition and were impenetrable. At the outlet, the Neumann boundary condition was obeyed (ie. no change in primitive variables in the direction normal to the outlet). Inlet turbulence boundary conditions were found by a sensitivity analysis; a turbulence intensity $I = \sqrt{2k/3}/U = 10\%$ and a turbulence length scale $l_t = 0.07d_{in}$ were chosen based on this. Simulations were conducted with inlet velocities of 10m/s and 20 m/s.

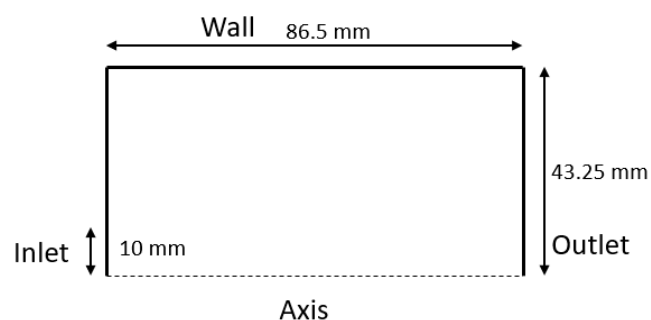


Figure 9.1: Configuration of the geometry studied for this investigation.

A steady-state solution with no inlet contaminant was found before the contaminant was introduced. The test contaminant was chosen to be cyclohexane, which is widely used as a test contaminant to

for analysing volatile organic compounds for respirator canisters[8]. It was introduced at a continuous inlet volume fraction of 2%. The relevant properties of cyclohexane are listed in Table 9.1.

The bed was packed with activated carbon of a particle diameter of 1 mm. The viscous and inertial losses for the momentum equation were calculated according to the Ergun equation (Eq. 5.1) on the basis of local porosity. Three different approaches were used to describe the distribution of porosity throughout the bed:

- Constant porosity throughout the bed.
- Porosity described solely based on radial distance from the wall on the basis of the Mueller equation (Eq. 3.10).
- A section-based porosity model, in which the bed is subdivided into discrete sections of fixed size. The sections are then allocated a local porosity based on the Muller equation for the radial distance from the wall of their centre. This porosity is then randomly perturbed according to a Gaussian distribution with a standard deviation of 5%.

Each porosity distribution is simulated at each flow rate. The full range of cases simulated is listed in Table 9.1.

The length of time steps used for all cases was based on a sensitivity analysis, increasing from 0.0001 s at the moment the contaminant was first introduced to a maximum of 0.0024 s.

Table 9.1: Material properties of cyclohexane and activated carbon used in this study

Cyclohexane Molecular Weight (kmol/kg)	84.17
Cyclohexane Diffusion Coefficient in air [119] (m^2/s)	7.84×10^{-6}
Heat of adsorption (kJ/kmol)*	18945.5
Micropore volume (cm^3 micropore/g carbon)*	0.324
Effective mass transfer coefficient (s^{-1}) [120, 121]	0.004
Bulk porosity (-)	0.365
Bulk Density (kg/m^3)	550
Mean particle diameter (m)	0.001

9.3 Validation

Table 9.2: The range of cases investigated in the study

Case	Inlet velocity (m/s)	Porosity Model
I	10	Longitudinally-averaged Mueller equation
II	20	Longitudinally-averaged Mueller equation
III	10	Section based
IV	20	Section based

9.3 Validation

Validation was provided by comparison of the numerical model to experimental data. Experimental data has previously been gathered for the breakthrough of cyclohexane on an activated carbon bed. The beds were cylindrical with a diameter of 86.5 mm, with the whole diameter of the bed serving as the inlet, and a depth of 15 mm. The beds were packed with activated carbon using the “snowstorm method” to maximise packing density [109] with particles of 1 mm in diameter and a nominal density of 550 kg/m³. Inlet flowrates of 15, 30 and 50 L/min were used, each with an inlet contaminant concentration of 2000 ppm. The maximum cyclohexane concentration seen at the outlet over time was then measured for each of these.

The method used for this study was then used to simulate each of these experimental cases, using each of the porosity models studied here, and for uniform porosity. The numerical method was then compared to the experimental data by means of the breakthrough time; the time taken until a cyclohexane concentration of 10 ppm could be seen in the outlet stream.

As can be seen in Table 9.3, both the constant porosity and section-based models give a good indication of the experimental breakthrough time. The longitudinally-averaged Mueller model significantly under-predicts the adsorption time.

Table 9.3: Results of the validation study

Flow rate (L/min)	Inlet velocity (m/s)	Breakthrough times (s)			
		Experimental	CFD – Constant porosity	CFD – Mueller equation	CFD – Section based model
15	0.0425	5208	5010	4846	4981
30	0.0851	2688	2631	2010	2595
50	0.1418	1407	1440	848	1381

9.4 Results

A measure of bed performance may be taken by assessing the depth at which contaminant over a threshold concentration can be seen into the bed over time. For this a contaminant threshold of 10 ppm is used, based on NIOSH standards for CBRN respirators. The furthest point into the bed in the axial direction where the contaminant threshold was crossed has been measured over time, and is shown in Fig. 9.2.

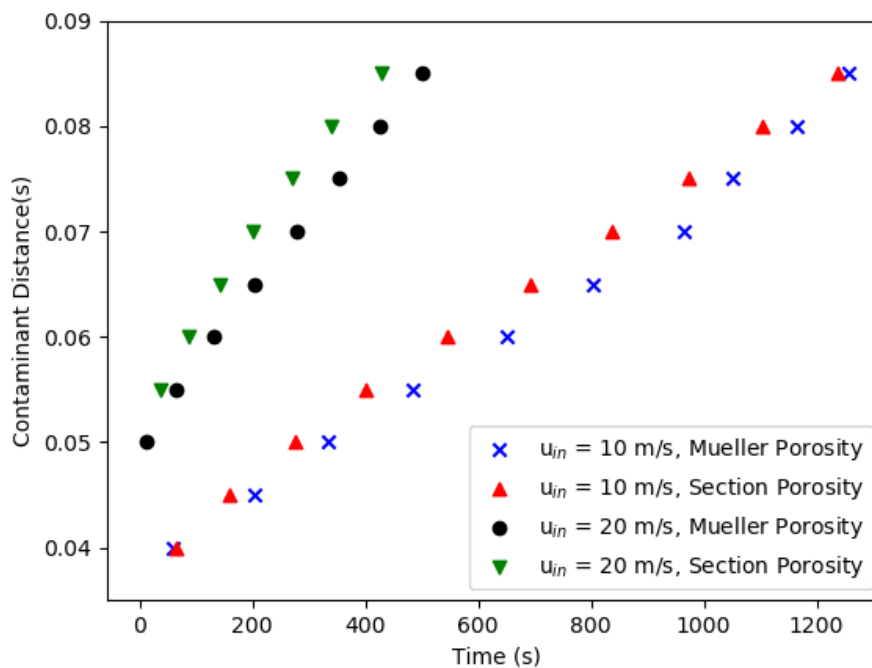


Figure 9.2: The axial distance penetrated into the bed over time for each case investigated here.

Similarly to the analysis seen in Chapter 7, the breakthrough performance for each of these cases may be compared to the Wheeler-Jonas equation (Eq. 3.8). There is a near-instantaneous penetration some depth into the bed, which is higher for faster flow rates, and is unaffected by choice of porosity model seen here. As discussed in Chapter 7, this distance is heavily influenced by the adsorption kinetics. Following this there is a steady progression of the contaminated front through the bed. Under the Wheeler-Jonas equation, this rate at which this front moves in the axial direction is constant. However, under the conditions used here there is a slight deviation away from the expected Wheeler-Jonas behaviour over the duration of the simulation, which is more prominent in the higher flow rate cases. This may be accounted for by two factors as demonstrated by the axial

9.4 Results

velocity profiles seen in Fig. 9.3. Firstly, the contaminant initially disperses away from the centred inlet, in a manner inconsistent with the unchanging front shape assumed by the Wheeler-Jonas equation. Additionally, the variation in velocity in the near-wall region caused by the alternating of areas of high and low porosity will have some effect on the dispersion of contaminant when it reaches the near-wall region.

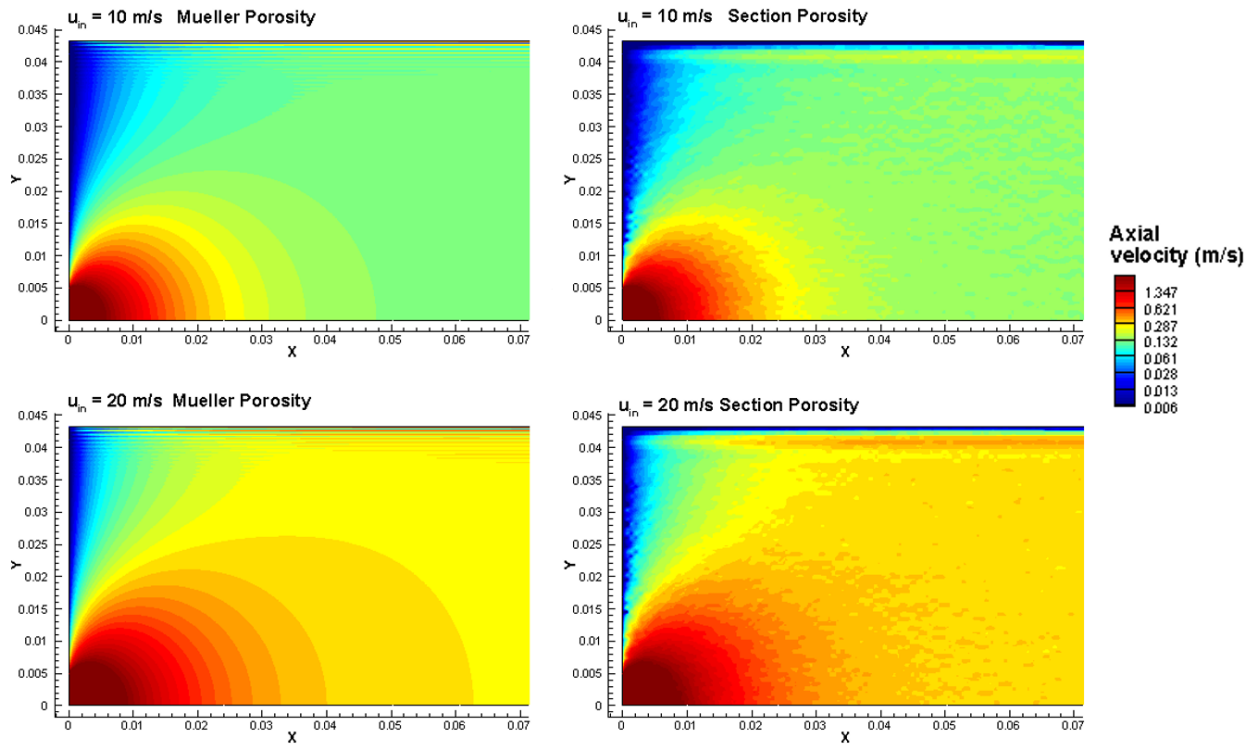


Figure 9.3: Axial velocity profiles for each of the cases considered here.

A qualitative analysis of the relationship between residence time and adsorption performance can be seen by observing a contour profile of mean air age as seen in Fig 9.4. This may then be overlaid against contours of vapor-phase cyclohexane at fixed points in time after exposure. This is exemplarily shown for a period 30 s after exposure in Fig. 9.5 and for 200 s after exposure in Fig. 9.5.

It is clear from Figures 9.4 and 9.5 that there is a good qualitative relationship between the shape of the contamination front and the shape of the residence time profile, and that this remains true over a wide range of times after contamination. This implies there is good scope for using mean air age distribution as a rough predictor for distribution of contaminant.

The main discrepancy between the mean air age and adsorption contour profiles occurs early after exposure; this is because the initial period of rapid adsorption when contamination first occurs operating on a drastically different time scale, which will not be reflected in the residence time distribution.

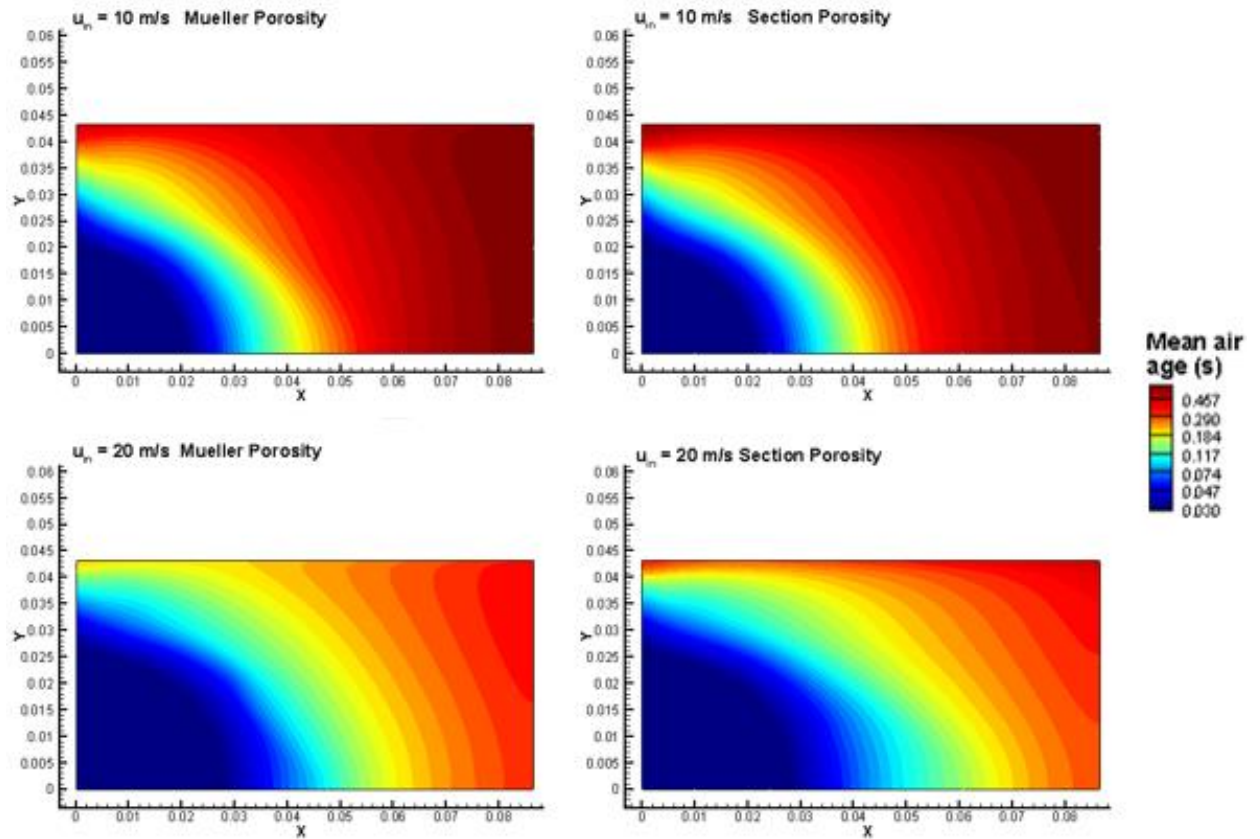


Figure 9.4: Contours of mean air age for each case investigated here.

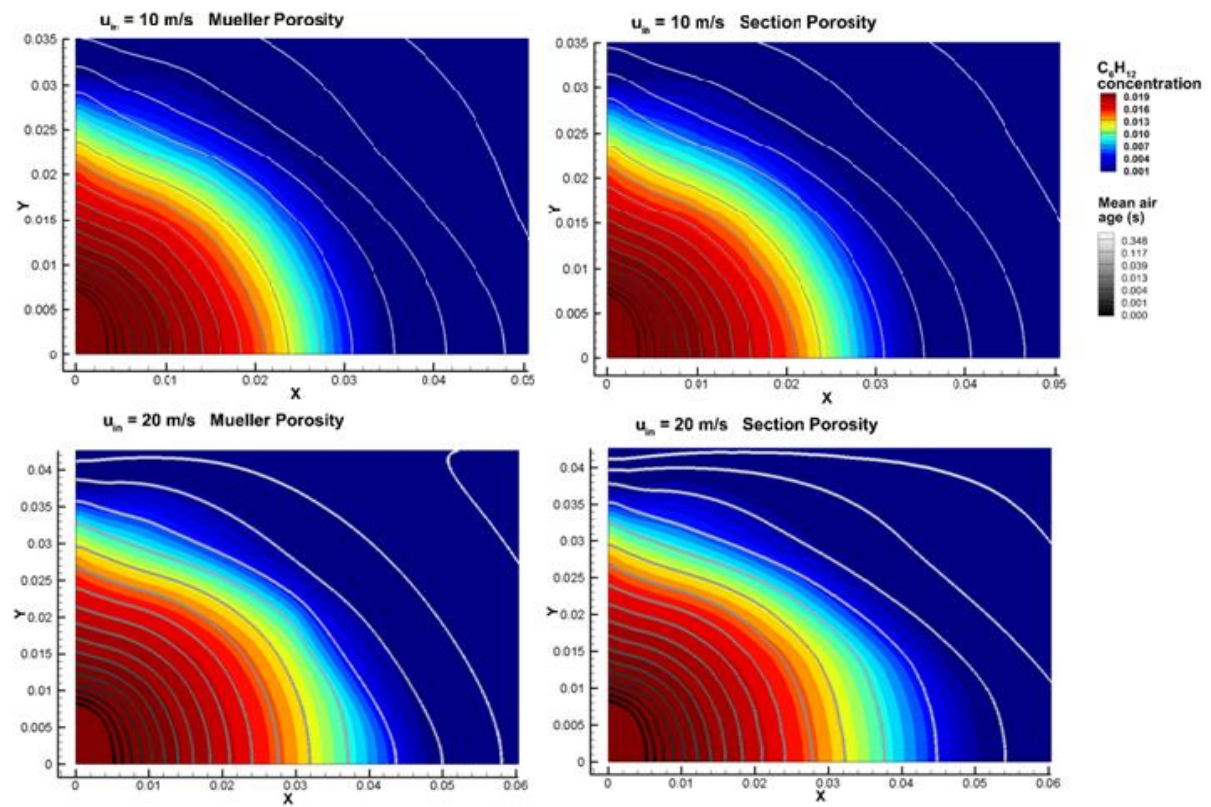


Figure 9.5: The distribution of contaminant close to the inlet after 30 s, overlaid with contours of mean air age for the two different porosity models and two different inlet flow rates investigated here.

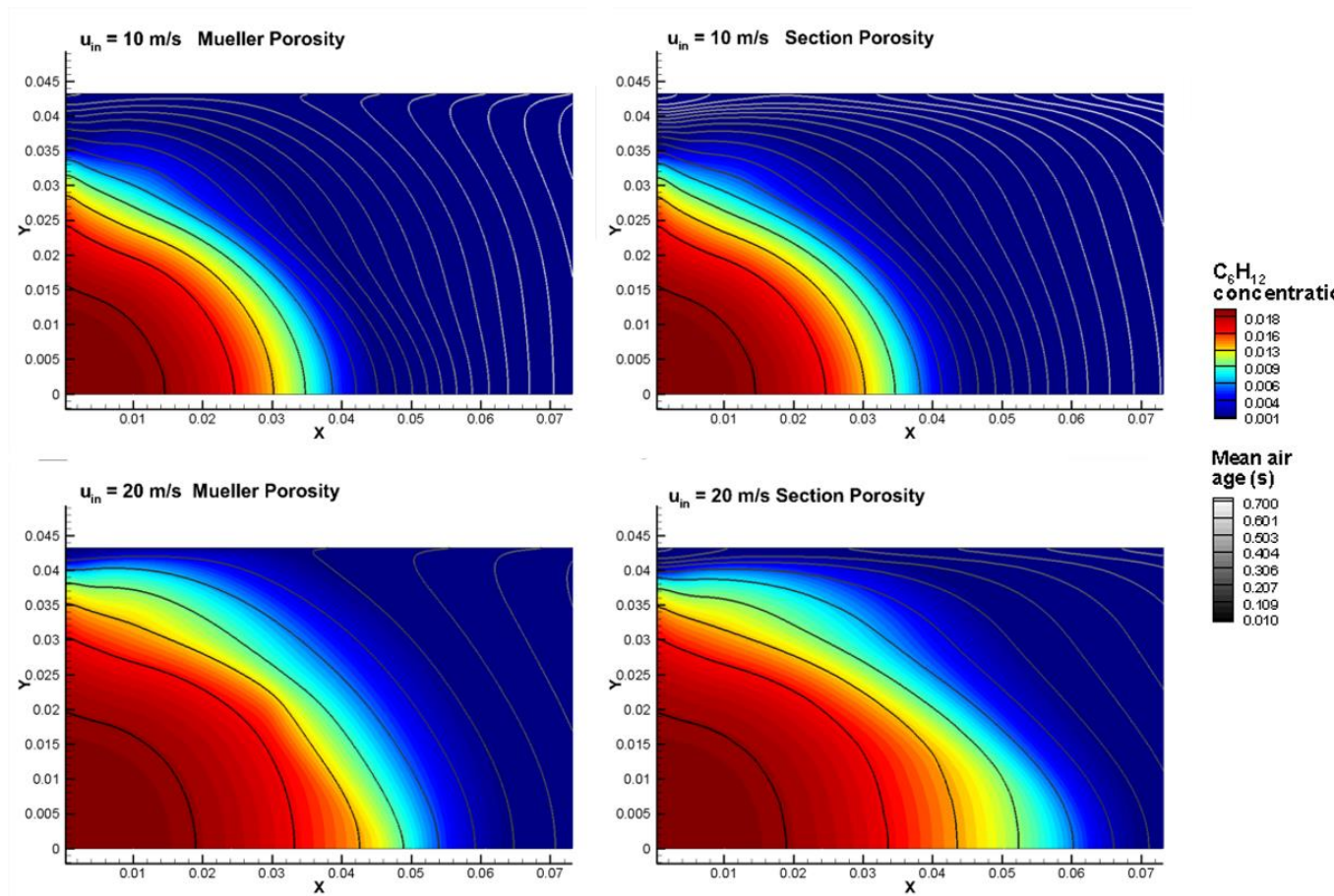


Figure 9.6: The distribution of contaminant close to the inlet after 200 s, overlaid with contours of mean air age, for the two different porosity models and two different inlet flow rates investigated here.

The relationship between adsorption behaviour and residence time distribution can be assessed by comparing the time taken for the bed to fail – defined as a concentration of cyclohexane greater than 10 ppm being detectable at the outlet – to the average mean air age at the outlet and the minimum mean air age at the outlet for each of the cases investigated here.

Table 9.4: Breakthrough time, minimum and average mean air ages at the outlet and the ratio of these.

Inlet velocity (m/s)	Porosity profile	Breakthrough time (s)	Average mean air age at outlet (s)	Breakthrough time: average mean air age ratio	Minimum mean air age at outlet (s)	Breakthrough time: minimum mean air age ratio
10	Mueller	1258	0.6684	1882.1	0.6277	2004.1
20	Mueller	501	0.3336	1501.8	0.3035	1650.7
10	Section-based	1236	0.6728	1837.1	0.6027	2050.8
20	Section-based	429	0.3363	1275.6	0.2770	1548.7

The ratio of breakthrough time to the average mean air age and the minimum mean air age has been compared for each case. In general for both ratios a fairly wide variance between the different cases can be seen. Although the number of cases seen here is small, this suggests that a simple inspection of average mean air age or minimum air age at the outlet will not be sufficient to predict breakthrough times between cases.

It is also useful to see the relationship between contamination and residence time over the lifetime of the bed. The time after initial exposure at which contamination above a threshold value can be seen has been recorded for every location within the carbon bed. In order to observe the extent to which mean air age can be used as an indicator for adsorption performance, the local time of first contamination has been plotted as a function of the local residence time for the entire domain for each of the cases investigated here, as seen in Fig. 9.7. Note that although the data is technically discrete due to the discrete nature of the computational mesh, it has been presented as the range of contamination times due to the extremely large number of data points. The area-weighted average of these has also been included.

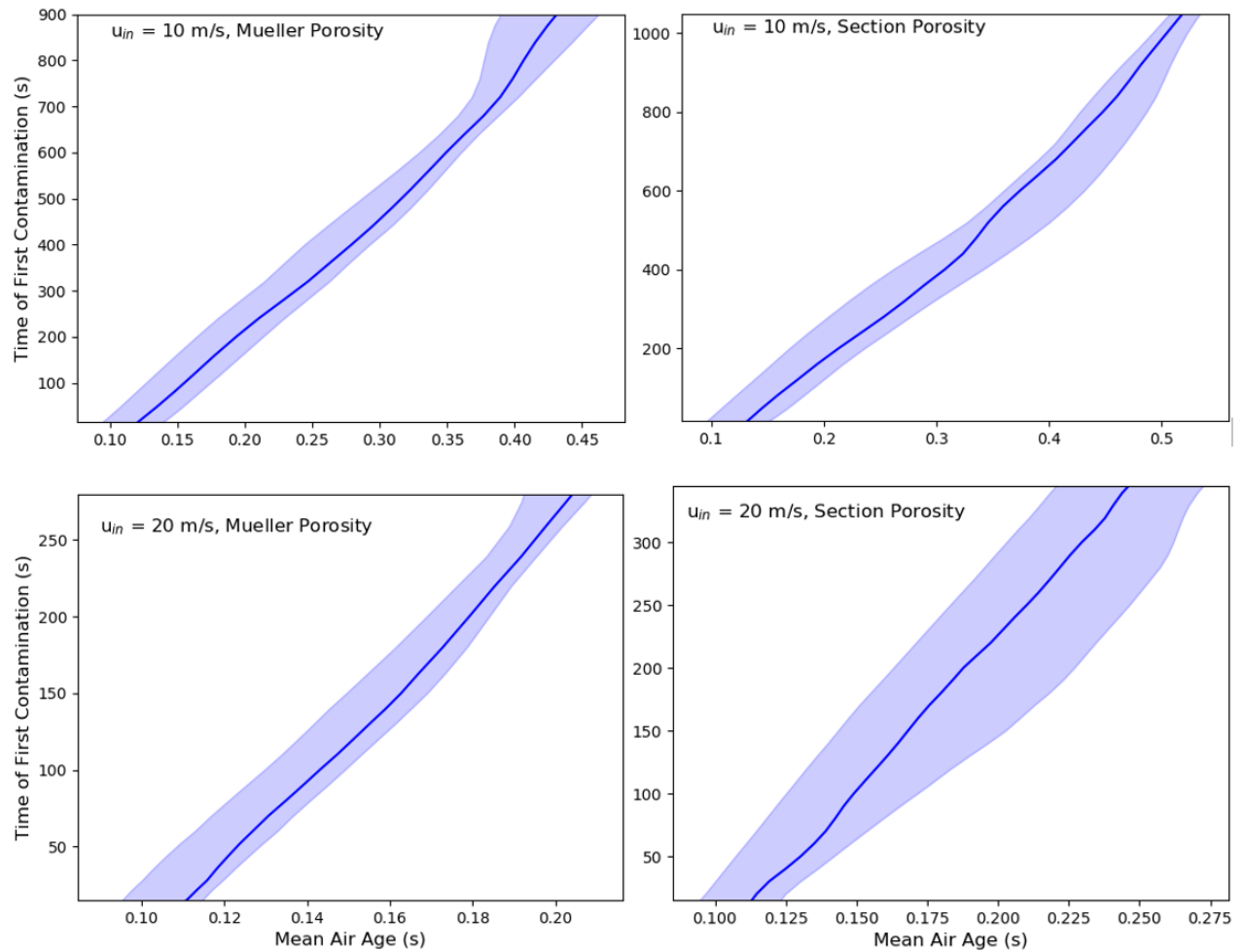


Figure 9.7: Time at which each area within the bed is first contaminated seen against local mean air age for each case.

It is clear that the local mean air age does not provide a simple predictor for the time at which a region will first become contaminated; a single mean air age may be associated with a wide range of contamination times, which depends on inlet velocity and porosity model, and varies considerably over the range of mean air ages seen for each case as the shape of the contaminated region develops over time.

For all cases that the upper and lower bounds of first contamination time increase with increasing local mean air age, although at varying rates. The average first contamination time shows a more consistent increase with increasing local mean air age and is closely correlated as demonstrated by the Pearson correlation coefficient seen in Table 9.5. This increase shows a good approximation of linear behaviour, and a linear regression coefficient (using a least-squares method) has been calculated for each case as shown in Table 9.5.

9.5 Key Findings

Table 9.5: Correlation coefficients and linear regression coefficients between local mean air age and the average time until contamination for each case.

Inlet velocity (m/s)	Porosity profile	Pearson correlation coefficient	Linear regression coefficient
10	Mueller	0.9957	2749
20	Mueller	0.9987	2779
10	Section-based	0.9958	2634
20	Section-based	0.9993	2477

There is a good degree of consistency between these coefficients, with a variation between the upper and lower values of only 12.1%. This suggests there may be some scope to use mean air age as a quantitative predictor of how long on average it will take for a region within a porous bed to become contaminated.

9.5 Key Findings

Axisymmetric RANS simulations of a cylindrical activated carbon bed with a centred inlet were carried out at two different inlet flow rates and using two different porosity models. A contaminant (cyclohexane) was introduced to the inlet stream and its adsorption onto the bed was modelled. The progress of the contaminant through the bed was compared to the distribution of mean air age throughout the bed (as recorded prior to the introduction of contaminant).

Due to time taken for the contaminant to spread from the inlet and the interaction between the wall and the area of oscillating porosity in the near wall region, the rate of axial spread of contaminant was seen to vary over the duration of the simulation, which was more prevalent for the cases with higher inlet flow rates.

A qualitative assessment of the relationship between mean air age and the spread of contamination could be seen by observing contours of each at different stages after contamination. It was seen that generally mean air age gave a fairly good representation of the shape of the contaminated front over time, with more deviation between mean air age profiles and contaminant distribution seen early on due to the rapid, kinetic governed period of adsorption.

Another assessment of the relationship between mean air age and adsorption performance was made by observing the time at which each location within the bed was first seen to be contaminated above a threshold value. This was then correlated with the residence time distribution throughout the bed. It was generally seen that increasing mean air age increased with the time of first contamination, although a single mean air age can correlate to a wide range of first contamination times. The average breakthrough time showed a more linear relationship with mean air age, and across all cases a similar linear regression coefficient was seen between the two values.

Although the number of cases investigated here was very limited, there is some evidence that there is justification for using mean air age as an indicator of adsorption performance, with potential for more qualitative relationships to be developed in future.

Chapter 10

Conclusions and Future Work

In this thesis, an investigation has been conducted into the ways that PAPRs may be improved by a better understanding of the flow within. From a review of the literature and analysis of a system level it was identified that the flow through the filter was the area with the greatest potential for improvement. A number of CFD studies were conducted to investigate key parameters affecting flow through the carbon bed. These consisted of:

- An initial study conducting a large number of axisymmetric simulations, in which the geometry of the filter canister was varied in small ways. The impact of these variations and the interactions between them were then assessed using Analysis of Variance (ANOVA).
- A study of an existing filter canister geometry to assess the relationship between flow behaviour under continuous and transient flow conditions.
- A study of how the performance of the adsorbent bed would be impacted by the flow profile and adsorption kinetics of the inlet contaminant.
- Development of a more accurate model to describe the distribution of porosity throughout the carbon bed, and a study of the impact this would have on canister performance.
- An investigation of the relationship between residence time distribution and adsorption performance within a carbon bed.

Key findings of each of these are given in the following sections.

10.1 Impact of Canister Geometry on Filter Performance

Simulations were conducted on a large number of simple variations of a standard filter canister geometry. It was demonstrated that the non-uniform porosity profile of the carbon bed resulted in alternating regions of high and low velocity close to the canister wall, providing a possible route

for breakthrough. Designs which included a bracket at the rear of the carbon bed, blocked this route and consequently had a longer minimum mean residence time than those, which did not. Altering the shape of the outer wall of the carbon bed could also influence this by guiding air through a longer route out of the highly porous region to maximise residence time.

It was also shown that the spacing between the carbon bed and the canister rear wall had a large impact on both residence time and pressure drop. In cases where the carbon backed directly onto the canister rear wall flow in the axial direction from the outside wall toward the canister axis resulted in far greater pressure drop and a reduction in minimum mean residence time within the carbon bed.

The flow distribution throughout the bed was shown to be highly dependent on inlet flowrate; when exposed to transient inlet conditions there is some scope to manipulate flow over the course of a breathing cycle to optimise filter usage by altering the shape and position of the inlet.

10.2 The Relationship between Steady-State and Transient Canister Performance

Canister performance under steady-state conditions was compared to performance under three different flow conditions which simulated real breathing profiles. It was seen that the pressure drop under steady state conditions was identical to that under the transient conditions at the same instantaneous inlet flow rate. This was not true for mean air age, which varied substantially in its distribution for the same instantaneous inlet flow rates. In general the transient cases showed a similar distribution of mean air age with respect to radial coordinate at the same stage in each breathing cycle, with similarly located dead zones. For each of the breathing rates a large region of higher mean air age was seen early on in the inhalation, with a more even distribution seen later on.

If a threshold mean air age is chosen to represent breakthrough then the same over all distribution of that threshold value will be seen at the moment of breakthrough, regardless of breathing rate or the choice of threshold value. In the geometry seen here, the shortest route seen through the filter always occurred in line with the central inlet holes.

10.3 Adsorption Kinetics within an Activated Carbon Bed

Throughout a breathing cycle, the minimum residence time seen at the outlet of a filter was consistently lower for transient breathing profiles than for the equivalent steady state flow rate. Significantly, the minimum residence time seen at any point in a breathing cycle maintained a constant ratio to the minimum residence time seen under the equivalent steady state flow rate.

10.3 Adsorption Kinetics within an Activated Carbon Bed

The adsorption process within an activated carbon bed was investigated to see how the performance of a respirator filter could be compared to existing models of adsorbent bed breakthrough. Over a wide range of flow rates it was seen that the adsorption process can be separated into two components; a rapid kinetically governed process which defines the shape of the contaminant front, and a slow kinetic-independent stage which governs the rate at which the contaminated front advances through the adsorbent bed. This is consistent with the behaviour seen in much larger beds, indicating that the larger influence of the walls in a small bed is not greatly significant to adsorption performance.

While the rate at which the contaminated front advanced through the bed was expected to be independent of adsorption kinetics, it was in fact found that slower kinetics resulted in slightly slower front speeds this was attributed to two factors. Firstly, when adsorption was fast there was a greater fluid acceleration due to the faster reduction in volume; this resulted in a greater generation of turbulence and a flatter profile, better approximating plug-flow conditions. Secondly, there was also a substantial entry-effect as in the inlet stream the contaminant entering was not mixed uniformly and the area first contaminated did not fall on the centre-line of the carbon bed, altering the shape of the initially contaminated region. This was shown to have a greater effect when the adsorption kinetics were fast. The extent to which effect occurs is likely to vary greatly in other applications depending on the geometry and conditions of the inlet.

10.4 Developing a Stochastic Model of Porosity within the Carbon Bed

Describing porosity using only the Mueller equation was found to be somewhat limited for some applications, showing a greater degree of flow channelling the near wall region than is seen in real

porous beds. A model was developed to incorporate the random variations around the longitudinally averaged porosity profile that are seen in real packed beds, by subdividing the bed into discrete sections and assigning each section a local porosity based on its radial position and a probability distribution function. For the generic CBRN canister investigated, it was shown that 2 mm was the largest possible section size that would give repeatable results when new random parameters were generated. However, simulations with 2 mm sections showed an unrealistic level of flow channelling through interconnected regions of similar porosity.

For smaller sections, it was generally seen that an increase in random porosity variations resulted in an increased pressure drop across the canister, as well as a decrease in average mean air age and an increase in minimum mean air age seen at the outlet of the canister. These could all be attributed to the large velocity gradients caused by adjacent areas of high and low porosity. This in turn resulted in increased turbulence and a flatter flow profile.

It was seen that for section sizes close to the particle size, the two-parameter porosity model could be reduced to a single parameter, the section size to standard deviation ratio. This significantly reduces the amount of experimental data needed for designing and validating a section-based model. These trends were all seen to persist over a range of flow rates.

10.5 Relating Mean Air Age to Adsorption Performance

The relationship between mean air age and adsorption performance was investigated by comparing the distribution of mean air age to the distribution of contaminant in an adsorbent bed over time, and it was generally seen that the shape of the contaminated front showed a good qualitative match to the mean air age profile, especially after the initial fast kinetically-governed penetration into the bed.

The time at which each location within the bed was contaminated was correlated against the mean air age across the whole volume of the bed and it was found that, while increasing mean air age on average corresponded to increasing time until contamination, a single mean air age could correspond to a wide range of first contamination times. The average first contamination time

showed a roughly linear increase with mean air age, however, and the linear relationship between the two was shown to be consistent over the small number of cases seen, suggesting potential for a quantitative relationship between mean air age and first contamination time.

10.6 Future Work

The findings of this work raise a number of additional issues which should be the subject for further investigation as follows:

- The relationship between steady state and transient performance of a CBRN canister should be investigated for a wider range of geometries, to see if the trends identified here are applicable to all cases.
- Further adsorption modelling under human breathing profiles should be carried out to investigate the effect this has on the contaminant distribution.
- The section-based porosity model developed here should be the subject of further investigation in order to better understand the range of its applicability. In particular the limits at which such a model may be reduced to a single parameter should be better quantified.
- Investigation into the correlation between mean air age and adsorption performance should be carried out over a wide range of scenarios to identify if there is greater potential to quantify this relationship.
- The use of mean air age as a proxy for adsorption performance should be confirmed against further experimental studies.

Many of the methods developed within this thesis provide possible routes by which greater insight into filter canister performance may be assessed with fewer experiments and simulations. Ultimately the goal of further work should be to use these tools and others to develop improved PAPRs and provide a higher degree of protection to the wearer than is currently seen.

References

- [1] Myers, W.R., *Respiratory Protective Equipment*, in *Patty's Industrial Hygiene*. 2001.
- [2] Stratling, W.M., et al., *Comparison of powered and conventional air-purifying respirators during simulated resuscitation of casualties contaminated with hazardous substances*.
Emergency Medicine Journal, 2008. **26**: p. 501-505.
- [3] *Approval of Respiratory Protective Devices: Non-Powered Air-Purifying Particulate Respirators*, in *Electronic Code of Federal Regulations Title 42*. 2019.
- [4] Schumacher, J., et al., *Comparison of Powered and Conventional Air-Purifying Respirators during Simulated Resuscitation of Casualties Contaminated with Hazardous Substances*.
Emergency Medicine Journal, 2009. **26**(7): p. 501-505.
- [5] Scott Safety, *C420 Plus CBRN Powered Air Purifying Respirator*, 2014
- [6] STS Shigematsu., *Sync01VP3 Full Face Respirator – Powered*. 2014:
<https://www.arenz.co.nz/wp-content/uploads/2014/12/STS40401.jpg>.
- [7] Janssen, L., et al., *CBRN Respirator Protection Handbook*. 2018, Department of Health and Human Services, Centers for Disease Control and Prevention: National Institute for Occupational Safety and Health, DHHS (NIOSH).
- [8] NIOSH, *Statement of Standard for Chemical, Biological, Radiological and Nuclear (CBRN) Full Facepiece Air Purifying Respirator*. 2003, NIOSH: Washington, DC.
- [9] Henning, K.D. and S. Schäfer, *Impregnated activated carbon for environmental protection*.
Gas Separation & Purification, 1993. **7**(4): p. 235-240.
- [10] Mueller, G.E., *Radial porosity in packed beds of spheres*. *Powder Technology*, 2010. **203**(3):
p. 626-633.

- [11] Sandberg, M. and M. Sjöberg, *The use of moments for assessing air quality in ventilated rooms*. Building and Environment, 1983. **18**(4): p. 181-197.
- [12] Hu, Q. and Z. Zhang, *Application of Dubinin–Radushkevich isotherm model at the solid/solution interface: A theoretical analysis*. Journal of Molecular Liquids, 2019. **277**: p. 646-648.
- [13] Sircar, S. and J.R. Hufton, *Why Does the Linear Driving Force Model for Adsorption Kinetics Work?* Adsorption, 2000. **6**(2): p. 137-147.
- [14] White, F.M., *Fluid mechanics*. McGraw Hill, 2015.
- [15] Versteeg, H.K. and W. Malalasekera, *An introduction to computational fluid dynamics: the finite volume method*. 2007: Pearson education.
- [16] Kalitzin, G., et al., *Near-wall behavior of RANS turbulence models and implications for wall functions*. Journal of Computational Physics, 2005. **204**(1): p. 265-291.
- [17] Mansour, N.N., J. Kim, and P. Moin, *Near-wall k-epsilon turbulence modeling*. AIAA Journal, 1989. **27**(8): p. 1068-1073.
- [18] Kader, B.A., *Temperature and concentration profiles in fully turbulent boundary layers*. International Journal of Heat and Mass Transfer, 1981. **24**(9): p. 1541-1544.
- [19] ANSYS, *Academic Research, Release 16.2*. 2016: Ansys.
- [20] Patankar, S., *Numerical Heat Transfer and Fluid Flow*. 1980: Hemisphere Publishing Corporation.
- [21] Martyny, J., C.S. Glazer, and L.S. Newman, *Respiratory protection*. New England Journal of Medicine, 2002. **347**(11): p. 824-830.

-
- [22] Koenig, K.L., et al., *Health care facilities' "war on terrorism": a deliberate process for recommending personal protective equipment*. The American journal of emergency medicine, 2007. **25**(2): p. 185-195.
- [23] Bollinger, N.J. and R.H. Schutz, *NIOSH guide to industrial respiratory protection*. 1987.
- [24] Garner, A., H. Laurence, and A. Lee, *Practicality of performing medical procedures in chemical protective ensembles*. Emergency Medicine, 2004. **16**(2): p. 108-113.
- [25] United States General Accounting Office, *Chemical Warfare: Soldiers Inadequately Equipped and Trained to Conduct Chemical Operations : Report to Congressional Requesters*. 1991: The Office.
- [26] Al-Damouk, M. and A. Bleetman, *Impact of the Department of Health initiative to equip and train acute trusts to manage chemically contaminated casualties*. Emergency medicine journal, 2005. **22**(5): p. 347-350.
- [27] Viscusi, D.J., et al., *Evaluation of the benefit of the user seal check on N95 filtering facepiece respirator fit*. Journal of occupational and environmental hygiene, 2012. **9**(6): p. 408-416.
- [28] Gross, S.F. and S.W. Horstman, *Half-mask respirator selection for a mixed worker group*. Applied Occupational and Environmental Hygiene, 1990. **5**(4): p. 229-235.
- [29] Skaggs, B.J., et al., *Effects of temperature and humidity on respirator fit under simulated work conditions*. 1988, Nuclear Regulatory Commission, Washington, DC (USA). Div. of Regulatory Applications
- [30] Khoo, K.L., et al., *The changing face of healthcare worker perceptions on powered air-purifying respirators during the SARS outbreak*. Respiriology, 2005. **10**(1): p. 107-110.

- [31] Arad, M., et al., *The effects of continuous operation in a chemical protective ensemble on the performance of medical tasks in trauma management*. The Journal of Trauma, 1993. **35**(5): p. 800-804.
- [32] Johnson, A.T., et al., *Exercise performance while wearing a tight-fitting powered air purifying respirator with limited flow*. Journal of Occupational and Environmental Hygiene, 2005. **2**(7): p. 368-373.
- [33] Currie, J., D. Caseman, and T.R. Anthony, *The Evaluation of CBRN canisters for use by Firefighters during Overhaul*. The Annals of Occupational Hygiene, 2009. **53**(5): p. 523-538.
- [34] United States. Occupational, S., S. Health Administration. Office of, and A. Technology, *OSHA Technical Manual*. Vol. 1. 1995: US Department of Labor, Occupational Safety and Health Administration
- [35] NIOSH, *Standard Respirator Testing Procedures: Air-Purifying Respirators with Chemical, Biological, Radiological, and Nuclear Protection*. 2016.
- [36] Tanaka, S., et al., *Breakthrough time of a respirator cartridge for carbon tetrachloride vapor flow of workers' respiratory patterns*. Industrial health, 1996. **34**(3): p. 227-236.
- [37] Anderson, N.J., et al., *Peak inspiratory flows of adults exercising at light, moderate and heavy work loads*. Journal of the International Society for Respiratory Protection, 2006. **23**(1/2): p. 53.
- [38] Subrenat, A., J.-N. Baléo, and P.L. Cloirec, *Analysis of pressure drops in pleated activated carbon cloth filters*. Journal of Environmental Engineering, 2000. **126**(6): p. 562-568.

-
- [39] Virr, A., Kao, D., Fu, X., Snow, J.M. and Chen, J., PAFTEC TECHNOLOGIES Pty Ltd, 2016. *Respirator*. U.S. Patent 9,248,248.
- [40] Kao, D., Fu, X.E., Virr, A., Snow, J.M. and Johnson, D.C., PAFTEC TECHNOLOGIES Pty Ltd, 2014. *Breathing Apparatus*. U.S. Patent Application 14/363,100.
- [41] Liu, Z.G. and P.K. Wang, *Numerical investigation of viscous flow fields around multifiber filters*. *Aerosol science and technology*, 1996. **25**(4): p. 375-391.
- [42] Chen, D.-R., D.Y.H. Pui, and B.Y.H. Liu, *Optimization of pleated filter designs using a finite-element numerical model*. *Aerosol Science and Technology*, 1995. **23**(4): p. 579-590.
- [43] Haghghat, F., et al., *Evaluation of various activated carbons for air cleaning – Towards design of immune and sustainable buildings*. *Atmospheric Environment*, 2008. **42**(35): p. 8176-8184.
- [44] Baléo, J.-N. and P.L. Cloirec, *Numerical simulation of the spatial distribution of mean residence time in complex flows through porous media*. *Progress of Theoretical Physics Supplement*, 2000. **138**: p. 690-695.
- [45] Li, C.-C., *Aerodynamic Behavior of a Gas Mask Canister Containing Two Porous Media*. *Chemical Engineering Science*, 2009. **64**(8): p. 1832-1843.
- [46] Su, Y.-C. and C.-C. Li, *Computational fluid dynamics simulations and tests for improving industrial-grade gas mask canisters*. *Advances in Mechanical Engineering*, 2015. **7**(8): p. 1687814015596297.
- [47] Su, Y., C. Li, and Y. Chang, *Dual Inlets Design of an Air Purifying Respirator to Study Inhalation Pressure Drop Reduction and Heart Rate Prediction*. *International Conference on Mechanical And Industrial Engineering*, 2015.

-
- [48] Si, F., *3D Numerical Simulation of Aerodynamic Characteristics of a Gas Filter*. Journal of Applied Mathematics and Physics, 2019. **7**(08): p. 1920.
- [49] Bansal, R.C. and M. Goyal, *Activated carbon adsorption*. 2005: CRC press.
- [50] Lagorsse, S., et al., *Water adsorption on carbon molecular sieve membranes: experimental data and isotherm model*. Carbon, 2005. **43**(13): p. 2769-2779.
- [51] Zhu, W., et al., *Adsorption of butane isomers and SF₆ on Kureha activated carbon: 1. Equilibrium*. Langmuir, 2004. **20**(13): p. 5277-5284.
- [52] Kinniburgh, D.G., *General purpose adsorption isotherms*. Environmental science & technology, 1986. **20**(9): p. 895-904.
- [53] Sheindorf, C., M. Rebhun, and M. Sheintuch, *A Freundlich-type multicomponent isotherm*. Journal of Colloid and Interface Science, 1981. **79**(1): p. 136-142.
- [54] Liu, Y., *Some consideration on the Langmuir isotherm equation*. Colloids and Surfaces A: Physicochemical and Engineering Aspects, 2006. **274**(1-3): p. 34-36.
- [55] Masel, R.I., *Principles of adsorption and reaction on solid surfaces*. Vol. 3. 1996: John Wiley & Sons.
- [56] Dada, A.O., et al., *Langmuir, Freundlich, Temkin and Dubinin–Radushkevich isotherms studies of equilibrium sorption of Zn²⁺ unto phosphoric acid modified rice husk*. IOSR Journal of Applied Chemistry, 2012. **3**(1): p. 38-45.
- [57] Bawn, C.E.H., *THE ADSORPTION OF GASES AND VAPORS ON PLANE SURFACES*. Journal of the American Chemical Society, 1932. **54**(1): p. 72-86.

-
- [58] Choy, K.K.H., J.F. Porter, and G. McKay, *Langmuir isotherm models applied to the multicomponent sorption of acid dyes from effluent onto activated carbon*. Journal of Chemical & Engineering Data, 2000. **45**(4): p. 575-584.
- [59] Mazzotti, M., *Equilibrium theory based design of simulated moving bed processes for a generalized Langmuir isotherm*. Journal of Chromatography A, 2006. **1126**(1): p. 311-322.
- [60] Sohn, S. and D. Kim, *Modification of Langmuir isotherm in solution systems—definition and utilization of concentration dependent factor*. Chemosphere, 2005. **58**(1): p. 115-123.
- [61] Yang, C.-h., *Statistical mechanical study on the Freundlich isotherm equation*. Journal of colloid and interface science, 1998. **208**(2): p. 379-387.
- [62] Skopp, J., *Derivation of the Freundlich adsorption isotherm from kinetics*. Journal of chemical education, 2009. **86**(11): p. 1341.
- [63] Fitter, A.H. and C.D. Sutton, *The use of the Freundlich isotherm for soil phosphate sorption data*. Journal of Soil Science, 1975. **26**(3): p. 241-246.
- [64] Jeppu, G.P. and T.P. Clement, *A modified Langmuir-Freundlich isotherm model for simulating pH-dependent adsorption effects*. Journal of contaminant hydrology, 2012. **129**: p. 46-53.
- [65] Nguyen, C. and D.D. Do, *The Dubinin–Radushkevich equation and the underlying microscopic adsorption description*. Carbon, 2001. **39**(9): p. 1327-1336.
- [66] Dubinin, M., *The potential theory of adsorption of gases and vapors for adsorbents with energetically nonuniform surfaces*. Chemical Reviews, 1960. **60**(2): p. 235-241.

- [67] Chen, S.G. and R.T. Yang, *Theoretical basis for the potential theory adsorption isotherms. The Dubinin-Radushkevich and Dubinin-Astakhov equations*. Langmuir, 1994. **10**(11): p. 4244-4249.
- [68] Ozawa, S., S. Kusumi, and Y. Ogino, *Physical adsorption of gases at high pressure. IV. An improvement of the Dubinin—Astakhov adsorption equation*. Journal of Colloid and Interface Science, 1976. **56**(1): p. 83-91.
- [69] Linders, M.J.G., et al., *Breakthrough of shallow activated carbon beds under constant and pulsating flow*. AIHA Journal, 2003. **64**(2): p. 173-180.
- [70] Ambesi, D., et al., *Predicting the chemical protection factor of CBRN protective garments*. Journal of Occupational and Environmental Hygiene, 2013. **10**(5): p. 270-276.
- [71] Reid, C.R. and K.M. Thomas, *Adsorption Kinetics and Size Exclusion Properties of Probe Molecules for the Selective Porosity in a Carbon Molecular Sieve Used for Air Separation*. The Journal of Physical Chemistry B, 2001. **105**(43): p. 10619-10629.
- [72] Fletcher, A.J., Y. Yuzak, and M. Thomas, *Adsorption and desorption kinetics for hydrophilic and hydrophobic vapors on activated carbon*. Carbon, 2006. **44**(5): p. 989-1004.
- [73] Linders, M.J.G., et al., *Design of an industrial adsorption process with activated carbon for the removal of hexafluoropropylene from wet air*. Industrial & engineering chemistry research, 2001. **40**(14): p. 3171-3180.
- [74] Alhamed, Y.A., *Adsorption kinetics and performance of packed bed adsorber for phenol removal using activated carbon from dates' stones*. Journal of hazardous materials, 2009. **170**(2-3): p. 763-770.

- [75] Cooney, D.O., *The importance of axial dispersion in liquid-phase fixed-bed adsorption operations*. Chemical Engineering Communications, 1991. **110**(1): p. 217-231.
- [76] Rosene, M.R., *Treatment of water by granular activated carbon*, in *Advances in Chemistry Series 202*. 1983, American Chemical Society Washington, DC. p. 201.
- [77] Chandrasekhara, B.C. and D. Vortmeyer, *Flow model for velocity distribution in fixed porous beds under isothermal conditions* *Modell der Geschwindigkeitsverteilung in einem isotherm durchströmten Festbett*. Wärme-und Stoffübertragung, 1979. **12**(2): p. 105-111.
- [78] Wood, G.O., *A review of the effects of vapors on adsorption rate coefficients of organic vapors adsorbed onto activated carbon from flowing gases*. Carbon, 2002. **40**(5): p. 685-694.
- [79] Coppola, A.P. and M.D. Levan, *Adsorption with axial diffusion in deep beds*. Chemical Engineering Science, 1981. **36**(6): p. 967-971.
- [80] Coppola, A.P. and M.D. Levan, *Adsorption with axial diffusion in shallow beds*. Chemical Engineering Science, 1983. **38**(7): p. 991-997.
- [81] Yoon, Y.H. and J.H. Nelson, *A theoretical model for respirator cartridge service Life*. Am Ind Hyg As-soc J, 1984. **45**(8): p. 509-516.
- [82] Yoon, Y.H., et al., *A theoretical model for respirator cartridge service life for binary systems: Application to acetone/styrene mixtures*. American Industrial Hygiene Association Journal, 1992. **53**(8): p. 493-502.
- [83] Croll, L., et al. *Design and Evaluation of Escape and CBRN Respirator Cartridges Using Nano Gold Carbon Monoxide Oxidation Catalysts*. in *10th International Symposium on Protection against Chemical and Biological Warfare Agents, Stockholm*. 2010.

- [84] Guidotti, M., et al., *Structured inorganic oxide-based materials for the absorption and destruction of CBRN agents*, in *Advanced Sensors for Safety and Security*. 2013, Springer. p. 43-53.
- [85] Gunjal, P.R. and V.V. Ranade, *Modeling of laboratory and commercial scale hydro-processing reactors using CFD*. *Chemical Engineering Science*, 2007. **62**(18): p. 5512-5526.
- [86] Roblee, L.H.S., R.M. Baird, and J.W. Tierney, *Radial porosity variations in packed beds*. *AIChE Journal*, 1958. **4**(4): p. 460-464.
- [87] Benenati, R.F. and C.B. Brosilow, *Void fraction distribution in beds of spheres*. *AIChE Journal*, 1962. **8**(3): p. 359-361.
- [88] Thadani, M.C. and F.N. Peebles, *Variation of local void fraction in randomly packed beds of equal spheres*. *Industrial & Engineering Chemistry Process Design and Development*, 1966. **5**(3): p. 265-268.
- [89] Vortmeyer, D. and J. Schuster, *Evaluation of steady flow profiles in rectangular and circular packed beds by a variational method*. *Chemical Engineering Science*, 1983. **38**(10): p. 1691-1699.
- [90] Bey, O. and G. Eigenberger, *Fluid flow through catalyst filled tubes*. *Chemical Engineering Science*, 1997. **52**(8): p. 1365-1376.
- [91] Kűfner, R. and H. Hofmann, *Implementation of radial porosity and velocity distribution in a reactor model for heterogeneous catalytic gasphase reactions (TORUS-Model)*. *Chemical Engineering Science*, 1990. **45**(8): p. 2141-2146.

-
- [92] Dixon, A.G., et al., *Experimental validation of high Reynolds number CFD simulations of heat transfer in a pilot-scale fixed bed tube*. Chemical Engineering Journal, 2012. **200**: p. 344-356.
- [93] Behnam, M., et al., *A new approach to fixed bed radial heat transfer modeling using velocity fields from computational fluid dynamics simulations*. Industrial & Engineering Chemistry Research, 2013. **52**(44): p. 15244-15261.
- [94] Torquato, S. and H.W. Haslach Jr, *Random heterogeneous materials: microstructure and macroscopic properties*. Appl. Mech. Rev., 2002. **55**(4): p. B62-B63.
- [95] Suikkanen, H., et al., *Discrete element modelling of pebble packing in pebble bed reactors*. Nuclear Engineering and Design, 2014. **273**: p. 24-32.
- [96] Jiang, Y., et al., *CFD of multiphase flow in packed-bed reactors: I. k-Fluid modeling issues*. AIChE Journal, 2002. **48**(4): p. 701-715.
- [97] Lappalainen, K., M. Manninen, and V. Alopaeus, *CFD modeling of radial spreading of flow in trickle-bed reactors due to mechanical and capillary dispersion*. Chemical Engineering Science, 2009. **64**(2): p. 207-218.
- [98] Gunjal, P.R., V.V. Ranade, and R.V. Chaudhari, *Liquid distribution and RTD in trickle bed reactors: experiments and CFD simulations*. Canadian Journal of Chemical Engineering, 2003. **81**(3-4): p. 821-830.
- [99] *MATLAB*. 2016, The MathWorks Inc: Natick, Massachusetts.
- [100] Ergun, S., *Flow through packed columns*. Chemical Engineering Progress, 1952. **48**: p. 89-94.

- [101] Dixon, S.L. and C.A. Hall, *Chapter 1 - Introduction: Basic Principles*, in *Fluid Mechanics and Thermodynamics of Turbomachinery (Seventh Edition)*, S.L. Dixon and C.A. Hall, Editors. 2014, Butterworth-Heinemann: Boston. p. 1-37.
- [102] Narabayashi, T., et al., *Centrifugal pump behavior in steady and transient two-phase flow*. Journal of Nuclear Science and Technology, 1986. **23**(2): p. 136-150.
- [103] Brown, G.O., *The history of the Darcy-Weisbach equation for pipe flow resistance*, in *Environmental and Water Resources History*. 2003. p. 34-43.
- [104] Lücke, T. and H. Fissan, *The prediction of filtration performance of high efficiency gas filter elements*. Chemical Engineering Science, 1996. **51**(8): p. 1199-1208.
- [105] Li, C., *Aerodynamic behaviour of a gas mask canister containing two porous media*. Chemical Engineering Science, 2008(64): p. 1832-1843.
- [106] Smith, A.G., S. MW, and K. Taylor, *Prediction of heat and Mass Transfer in Canister Filters*. PHOENICS User Conference, 2004.
- [107] Suzin, Y., I. Nir, and D. Kaplan, *The effect of flow pattern on adsorption of dimethyl methyl phosphonate in activated carbon beds and canisters*. Carbon, 2000. **38**(8): p. 1129-1133.
- [108] Wilcox, D.C., *Turbulence Modeling for CFD*, in *Turbulence Modeling for CFD*. 1994, DCW Industries, Inc.: California.
- [109] Harris, E., *Improvements in or relating to the filling of granular materials into containers*. 1946, GB Patent 606867: United Kingdom.
- [110] Mueller, G.E., *Radial void fraction distributions in randomly packed fixed beds of uniformly sized spheres in cylindrical containers*. Powder Technology, 1992. **72**(3): p. 269-275.
- [111] Mann, P.S. and C.J. Lacke, *Introductory Statistics*. 2001, Hoboken: Wiley.

- [112] Galván, S., M. Reggio, and F. Guibault, *Assessment study of K - ε turbulence models and near-wall modeling for steady state swirling flow analysis in draft tube using fluent*. Engineering Applications of Computational Fluid Mechanics, 2011. **5**(4): p. 459-478.
- [113] Yuasa, H., et al., *Breathing simulator of workers for respirator performance test*. Industrial health, 2015. **53**(2): p. 124-131.
- [114] Wheeler, A. and A.J. Robell, *Performance of fixed-bed catalytic reactors with poison in the feed*. Journal of Catalysis, 1969. **13**(3): p. 299-305.
- [115] Wang, G., et al., *Adsorption of benzene, cyclohexane and hexane on ordered mesoporous carbon*. Journal of Environmental Sciences, 2015. **30**: p. 65-73.
- [116] Heeb, T.G. and R.S. Brodkey, *Turbulent mixing with multiple second-order chemical reactions*. AIChE Journal, 1990. **36**(10): p. 1457-1470.
- [117] Das, A.K., et al., *CFD simulation of dilute phase gas–solid riser reactors: part II—simultaneous adsorption of SO_2 – NO_x from flue gases*. Chemical Engineering Science, 2004. **59**(1): p. 187-200.
- [118] Wood, S.G.A., et al., *The impact of canister geometry on chemical biological radiological and nuclear filter performance: A computational fluid dynamics analysis*. Journal of Occupational and Environmental Hygiene, 2018: p. 1-35.
- [119] Berezhnoi, A.N. and A.V. Semenov, *Binary diffusion coefficients of liquid vapors in gases*. 1997: Begell House New York.
- [120] Lodewyckx, P., G.O. Wood, and S.K. Ryu, *The Wheeler–Jonas equation: a versatile tool for the prediction of carbon bed breakthrough times*. Carbon, 2004. **42**(7): p. 1351-1355.

- [121] Wood, G.O. and P. Lodewyckx, *An Extended Equation for Rate Coefficients for Adsorption of Organic Vapors and Gases on Activated Carbons in Air-Purifying Respirator Cartridges*. AIHA Journal, 2003. **64**(5): p. 646-650.
- [122] NIOSH, *Determination of CBRN Organic Vapor (Cyclohexane) Service Life Test, Air Purifying Respirators Standard Test Procedure (STP) CET-APRS-STP-CBRN-0301*. 2005, Centers for Disease Control and Prevention: <https://www.cdc.gov/niosh/npptl/stps/aprespnbrn.html>.
- [123] Grévillet, G., S. Marsteau, and C. Vallières, *A Comparison of the Wheeler-Jonas Model and the Linear Driving Force at Constant-Pattern Model for the Prediction of the Service Time of Activated Carbon Cartridges*. Journal of Occupational and Environmental Hygiene, 2011. **8**(5): p. 279-288.
- [124] Wang, Y., J. Chen, and F. Larachi, *Modelling and simulation of trickle-bed reactors using computational fluid dynamics: A state-of-the-art review*. Canadian Journal of Chemical Engineering, 2013. **91**(1): p. 136-180.
- [125] Sederman, A.J., et al., *Structure-flow correlations in packed beds*. Chemical Engineering Science, 1998. **53**(12): p. 2117-2128.
- [126] Harter, I., et al., *Flow distribution studies applied to deep hydro-desulfurization*. Industrial and Engineering Chemistry Research, 2001. **40**(23): p. 5262-5267.
- [127] Gunjal, P.R., et al., *Hydrodynamics of trickle-bed reactors: experiments and CFD modeling*. Industrial and Engineering Chemistry Research, 2005. **44**(16): p. 6278-6294.
- [128] Chen, J., et al., *Particle motion in packed/ebullated beds by CT and CARPT*. AIChE journal, 2001. **47**(5): p. 994-1004.

-
- [129] Wood, S.G.A., et al., *A computational fluid dynamics analysis of transient flow through a generic Chemical Biological Radiological and Nuclear respirator canister*. Chemical Engineering Research and Design, 2019. **142**: p. 13-24.
- [130] Taylor, K., et al., *CFD modelling of pressure drop and flow distribution in packed bed filters*. PHOENICS Journal of Computational Fluid Dynamics and its applications, 2000. **13**(4): p. 399-413.
- [131] Jonas, L.A. and J.A. Rehrmann, *Predictive equations in gas adsorption kinetics*. Carbon, 1973. **11**(1): p. 59-64.
- [132] Wood, S.G.A. and N. Chakraborty. *Transient Performance of Chemical, Biological, Radiological and Nuclear Filter Canisters*. in *ASTFE Digital Library*. 2018. Begel House Inc.